

Computational investigation of the response of osteoblasts in interaction with substrate under effects of electric field exposure



Dissertation
zur
Erlangung des akademischen Grades
Doktor-Ingenieur (Dr.-Ing.)
der Fakultät für Informatik und Elektrotechnik
der Universität Rostock

vorgelegt von

Thanh Duy Truong, geboren am 27.08.1987 in Ca Mau, Vietnam

Rostock, 2018

Datum der Einreichung: 05.02.2018

Datum der Verteidigung: 08.05.2018

Gutachter

Prof. Dr. Ursula van Rienen, Universität Rostock

Prof. Dr. Barbara Nebe, Universitätsmedizin Rostock

Prof. Dr. José Manuel García Aznar, Universidad Zaragoza

Abstract

Further improvement of implants for the human skeleton involves understanding interactions between bone cells and surrounding bio-materials under different stimuli (bio-chemical, biophysical, mechanical, electrical). In addition to experimental methods, the computational approach has been a useful tool to investigate the mechanisms of these interactions. In this thesis, we attempt to build a numerical model that predicts the traction forces and the actin distribution in osteoblasts when they interact with substrates of different characteristics, where the effects of external electric field are addressed. Our model is based on the bio-chemo-mechanical model proposed by Deshpande *et al.* [15], which possesses many advantages and has been widely applied to simulate two and three dimensional cells in interaction with various substrates.

The results we obtain in this thesis can be summarised in three main achievements. First, we successfully reduced the complexity of the bio-chemo-mechanical model using a semi-analytical approach. Our formulation delivered similar results compared to the classical approach, while the computation time was significantly improved. Second, we proposed an inhomogeneous adhesion and constructed smooth scaling functions representing the differences in strength of adhesion at different locations in the contact parts between cells and micro-pillar structures. With our description for the adhesion, the bio-chemo-mechanical model was able to predict the actin distribution in the experiments of osteoblasts on titanium micro-pillar arrays. Finally, we enhanced the bio-chemo-mechanical model with our description for the effects of the direct-current (DC) electric field by letting the tension in stress fibres depend on their orientation and introducing a scaling function representing the weakening of adhesion at some parts of the cell. Our enrichment of the model helped predict several existing experimental outcomes on fibroblasts and osteoblasts when they are exposed to DC electric field.

Zusammenfassung

Eine weitere Verbesserung von Implantaten für das menschliche Knochengerüst erfordert ein besseres Verständnis der Wechselwirkung zwischen Knochenzellen und benachbarten Biomaterialien im Hinblick auf verschiedene Stimuli (biochemische, biophysikalische, mechanische, elektrische). Neben experimentellen Methoden erwiesen sich computergestützte Ansätze als ein nützliches Werkzeug zur Untersuchung der Mechanismen dieser Wechselwirkungen. In dieser Arbeit wird versucht, ein numerisches Modell aufzustellen, das die Traktionskräfte und die Aktinverteilung in Osteoblasten vorhersagt, wenn diese mit Substraten unterschiedlicher Eigenschaften interagieren und dabei den Wirkungen eines externen elektrischen Feldes unterliegen. Das vorgestellte Modell basiert auf dem von Deshpande *et al.* [15] vorgeschlagenen bio-chemo-mechanischen Modell, welches viele Vorteile aufweist und breit angewendet wurde, um zwei- und dreidimensionale Zellen in Wechselwirkung mit verschiedenen Substraten zu simulieren. Die in dieser Arbeit erhaltenen Ergebnisse können in drei wesentlichen Erfolgen zusammengefasst werden. Erstens konnte die Komplexität des bio-chemo-mechanischen Modells unter Verwendung eines semi-analytischen Ansatzes erfolgreich reduziert werden. Im Vergleich zum klassischen Ansatz lieferte die neue Formulierung ähnliche Ergebnisse, während die Rechenzeit deutlich verbessert wurde. Zweitens wurde eine inhomogene Adhäsion vorgeschlagen und glatte Skalierungsfunktionen konstruiert, die die Unterschiede in der Haftfestigkeit an verschiedenen Stellen in den Kontaktteilen zwischen Zellen und Mikrosäulenstrukturen darstellen. Mit der hier eingeführten Beschreibung für die Adhäsion konnte das bio-chemo-mechanische Modell die in den Experimenten mit Osteoblasten auf Titan-Mikrosäulen-Arrays beobachtete Aktinverteilung vorhersagen. Schließlich wurde das bio-chemo-mechanische Modell um eine Beschreibung der Wirkung eines Gleichstromfeldes verbessert, indem die Zugspannung in den Stressfasern in Abhängigkeit von ihrer Orientierung modelliert wurde und eine Skalierungsfunktion einführt wurde, welche die Abschwächung der Adhäsion in einigen Teilen der Zelle wiedergibt. Unsere Verbesserung des Modells trug dazu bei, mehrere experimentelle Ergebnisse zu Fibroblasten und Osteoblasten unter der Wirkung eines Gleichstromfeldes zuverlässig vorhersagen zu können.

Acknowledgements

First of all, I would like to thank Prof. Dr. Ursula van Rienen for offering me a chance to work in her group and for her great supervision of my work. She has given me kind support, good advices and more than sufficient encouragement to overcome the obstacles I met.

Secondly, I would like to thank Prof. Dr. Barbara Nebe for her valuable advice and her kind collaboration during my research. Together with Prof. van Rienen, she brought me an interesting research topic and provided me with ideas and discussions that helped the development of my research.

I would also like to express my appreciation to my colleagues for building a friendly environment in the working group and offering help every time I needed it. Particularly, I would like to thank my officemate Andrea Böhme and Dr. Christian Bahls for their strong support and encouragement.

My research would not have been possible without the financial support from the German Science Foundation (DFG) through the research training group 1505/2 *welisa*. I would like to gratefully acknowledge the support.

Finally, I would like to express my special thanks to my family for funding my studies and for their constant support and encouragement.

Contents

1. Introduction	1
1.1. Motivation	1
1.2. Thesis outline	2
2. Fundamentals for modelling mechanical and electrical interactions of cells	4
2.1. Theory of continuum mechanics	4
2.1.1. Strain and stress measures	5
2.1.2. Equations of motion	7
2.1.3. Constitutive laws	8
2.1.4. Solution of the equilibrium condition	9
2.2. Maxwell's equations	12
2.3. Solution methods for time dependent problems	14
2.3.1. Explicit time integration	15
2.3.2. Implicit time integration	16
2.4. Finite element formalism	16
3. Experimental and numerical methods for cell-substrate interactions	18
3.1. Cell structure	18
3.1.1. Extracellular matrix	18
3.1.2. Cytoskeleton	20
3.1.3. Cell Adhesion	21
3.2. Experimental studies	22
3.3. Mathematical modelling	27
4. An efficient theoretical framework for cell contractility and adhesion	35
4.1. The bio-chemo-mechanical model for cell contractility	36
4.1.1. Background and assumptions	36
4.1.2. The equations	36

Contents

4.1.3. Incorporating the bio-chemo-mechanical model into the framework of continuum mechanics	38
4.2. The bio-mechanical model for cell focal adhesion	41
4.3. Finite element formulation for the coupled problem	44
4.3.1. Time discretisation for the activation level	45
4.3.2. Computation of the active stress tensor	45
4.3.3. Weak form for the coupled problem	45
4.4. Applications of the bio-chemo-mechanical model	48
4.4.1. Simulations of cells on micro-post arrays	48
4.4.2. Development of actin cytoskeleton and focal adhesion	52
5. Model order reduction of the bio-chemo-mechanical model	56
5.1. Semi-analytical formulation	56
5.2. Weak formulation for finite element implementation	60
5.3. Results and error analysis	61
5.3.1. Results	61
5.3.2. Error analysis	65
6. Numerical study on actin formation of osteoblasts on titanium arrays	68
6.1. Description for cell-pillar adhesion	69
6.2. Results and discussion	70
6.2.1. Osteoblast on arrays of titanium coated pillars of $5\mu\text{m} \times 5\mu\text{m}$. .	71
6.2.2. Osteoblast on an array of titanium coated pillars of $3\mu\text{m} \times 3\mu\text{m}$.	73
6.2.3. Effect of the adhesion scaling function	74
6.3. Conclusion	76
7. Contractility of fibroblasts and osteoblasts under DC electric field	77
7.1. Modelling the effects of DC electric field	78
7.2. Results	81
7.2.1. Magnitude of the Maxwell stress tensor	81
7.2.2. Fibroblast contractility and cytoskeleton	82
7.2.3. Dynamic changes in traction forces by osteoblasts under DC elec- tric field exposure	85
7.3. Conclusion	88
8. Summary and perspectives	90

A. FEniCS implementation for simulation of a cell on micro-post array	105
B. Stability analysis	112
C. Convergence study	113

List of Figures

2.1. Reference and current configurations to describe the motion of a body	5
2.2. A surface element in the reference (undeformed) and current (deformed) configurations	6
2.3. Example for time dependent behaviour of a displacement component u_i	15
3.1. 2D visualisation of some fundamental components of a cell and its environment	19
3.2. Different extracellular matrix proteins	19
3.3. Mechanical properties of actin, tubulin and intermediate filament polymers	20
3.4. Formation of filaments from smaller protein subunits and rapid reorganisation of the cytoskeleton in a cell in response to an external signal	21
3.5. Cell-cell and cell-matrix adhesion apparatuses	22
3.6. Some examples of force application techniques including micro-pipette aspiration, micro-needle manipulation, substrate deformation and electrical stimulation	23
3.7. Some examples of force sensing techniques including using micro-needle arrays and wrinkling membrane	25
3.8. Newtonian and compound liquid drop models	28
3.9. Maxwell liquid drop model and linear visco-elastic model	29
3.10. Mixture of four constituents in cytoplasm	31
3.11. Plot of von Mises distribution for different levels of anisotropy	32
3.12. Plots for tension-length and tension-velocity relations	33
4.1. Plot of the concentration level over time and the tension-strain rate relationship	37
4.2. Definition of fibre orientation in 2D and a possible sampling of stress fibres at every point in a 2D cell	39
4.3. Definition of fibre orientation in 3D and a possible sampling of stress fibres at every point in a 3D cell	40

List of Figures

4.4. The adhesion behaviour needs to be described as a boundary condition at the region where the cell is in contact with the substrate.	41
4.5. The bent and extended-open conformations of integrin	42
4.6. Plot for the stretch energy and its derivative with respect to the effective stretch.	43
4.7. The model for cell focal adhesion is included as a boundary condition at the region where the cell is in contact with the substrate.	44
4.8. Division of the cell body into contact and non-contact regions	46
4.9. Plots for predicted steady-state distribution of actin of smooth muscle cells on arrays of 2×2 , 3×3 and 4×4 micro-posts	50
4.10. Our FEniCS result for a single muscle cell on 5×5 posts with three different normalised bending stiffnesses	51
4.11. Our FEniCS results for a cell on an array of 5×5 posts with two different post distances	51
4.12. The shape of the fibroblast cell in our simulation and the plot for predicted steady-state distribution of actin	52
4.13. The size of a triangular and a circular cell in the simulation	53
4.14. Plots for predicted steady-state distributions of the stress fibre and high affinity integrins concentrations for a triangular cell on a ligand pattern of the same shape	54
4.15. Plots for predicted steady-state distributions of the stress fibre and high affinity integrins concentrations for a circular cell on a ligand pattern of the same shape	55
4.16. Normalised concentrations of high and low affinity integrins for the circular cell	55
5.1. A possible configuration for the activation level at a point in 2D using the classical representation and our approximation using a 2D quadratic form	57
5.2. A possible configuration for the activation level at a point in 3D using the classical representation and our approximation using a 3D quadratic form	58
5.3. Cell under bi-axial isometric tension and the plot for the normalised active stress over time	62
5.4. Dimensions of a 3D round cell, the mesh and plot for the average activation level at the steady state	64

List of Figures

5.5. The plot for the differences in minimum and maximum activation level at any point in the cell.	65
5.6. The distribution of average activation level at four selected times	66
5.7. The three points of interest and the plot of relative error in cell displacement	66
6.1. Plot of an exemplary function for the concentration level of the adhesion on a single pillar and plot of a slice through two spots	69
6.2. Fluorescence image of the actin filament distribution in MG-63 osteoblasts, sketch of the patch of a cell used in the simulation and our predicted result for actin distribution using the bio-chemo-mechanical model and our description for the cell-pillar adhesion	72
6.3. Experimental result, sketch of an osteoblast on an array of $5\mu\text{m} \times 5\mu\text{m}$ pillars and our simulation result for this cell	73
6.4. Experimental result for the actin distribution of a MG-63 osteoblast on $3\mu\text{m} \times 3\mu\text{m}$ pillar structures, dimensions of the pillars and sketch of the cell used in the simulation	73
6.5. Experimental and simulated results for actin distribution of an osteoblast on an array of $3\mu\text{m} \times 3\mu\text{m}$ pillars	74
6.6. Different adhesion scaling functions for a single pillar obtained by changing the size and the number of spots	74
6.7. Predicted results for actin distribution of an osteoblast on an array of 19 pillars using different adhesion scaling functions	76
7.1. A possible scaling function to represent the raise of the maximum tension in the direction parallel to the electric field and a possible function to represent stimulation of the active stress in different directions at four time periods.	79
7.2. An exemplary function for the scaling of the adhesion between the cell and the substrate and plot for the scaling function on a line through the cell and parallel to the electric field.	80
7.3. Sketch of a typical cell under a DC electric field exposure and plot of electric field norm	81
7.4. Plot of the components of the Maxwell stress tensor	82
7.5. Shape and size of a fibroblast cell used in our simulation and the scaling function for the adhesion.	83
7.6. Change of the bounding box of a fibroblast cell over time.	84

List of Figures

7.7. Two osteoblast-like cells of different shape are investigated in our simulation where their geometries are constructed based on the images obtained in existing experiments	86
7.8. The change over time of the bounding box around every cell in the direction along parallel and perpendicular to the electric field and our simulation results for different values of maximum fibre tension	87
7.9. Dynamic change of the difference in substrate displacements near the cell peripheries obtained in our simulations	89
A.1. Mesh and physical regions for cell on 2×2 pillars that are stored in a hdf5 file. The number of mesh cells is 15 624, while the numbers of degrees of freedom for the deformation and the activation are 31 826 and 562 464, respectively.	107
B.1. Plot for the average activation at a point in the cell over time for different time steps used.	112
C.1. Plot of the magnitudes of cell displacement and the relative errors $\ u_k - u_{k-1}\ /\ u_k\ $ for meshes of different sizes.	113

1. Introduction

1.1. Motivation

The quality of tissue engineered implants has been improved in the last decades thanks to the rapid development of tissue engineering, in which scientific principles are applied to the design, construction, modification, growth, and maintenance of living tissues [5, 7, 82]. Producing implants having the same structural organisation and functionality as the healthy tissue *in vivo* is the final objective of tissue engineering. In order to achieve this goal, it is crucial to understand and utilise various stimuli in the human body that control the development and maintenance of the tissue structure and functionality [5, 8]. Besides biochemical cues, biophysical or mechanical stimuli are necessary to achieve the desired functionality and texture of the engineered tissue. While these stimuli, together with chemical, material-based and magnetic cues, are well-established tools in the *in vitro* production of tissues and organs, electrical stimulation with its importance in the physiology and development of the majority of all human tissues has become a potential type of stimulus for further improvement of implants [5].

To efficiently employ these stimuli, it is essential to understand the underlying mechanisms of the interactions between cells and their surrounding environment as they could give us a better control over cell growth, cell contraction, cell migration, adhesion, and orientation. An important aspect is to understand cellular forces, as they are crucial for many biological processes [47, 50]. A great number of experiments have been carried out to study the mechanisms for force generation of cells and their mechanical response to external stimuli such as stretching, compressing, ultrasound and electrical stimulation. Besides experimental techniques, mathematical modelling has been a powerful tool to interpret the cellular behaviours. A great number of numerical models with different scales and complexities have been proposed to analyse the cellular processes. The two main classes of these models include micro/nano-structural approaches and continuum-based approaches. While the former is required to model phenomena in small scales,

1. *Introduction*

such as in protein folding and fracture, the latter is more widely applied to interpret the results on cellular responses using common experimental methods [106]. In continuum models, the cell material is usually assumed to be passive. Recently, the active nature of the cell has been addressed using several approaches and the models could predict better many experimental results [73]. For example, when the dynamic reorganisation of the cytoskeleton is taken into account, some models could simulate very well the high concentration of stress fibres at focal adhesions or the influence of substrate stiffness on the forces generated by the cells.

The effects of electrical stimulation on cell contractility and the formation of actin filaments have been investigated experimentally [5, 14, 36]. However, they are not incorporated in most of the computational models. The objective of this thesis is to obtain a numerical model for the mechanical responses of cells, where the influence of the external electric field is addressed. In addition, a mathematical description for the adhesion between the cell and the substrate is also to be proposed. The model should capture several outcomes from the experiments on osteoblast cells which have been carried out at the DFG Research Training Group 1505/2 “*welisa*” [55]. For instance, the formation of actin in osteoblasts when they are cultured on titanium substrates of different geometries. Moreover, the model should also be applicable to simulate the contraction and cytoskeleton of different cell types when they are exposed to an external electric field, as presented in existing literature.

1.2. Thesis outline

The thesis is organised as follow. Chapter 1 introduces the research topic and the overview of the thesis. Chapter 2 provides the basic concepts and the essential equations used in numerical models that are based on the theory of continuum mechanics and electromagnetics. A brief introduction to the techniques for solving these equations is also presented. In Chapter 3, the structure and major components of biological cells are introduced. Moreover, experimental techniques and numerical methods that have been used to investigate the interactions between cells and their substrates are reviewed. Chapter 4 represents the concepts and the formulation of a bio-chemo-mechanical model that has been shown to be more advantageous compared to other mathematical descriptions. As this model is very efficient, it is used as a foundation for the development of our numerical model. In addition, a bio-mechanical model for cell adhesion that can be com-

1. *Introduction*

bined with this model is also presented. Our approach for an efficient implementation is shown by presenting the finite element formulation for the coupling of this model to the equations of continuum mechanics and the steps to transform it to software code. The results using our implementation are compared to those presented in the literature. The advantages of these models are demonstrated by their applications in the predictions of several experimental studies. Chapter 5 presents our approach to reduce the complexity of the model, while retaining its significant features. In Chapter 6, our description for the adhesion between cell and substrate is proposed so that the model can capture the formation of actin in osteoblasts when they are laid on titanium pillar structures. Our suggestion for addressing the effects of external electric field is presented in Chapter 7. The proposed idea gives the model the capacity to simulate the contractility of different cell types under the presence of electric field exposure. Finally, Chapter 8 includes some discussion and perspectives for future research.

2. Fundamentals for modelling mechanical and electrical interactions of cells

A class of computational models for mechanical responses of cells is based on continuum mechanics, while the theory of electromagnetics is used to study electrical properties of the cells. In this chapter, the main concepts and the elementary equations in these two fields of physics are presented. Moreover, the approaches for time discretisation and the finite element formulation for solving the partial differential equations are also described.

2.1. Theory of continuum mechanics

In this section, a short overview of continuum mechanics, the governing equations as well as the formulation suitable for the application of finite element analysis are represented. A more comprehensive introduction to the mechanics of structures can be found in [6], while extensive formulations of non-linear finite element methods are presented in [12], [13] and [110].

The motion of a body can be described by a function $\phi(\mathbf{X}, t)$ of material coordinates \mathbf{X} and time t which determines the spatial positions of the material points $\mathbf{x} = \phi(\mathbf{X}, t)$. Let $\mathbf{u} = \mathbf{x} - \mathbf{X}$ be the displacement vector, then the *deformation gradient* of the transformation from reference to current configuration can be written as:

$$\mathbf{F} = \frac{\partial \mathbf{x}}{\partial \mathbf{X}} = \frac{\partial}{\partial \mathbf{X}}(\mathbf{X} + \mathbf{u}) = \mathbf{I} + \nabla \mathbf{u} \quad (2.1)$$

where \mathbf{I} represents the identical transformation. The determinant of the deformation gradient, $J = \det \mathbf{F}$, is called the *Jacobian* of the deformation and expresses the ratio between the deformed and undeformed infinitesimal volume elements. As both volume elements are positive for realistic deformations, J is a positive number and \mathbf{F} is an invertible tensor.

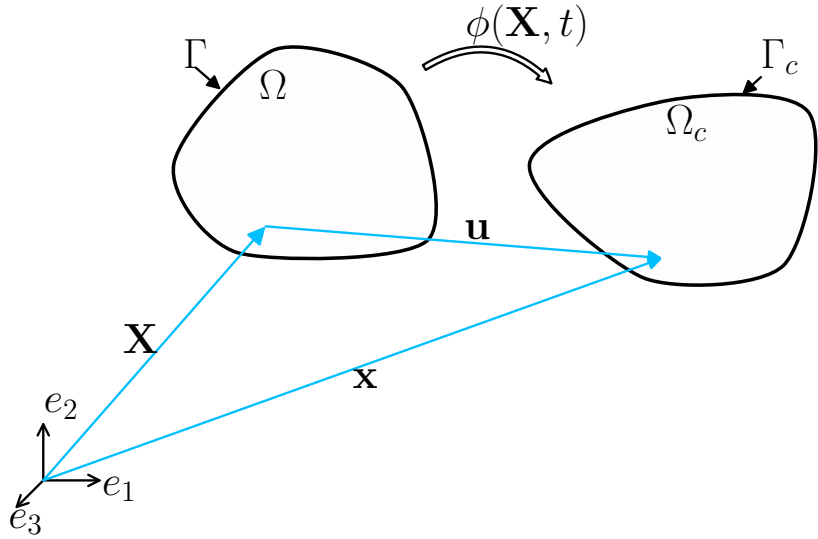


Figure 2.1: Reference and current configuration to describe the motion of a body. Figure adapted from [110].

2.1.1. Strain and stress measures

In continuum mechanics, several stress measures can be defined and they are usually related by transformations between the reference and the current configurations. The analysis of the structure can be performed using different theories (e.g. infinitesimal strain theory, large strain theory), depending on the amount of the deformation. In each theory, a different strain measure is used.

Strain measures

When a structure deforms, the strain represents the displacement between particles in the body relative to a reference configuration. For geometrically linear analysis, in which the displacement vector and its gradient are much smaller compared to unity (i.e., $\|\mathbf{u}\| \ll 1$ and $\|\nabla \mathbf{u}\| \ll 1$), the linear strain tensor:

$$\boldsymbol{\varepsilon} = \frac{1}{2} (\nabla^\top \mathbf{u} + \nabla \mathbf{u}) \quad (2.2)$$

which is the symmetric part of the gradient of the deformation vector, is usually used. This strain tensor is also called Cauchy's strain tensor or small strain tensor.

2. Fundamentals for modelling mechanical and electrical interactions of cells

For large deformation of the structure, the Green-Lagrange strain measure:

$$\mathbf{E} = \frac{1}{2} (\mathbf{F}^\top \cdot \mathbf{F} - \mathbf{I}) = \frac{1}{2} (\nabla^\top \mathbf{u} + \nabla \mathbf{u} + \nabla^\top \mathbf{u} \cdot \nabla \mathbf{u}) \quad (2.3)$$

is used. Here, the symmetric tensor $\mathbf{C} = \mathbf{F}^\top \cdot \mathbf{F}$ is also called the right Cauchy-Green tensor and is mathematically convenient in formulating constitutive laws. The Green-Lagrange strain tensor is then written as $\mathbf{E} = \frac{1}{2}(\mathbf{C} - \mathbf{I})$. It can be seen that the Cauchy's strain tensor is actually a linearisation of the Green-Lagrange strain tensor, where the second-order terms are neglected.

Stress measures

The Cauchy stress, or physical stress, is defined as the total force per unit area in the current configuration. For a given vector element of surface, let $d\Gamma$ and \mathbf{n} be the area

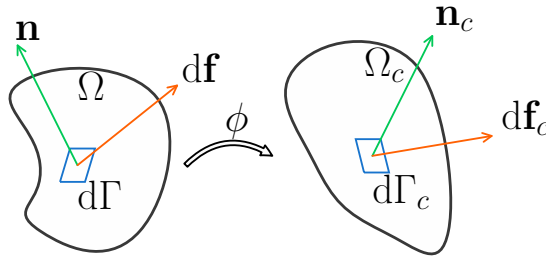


Figure 2.2: A surface element in the reference (undeformed) and current (deformed) configurations. Figure adapted from [6].

and the outward normal of the element, respectively, in the reference configuration. The surface element is subjected to a traction \mathbf{t} leading to a force vector $d\mathbf{f} = \mathbf{t}d\Gamma$. Assuming that the area becomes $d\Gamma_c$ with outward normal \mathbf{n}_c and traction vector \mathbf{t}_c leading to a force $d\mathbf{f}_c$ after the deformation, the Cauchy stress σ can be written as:

$$\mathbf{n}_c \cdot \sigma d\Gamma_c = d\mathbf{f}_c = \mathbf{t}_c d\Gamma_c. \quad (2.4)$$

For geometrically nonlinear analysis, stress measures in undeformed configuration are used. The nominal stress, or first Piola-Kirchhoff stress, \mathbf{P} is given by:

$$\mathbf{n} \cdot \mathbf{P} d\Gamma = d\mathbf{f}_c = \mathbf{t}_c d\Gamma_c. \quad (2.5)$$

The second Piola-Kirchhoff stress \mathbf{S} is defined in a similar way, but unlike the nominal stress, the force vector $d\mathbf{f} = \mathbf{F}^{-1} \cdot d\mathbf{f}_c$ in the reference configuration is used:

$$\mathbf{n} \cdot \mathbf{S} d\Gamma = \mathbf{F}^{-1} \cdot d\mathbf{f}_c = \mathbf{F}^{-1} \cdot \mathbf{t} d\Gamma \quad (2.6)$$

2. Fundamentals for modelling mechanical and electrical interactions of cells

Alternatively, this stress tensor can be written as

$$\mathbf{S} = J\mathbf{F}^{-1} \cdot \boldsymbol{\sigma} \cdot (\mathbf{F}^{-1})^\top \quad (2.7)$$

which is a transformation of the Cauchy stress into the reference configuration. Since the Cauchy stress is symmetric, so is the second Piola-Kirchhoff stress.

2.1.2. Equations of motion

Consider an arbitrary subdomain of the body Ω with boundary Γ . Suppose that the body has the density ρ_c and is subjected to the surface traction \mathbf{t}_c and the body force $\rho_c \mathbf{b}$ in the current configuration, where \mathbf{b} is a force per unit mass. The conservation of mass gives the relation $\rho = J\rho_c$ with ρ being the density in the reference configuration and $J = \det \mathbf{F}$. In case of geometrically linear analysis, the Cauchy motion equation in the so-called *Euler formulation* is given by:

$$\rho_c \ddot{\mathbf{u}} = \nabla \sigma + \rho_c \mathbf{b} \quad \forall \mathbf{x} \in \Omega_c \quad (2.8)$$

where $\nabla \sigma$ represents the divergence of $\boldsymbol{\sigma}$ with respect to the current configuration ($\frac{\partial \sigma_{ij}}{\partial x_j}$). The static equilibrium is obtained by eliminating the inertia term:

$$\nabla \sigma + \rho_c \mathbf{b} = \mathbf{0} \quad \forall \mathbf{x} \in \Omega_c. \quad (2.9)$$

At the boundaries that are subjected to surface traction, the boundary condition:

$$\boldsymbol{\sigma} \cdot \mathbf{n}_c = \mathbf{t}_c \quad \forall \mathbf{x} \in \Gamma_\sigma \quad (2.10)$$

should be satisfied.

For geometrically nonlinear analysis, it is convenient to utilise the motion equation in the so-called *Lagrange formulation*, which is obtained by relating the Cauchy equation of motion to the reference configuration. This can be done by first multiplying the motion equation (2.8) by $J = \det \mathbf{F}$ and applying the identity $J\nabla \sigma = \nabla(\mathbf{F} \cdot \mathbf{S})$, where \mathbf{S} is the second Piola-Kirchhoff stress tensor. The derivation of this identity is presented in [6], [48]. Note that $\nabla(\mathbf{F} \cdot \mathbf{S})$ represents the divergence of $\mathbf{F} \cdot \mathbf{S}$ with respect to the reference configuration ($\partial/\partial X_j$). The equation of motion in the Lagrangian formulation is obtained as:

$$\rho \ddot{\mathbf{u}} = \nabla(\mathbf{F} \cdot \mathbf{S}) + \rho \mathbf{b} \quad \forall \mathbf{X} \in \Omega \quad (2.11)$$

The condition for static equilibrium is then written as:

$$\nabla(\mathbf{F} \cdot \mathbf{S}) + \rho \mathbf{b} = \mathbf{0} \quad \forall \mathbf{X} \in \Omega. \quad (2.12)$$

2. Fundamentals for modelling mechanical and electrical interactions of cells

The traction boundary condition is described in the reference configuration as:

$$\mathbf{F} \cdot \mathbf{S} \cdot \mathbf{n} = \mathbf{T}^* \quad \forall \mathbf{X} \in \Gamma_\sigma \quad (2.13)$$

where \mathbf{T}^* is the traction applied on an undeformed body.

2.1.3. Constitutive laws

The relationship between the stress and the strain (and hence the displacement) characterises the response of the material under loading and is called the constitutive equation. This section presents some material models that are used in our simulations of cells, including linear elasticity and hyperelasticity.

Linear elasticity

The response of the material may be considered to be linearly elastic when the structure undergoes a small deformation and rotation. The Cauchy stress and linear strain tensors are used and the relationship between them can be generally written as

$$\boldsymbol{\sigma} = \mathcal{C} : \boldsymbol{\varepsilon} \quad (2.14)$$

where \mathcal{C} is a fourth-order tensor which is called the stiffness tensor or elasticity tensor. For an isotropic linearly elastic material, the tensor \mathcal{C} has 21 independent components and is written as

$$\mathcal{C} = \lambda \mathbf{I} \otimes \mathbf{I} + 2\mu \mathbf{I}$$

where \mathbf{I} is the unit tensor and the two independent material constants λ and μ are called the Lamé constants which can be expressed in terms of the Young's modulus E and the Poisson's ratio ν as

$$\lambda = \frac{E\nu}{(1+\nu)(1-2\nu)}, \quad \mu = \frac{E}{2(1+\nu)}$$

Thus, the stress-strain relation for an isotropic linear elastic material is obtained as

$$\boldsymbol{\sigma} = \lambda \text{tr}(\boldsymbol{\varepsilon}) \mathbf{I} + 2\mu \boldsymbol{\varepsilon} \quad (2.15)$$

This relation can also be derived from $\boldsymbol{\sigma} = \frac{\partial W}{\partial \boldsymbol{\varepsilon}}$, where W is the strain energy per unit volume and is given as a function of the strain tensor as:

$$W(\boldsymbol{\varepsilon}) = \frac{\lambda}{2} \text{tr}(\boldsymbol{\varepsilon})^2 + \mu \text{tr}(\boldsymbol{\varepsilon}^2) \quad (2.16)$$

Hyperelasticity

Hyperelastic materials are elastic materials for which the work done on the material is independent of the load path [6]. The stress-strain relationship for elastic material models is derived from a strain energy density function. Many hyperelastic models have been developed, but only two of them are presented here.

Saint Venant–Kirchhoff model The Saint Venant–Kirchhoff model is the simplest hyperelastic material model and is an extension of the linear elastic material model. The strain energy density function for the St. Venant–Kirchhoff model is given by:

$$W(\mathbf{S}) = \frac{\lambda}{2} \operatorname{tr}(\mathbf{E})^2 + \mu \operatorname{tr}(\mathbf{E}^2)$$

Then the relationship between the second Piola-Kirchhoff stress \mathbf{S} and the Green-Lagrange strain \mathbf{E} is obtained as:

$$\mathbf{S} = \frac{\partial W}{\partial \mathbf{E}} = \lambda \operatorname{tr}(\mathbf{E}) \mathbf{I} + 2\mu \mathbf{E} \quad (2.17)$$

Neo-Hookean material The strain energy density function for an compressible neo-Hookean material is expressed in terms of the right Cauchy-Green tensor $\mathbf{C} = \mathbf{F}^\top \cdot \mathbf{F}$ and is given by

$$W(\mathbf{C}) = \frac{\mu}{2}(I_C - 3) - \mu \ln J + \frac{\lambda}{2}(\ln J)^2,$$

where $I_C = \operatorname{tr} \mathbf{C}$ and $J = \det \mathbf{F}$. The stress is then derived as:

$$\mathbf{S} = \frac{\partial W}{\partial \mathbf{E}} = 2 \frac{\partial W}{\partial \mathbf{C}} = \mu(\mathbf{I} - \mathbf{C}^{-1}) + \lambda \ln J \mathbf{C}^{-1}.$$

2.1.4. Solution of the equilibrium condition

Given a structure that is subjected to some forces (e.g. body force, surface traction) and supports, its deformation can be obtained by solving a coupled system of partial differential equations which include the kinematical relations, the equation of motion and the constitutive law. For Lagrangian description, the use of the second Piola-Kirchhoff stress tensor leads to the following equations:

Kinematics:	$\mathbf{E} = \frac{1}{2} (\mathbf{F}^\top \cdot \mathbf{F} - \mathbf{I})$
Equilibrium:	$\rho \ddot{\mathbf{u}} = \nabla(\mathbf{F} \cdot \mathbf{S}) + \rho \mathbf{b} \quad \forall \mathbf{X} \in \Omega$
Constitutive law:	$\mathbf{S} = \frac{\partial W}{\partial \mathbf{E}}$

2. Fundamentals for modelling mechanical and electrical interactions of cells

In addition, let $\Gamma = \partial\Omega$ be the boundary of the subdomain Ω , the displacement boundary conditions are prescribed on Γ_u and the traction boundary conditions are formulated on Γ_σ as:

$$\mathbf{u}(\mathbf{X}) = \mathbf{u}^*(\mathbf{X}), \quad \forall \mathbf{X} \in \Gamma_u, \quad \mathbf{F} \cdot \mathbf{S} \cdot \mathbf{N} = \mathbf{T}^*, \quad \forall \mathbf{X} \in \Gamma_\sigma$$

The above system of partial differential equations can only be solved analytically in some trivial cases. In practice, an approximate solution for this set of equations is obtained using numerical methods such as finite difference or finite element, where the latter is more widely used. For the use of finite element method, a variational formulation of the equations is required. Two approaches that can be used to derive the variational formulation are the uses of the principle of virtual work and the minimum total potential energy principle.

The principle of virtual work

The weak form of the governing equations is obtained by multiplying the Eq. (2.11) by a test function $\delta\mathbf{u}$ and integrating the product over the domain of the body:

$$\int_{\Omega} \delta\mathbf{u} \cdot \ddot{\mathbf{u}} \rho dV = \int_{\Omega} \delta\mathbf{u} \cdot \nabla(\mathbf{F} \cdot \mathbf{S}) dV + \int_{\Omega} \delta\mathbf{u} \cdot \mathbf{b} \rho dV \quad (2.18)$$

where the test function $\delta\mathbf{u}$ has to vanish on the prescribed displacement boundary Γ_u . The above weak form is known as principle of virtual work in classical mechanics and the test function $\delta\mathbf{u}$ is also called virtual displacement. The approach using weak form is suitable for general problems, for example, inelastic materials, since the assumptions such as existence of a potential function are not required.

By applying the product rule $\delta\mathbf{u} \cdot \nabla(\mathbf{F} \cdot \mathbf{S}) = \nabla(\delta\mathbf{u} \cdot (\mathbf{F} \cdot \mathbf{S})) - \nabla\delta\mathbf{u} : (\mathbf{F} \cdot \mathbf{S})$ and the divergence theorem for the integral of the term $\nabla(\delta\mathbf{u} \cdot (\mathbf{F} \cdot \mathbf{S}))$, the weak form becomes:

$$\int_{\Omega} \delta\mathbf{u} \cdot \ddot{\mathbf{u}} \rho dV + \int_{\Omega} \nabla\delta\mathbf{u} : (\mathbf{F} \cdot \mathbf{S}) dV = \int_{\Omega} \delta\mathbf{u} \cdot \mathbf{b} \rho dV + \int_{\Gamma_\sigma} \delta\mathbf{u} \cdot \mathbf{T}^* dA \quad (2.19)$$

The second term on the left hand side can be expressed in terms of the variation of the Green-Lagrange strain tensor $\delta\mathbf{E}$. Using the fact that the scalar product of a symmetric tensor with the antisymmetric part of a tensor is zero, the following identity is obtained [110]:

$$\begin{aligned} \delta\mathbf{E} : \mathbf{S} &= \frac{1}{2} \delta(\mathbf{F}^\top \cdot \mathbf{F} - \mathbf{I}) : \mathbf{S} = \frac{1}{2} (\delta\mathbf{F}^\top \cdot \mathbf{F} + \mathbf{F}^\top \cdot \delta\mathbf{F}) : \mathbf{S} \\ &= \mathbf{F}^\top \delta\mathbf{F} : \mathbf{S} = \delta\mathbf{F} : \mathbf{F} \cdot \mathbf{S} \end{aligned} \quad (2.20)$$

2. Fundamentals for modelling mechanical and electrical interactions of cells

here $\delta\mathbf{F}$ is the variation of the deformation gradient and is obtained by its definition and by the fact that the coordinates of the reference configuration are unchanged as:

$$\delta\mathbf{F} = \frac{\partial}{\partial\mathbf{X}}(\delta\mathbf{X} + \delta\mathbf{u}) = \frac{\partial\delta\mathbf{u}}{\partial\mathbf{X}} = \nabla\delta\mathbf{u} \quad (2.21)$$

With the above two identities, the principle of virtual work can be now written as:

$$\int_{\Omega} \delta\mathbf{u} \cdot \ddot{\mathbf{u}} \rho dV + \int_{\Omega} \delta\mathbf{E} : \mathbf{S} dV = \int_{\Omega} \delta\mathbf{u} \cdot \mathbf{b} \rho dV + \int_{\Gamma_{\sigma}} \delta\mathbf{u} \cdot \mathbf{T}^* dA \quad (2.22)$$

The first term in the left hand side is called the virtual work of inertial forces δW_{dyn} , while the second term is the internal virtual work δW_{int} . The sum in the right hand side is the virtual work of external forces δW_{ext} .

The principle of minimum potential energy

For hyperelastic materials, which are characterised by the existence of a strain energy function, a preferable approach to obtain the solution for the static problem is to solve a potential energy minimisation problem. The functional for the total potential energy Π associated with a body can be stated as:

$$\Pi(\mathbf{u}) = \Pi_{\text{int}}(\mathbf{u}) + \Pi_{\text{ext}}(\mathbf{u}) \quad (2.23)$$

Here, the internal potential energy Π_{int} can be expressed in term of the stored strain energy density $W(\mathbf{C})$ as:

$$\Pi_{\text{int}}(\mathbf{u}) = \int_{\Omega} W(\mathbf{C}(\mathbf{u})) dV, \quad (2.24)$$

while the external potential energy Π_{ext} due to body forces and surface traction is given as:

$$\Pi_{\text{ext}}(\mathbf{u}) = - \int_{\Omega} \rho \mathbf{b} \cdot \mathbf{u} dV - \int_{\Gamma_{\sigma}} \mathbf{T}^* \cdot \mathbf{u} dA, \quad (2.25)$$

The minimum total potential energy principle states that the deformations which fulfil the equilibrium condition minimise the total potential energy. Minimisation of Π involves solving the stationary condition $F(\mathbf{u}, \mathbf{w}) = 0$, where the directional derivative $F(\mathbf{u}, \mathbf{w})$ at \mathbf{u} along the direction \mathbf{w} is given as:

$$F(\mathbf{u}, \mathbf{w}) := D\Pi(\mathbf{u}) \cdot \mathbf{w} = \frac{d}{d\alpha} \Pi(\mathbf{u} + \alpha\mathbf{w}) \Big|_{\alpha=0} \quad (2.26)$$

2. Fundamentals for modelling mechanical and electrical interactions of cells

With the definition of the total potential energy and by applying the chain rule for the derivative w.r.t. α of Π_{int} , the directional derivative becomes:

$$F(\mathbf{u}, \mathbf{w}) = \int_{\Omega} \frac{\partial W}{\partial \mathbf{C}} : D\mathbf{C} \cdot \mathbf{w} \, dV - \int_{\Omega} \rho \mathbf{b} \cdot \mathbf{w} \, dV - \int_{\Gamma_{\sigma}} \mathbf{T}^* \cdot \mathbf{w} \, dA \quad (2.27)$$

From the relationship between the right Cauchy-Green strain tensor \mathbf{C} and the Green-Lagrange strain tensor \mathbf{E} , the identity $D\mathbf{C} \cdot \mathbf{w} = 2D\mathbf{E} \cdot \mathbf{w}$, or $\delta\mathbf{C} = 2\delta\mathbf{E}$, is obtained. Together with the definition of the second Piola-Kirchhoff stress tensor via the strain energy function, $\mathbf{S} = 2\partial W/\partial\mathbf{C}$, the following equation is obtained:

$$F(\mathbf{u}, \mathbf{w}) = \int_{\Omega} \mathbf{S} : \delta\mathbf{E} \, dV - \int_{\Omega} \rho \mathbf{b} \cdot \mathbf{w} \, dV - \int_{\Gamma_{\sigma}} \mathbf{T}^* \cdot \mathbf{w} \, dA = 0 \quad (2.28)$$

which is equivalent to the weak form (2.22) for static equilibrium.

2.2. Maxwell's equations

In this section, the fundamental equations in electricity and magnetism are described. Depending on the problem, different assumptions can be made and the equations can be simplified. A very short description of the Maxwell's stress tensor that has been applied in molecular biology is also given. An extensive introduction to electrodynamics can be found in [30], while the classification of the problems in electrical engineering as well as solution methods are presented comprehensively in [104].

All electromagnetic phenomena can be described by a set of equations, the Maxwell's equations. They include four first-order partial differential equations which are stated as follows:

$$\nabla \times \mathbf{E} = -\frac{\partial \mathbf{B}}{\partial t} \quad (2.29)$$

$$\nabla \times \mathbf{H} = \mathbf{J} + \frac{\partial \mathbf{D}}{\partial t} \quad (2.30)$$

$$\nabla \cdot \mathbf{D} = \rho \quad (2.31)$$

$$\nabla \cdot \mathbf{B} = 0 \quad (2.32)$$

where \mathbf{E} is the electric field intensity (V/m), \mathbf{D} is the electric flux density which is also known as displacement field (As/m²), \mathbf{H} is the magnetic field intensity (A/m), \mathbf{B} is the magnetic induction (Vs/m²), \mathbf{J} is the electric current density (A/m²), and ρ is the space charge density (As/m³).

2. Fundamentals for modelling mechanical and electrical interactions of cells

In addition, a set of equations that specifies the relations between the quantities, for example between \mathbf{D} and \mathbf{E} , between \mathbf{H} and \mathbf{B} should be supplied. These relations are specific to a material or substance and are called constitutive equations. For linear and isotropic media, the following laws are given:

$$\mathbf{J} = \kappa \mathbf{E} \quad (2.33)$$

$$\mathbf{D} = \varepsilon \mathbf{E} \quad (2.34)$$

$$\mathbf{B} = \mu \mathbf{H} \quad (2.35)$$

where κ is the electrical conductivity (S/m), ε is the electric permittivity (As/Vm) and μ is the magnetic permeability (Vs/Am).

Continuity equation The principle of charge conservation states that electric charge can neither be created nor destroyed. Local conservation of charge is a consequence of the laws of electrodynamics and its mathematical statement can be derived from Maxwell's equations [30]. By taking the divergence of Eq. (2.30) and using the fact that $\nabla \cdot (\nabla \times \mathbf{H}) = 0$, we obtain the identity:

$$\nabla \cdot \mathbf{J} = -\nabla \cdot \frac{\partial \mathbf{D}}{\partial t} \quad (2.36)$$

Now if we interchange the space and time derivatives on the right hand side and apply Eq. (2.30), we get:

$$\nabla \cdot \mathbf{J} = -\frac{\partial \rho}{\partial t} \quad (2.37)$$

This is called continuity equation [104].

Stationary current fields A stationary current (which is also called steady current, time-independent current, or constant current) is a type of direct current whose intensity does not vary over time. Since charge is not piling up anywhere in a constant current, $\partial \rho / \partial t = 0$ and the continuity equation becomes:

$$\nabla \cdot \mathbf{J} = 0 \quad (2.38)$$

with $\mathbf{J} = \kappa \mathbf{E}$ being the electric current density. Here, κ is the conductivity of the medium and is a constant. Moreover, since the process is steady, the magnetic field generated by a stationary current is a constant over time. Hence, $\nabla \times \mathbf{E} = \mathbf{0}$ (from

2. Fundamentals for modelling mechanical and electrical interactions of cells

Eq. 2.29) and the electric field can be uniquely described by a scalar potential function [104]:

$$\mathbf{E} = -\nabla\phi \quad (2.39)$$

Hence, Eq. (2.38) can be written as:

$$\kappa\nabla \cdot \mathbf{E} = -\kappa\nabla \cdot \nabla\phi = 0 \quad (2.40)$$

which means that the potential satisfies Laplace's equation $\Delta\phi = 0$

Maxwell's stress tensor The Maxwell's stress tensor is used to represent the interaction between electromagnetic forces and mechanical momentum [30]. It is convenient for finding the total electromagnetic force on a body. It has been used to examine electrical interactions along and between molecules at cell-matrix and cell-surface interface, as well as within tissues [31].

Suppose that a medium has a constant permeability μ and a constant permittivity ϵ and experiences an electric field \mathbf{E} and a magnetic field \mathbf{B} . Components of the Maxwell's stress tensor \mathbf{S}^{el} are given as:

$$S_{ij}^{\text{el}} = \epsilon \left(E_i E_j - \frac{1}{2} \delta_{ij} E^2 \right) + \frac{1}{\mu} \left(B_i B_j - \frac{1}{2} \delta_{ij} B^2 \right), \quad i, j \in \{1, 2, 3\} \quad (2.41)$$

where E_i and B_i are components of the electric field and magnetic field, respectively, and δ_{ij} is the Kronecker delta function [30]. The magnitudes of the electric field and the magnetic field are computed as $E = \sqrt{E_1^2 + E_2^2 + E_3^2}$ and $B = \sqrt{B_1^2 + B_2^2 + B_3^2}$, respectively.

2.3. Solution methods for time dependent problems

In modelling the process of the deformation of structures, the change of state variables and deformations in time has to be considered. The time evolution of a variable u can generally be written as:

$$\frac{\partial u}{\partial t} = F(u) \quad (2.42)$$

where the discretisation of the spatial domain can be described in the function F . An example is the diffusion problem:

$$\frac{\partial u}{\partial t} = \Delta u + f \quad \text{in } \Omega, \quad \text{for } t > 0 \quad (2.43)$$

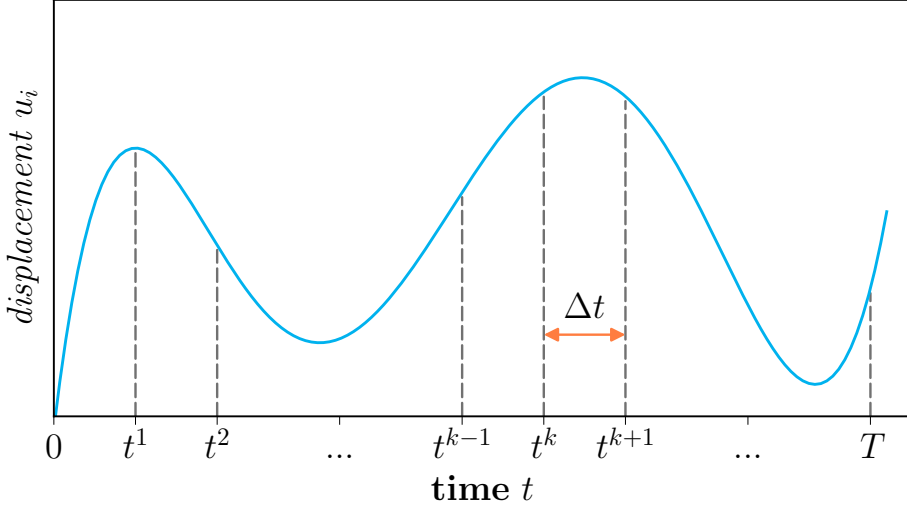


Figure 2.3: Time dependent behaviour of a displacement component u_i . Figure adapted from [110].

where f is a prescribed function and Δ is the Laplace operator.

The first-order temporal discretisation using backward differences is written as:

$$\frac{u^{k+1} - u^k}{\Delta t} = F(u) \quad (2.44)$$

where the superscripts $k, k+1$, respectively, indicate the current time level and the next time level. Here, the time interval $0 \leq t \leq T$ is subdivided into multiple time steps Δt , as depicted in Fig. 2.3. The function $F(u)$ can be evaluated using explicit or implicit time integration.

2.3.1. Explicit time integration

In this method, the function $F(u)$ is evaluated at the current time:

$$\frac{u^{k+1} - u^k}{\Delta t} = F(u^k) \quad (2.45)$$

and the value at the next time level can be explicitly computed from the existing values u^k :

$$u^{k+1} = u^k + \Delta t F(u^k) \quad (2.46)$$

2.3.2. Implicit time integration

This method evaluates the function $F(u)$ at the next time:

$$\frac{u^{k+1} - u^k}{\Delta t} = F(u^{k+1}) \quad (2.47)$$

This leads to an implicit relation between the value at the current and the following time step:

$$u^{k+1} - \Delta t F(u^{k+1}) = u^k \quad (2.48)$$

To obtain the value of u^{k+1} , this implicit equation can be solved using iterations.

2.4. Finite element formalism

In order to apply finite element methods for the solution of partial differential equations (PDEs), the mathematical model is often formulated as a *variational problem*. A usual approach is to multiply the PDE by a function v , which is called a *test function*, and perform an integration over the domain Ω . The variable u , whose approximate solution to be sought, is also called a *trial function*, and the integral representation of the equation is called a *weak form*. The key idea of finite element methods is to solve the variational problem on a finite-dimensional (discrete) space instead of an infinite-dimensional (continuous) space [53, 110].

Linear problems

A linear variational problem can be generally written in the form: find $u \in V$ such that

$$a(u, v) = L(v), \quad \text{for } v \in \hat{V}, \quad (2.49)$$

where V is the trial space and \hat{V} is the test space. Here the functional $a : V \times \hat{V} \rightarrow \mathbb{R}$ is a bilinear form and $L : \hat{V} \rightarrow \mathbb{R}$ is a linear form. The restriction of the above problem to a finite-dimensional space can be stated as: find $u_h \in V_h \subset V$ such that

$$a(u_h, v) = L(v) \quad \forall v \in \hat{V}_h \subset V. \quad (2.50)$$

In order to approximate the primary field variables, ansatz functions have to be chosen. The approximation of the exact solution of the mathematical model is done using an ansatz as:

$$u_{\text{exact}} \approx u_h = \sum_{i=1}^n N_i u_i, \quad (2.51)$$

2. Fundamentals for modelling mechanical and electrical interactions of cells

where $(u_1, \dots, u_n) \in \mathbb{R}^n$ is the vector of degrees of freedom to be computed and $\{N_i\}_{i=1}^n$ is a basis for V_h . Here, the space V_h has the dimension of n . Let $\{\hat{N}_i\}_{i=1}^n$ be a basis for the test space \hat{V}_h and take $v = \hat{N}_i$, for $i = 1, 2, \dots, n$, the condition that u_h is a solution of the variational problem leads to:

$$\sum_{i=1}^n u_i a(N_i, \hat{N}_i) = L(\hat{N}_i), \quad i = 1, 2, \dots, n. \quad (2.52)$$

The coefficient vector $\mathbf{u} = (u_1, \dots, u_n)$ can be obtained by solving a linear system $\mathbf{A}\mathbf{u} = \mathbf{b}$, where the components A_{ij} of the matrix \mathbf{A} and b_i of the vector \mathbf{b} are defined as:

$$\begin{aligned} A_{ij} &= a(N_i, \hat{N}_i), \\ b_i &= L(\hat{N}_i) \end{aligned}$$

for $i, j = 1, 2, \dots, n$.

Non-linear problems

In general, a non-linear variational problem can be written in the form: find $u \in V$ such that

$$F(u; v) = 0, \quad \forall v \in \hat{V}, \quad (2.53)$$

where $F : V \times \hat{V} \rightarrow \mathbb{R}$ is a semi-linear form, which is linear in the second argument. Equation (2.28) is an example for this kind of problem, where the nonlinearity is described by the Green-Lagrange strain tensor \mathbf{E} . The discretisation of the above problem using finite-dimensional sub-spaces gives: find $u_h \in V_h \subset V$ such that

$$F(u_h; v) = 0, \quad \forall v \in \hat{V}_h \subset \hat{V}. \quad (2.54)$$

Similar to the linear case, let $\{N_i\}_{i=1}^n$ be a basis for the trial space V_h and $\{\hat{N}_i\}_{i=1}^n$ be a basis for the test space \hat{V}_h , the approximation $u_{\text{exact}} \approx u_h = \sum_{i=1}^n N_i u_i$ leads to a non-linear system of equations

$$b(\mathbf{u}) = \mathbf{0}, \quad (2.55)$$

where $b : \mathbb{R}^n \rightarrow \mathbb{R}^n$ and the components of $b(\mathbf{u})$ are:

$$b_i(\mathbf{u}) = F(u_h, \hat{N}_i), \quad i = 1, 2, \dots, n. \quad (2.56)$$

This non-linear system can be solved using iterative methods such as Newton-Raphson method [87].

3. Experimental and numerical methods for cell-substrate interactions

In this chapter, the structure and main components of biological cells are briefly presented. Then, a short review of research on the mechanical interactions between cells and substrates will be given. Both experimental studies and numerical methods are presented.

3.1. Cell structure

The cell is known as the basic structural, functional and biological unit of all recognised living organisms. Cells consist of cytoplasm enclosed within a membrane, which contains many biomolecules such as proteins and nucleic acids [1]. Cells are classified into two types: *eukaryotic* has a nucleus, while *prokaryotic* does not. The space between cells in the tissue is filled by the extracellular matrix, the cell's shape is organised and maintained by the cytoskeleton, and the connection between neighbouring cells or between a cell and the extracellular matrix is provided by cell junctions.

3.1.1. Extracellular matrix

The extracellular matrix (ECM) fills a large part of the tissue volume and is constituted by extracellular macromolecules. The composition of the ECM is different between multicellular structures, but the common functions of the ECM are cell adhesion, cell-to-cell communication and differentiation. In addition to binding the cells together, the ECM also influences their survival, development, shape, polarity and behaviour [1]. Fibrous proteins and glycosaminoglycan (GAG) chains are the two main components

3. Experimental and numerical methods for cell-substrate interactions

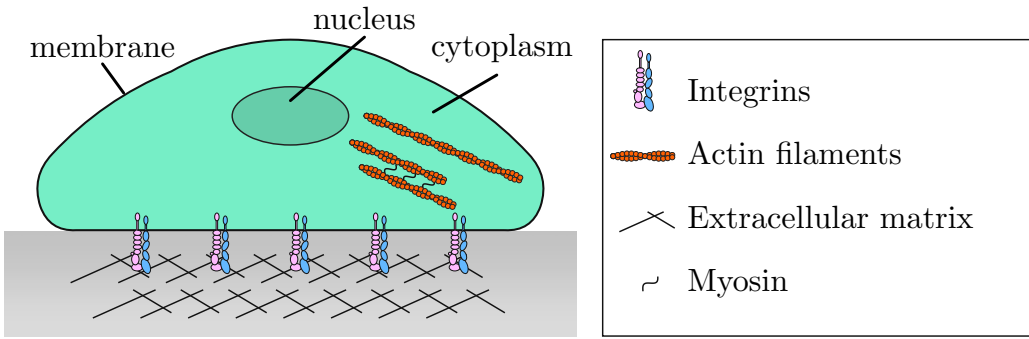


Figure 3.1: 2D visualisation of some fundamental components of a cell and its environment. Figure adapted from [78].

that compose the ECM. GAGs are a heterogeneous group of polysaccharide chains that are usually attached to extracellular matrix proteins to form proteoglycan molecules. Proteoglycans take up a large volume and as they have a net negative charge, they form hydrated gels in the extracellular space. On the surface of cells, proteoglycans also exist and their functionality is to help cells respond to secreted signal proteins [1]. Examples of fibrous proteins are fibrous collagens, fibronectin, tenascin, elastins and laminin [26].

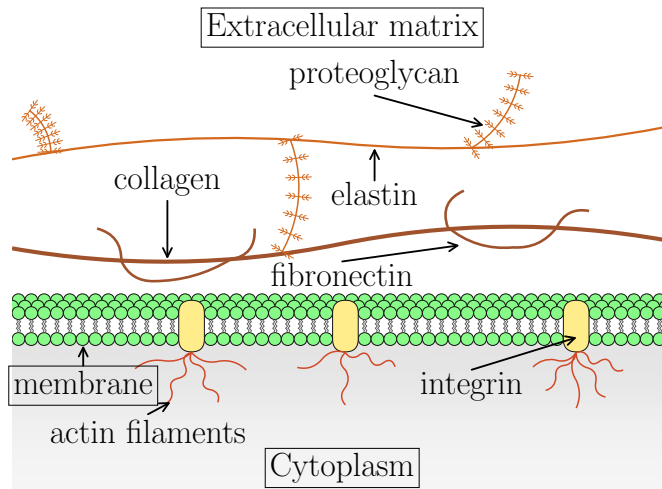


Figure 3.2: Different proteins exist in extracellular matrix including collagen, fibronectin, elastin and proteoglycan. Figure adapted from [23].

3. Experimental and numerical methods for cell-substrate interactions

The elasticity of the ECM is mainly contributed by an extensive cross-linked network of fibres and sheets which is formed by elastin molecules. For different tissue types, the elasticity of the ECM can be various by several orders of magnitude.

3.1.2. Cytoskeleton

All spatial and mechanical functions of cells depend on the so-called cytoskeleton, which is a complex network of interlinked filaments. The cytoskeleton gives the cells the ability to change their shape and move from place to place. It supports the cell membrane and helps the cells to resist deformation and endure strains and external stresses. It also provides machinery for force generation, through which cells sense and respond to the surrounding environment [1].

Microtubules, intermediate filaments and actin filaments are the three common types of filaments that comprise the cytoskeleton of many eucaryotic cells. They are formed by three families of protein molecules. Due to the differences in the magnitudes of the forces between the subunits and their structures, the three types of filaments have different mechanical properties and dynamics (Fig. 3.3). Intermediate filaments are made up of smaller subunits that are themselves elongated and fibrous. They are rope-like structures, easy to bend but hard to break. The subunits that form the microtubules and actin filaments are compact and globular. Microtubules are strong, rigid hollow tubes. Actin filaments are the thinner than the other two types of filaments and are hard to stretch but easy to break [1].

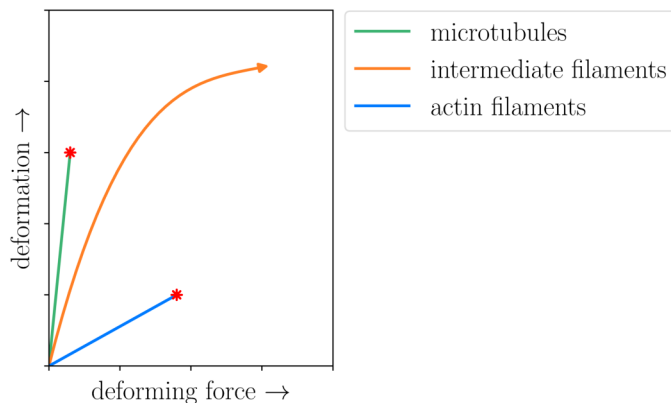


Figure 3.3: Mechanical properties of actin, tubulin and intermediate filament polymers.
Figure adapted from [1].

3. Experimental and numerical methods for cell-substrate interactions

In living cells, the filaments of all three types experience constant remodelling through the assembly and disassembly of their subunits. For microtubules and actin filaments, gaining and losing subunits happen only at their ends, where one end grows faster than the other end. The cell has the ability to expand itself by repeating assembly of large number of small subunits. Due to their very small size, the subunits are able to diffuse rapidly with cytoplasm, while the assembled filaments are not. Hence, cells can undergo rapid structural reorganisations, where filaments are disassembled at one site and reassembled at another site far away (Fig. 3.4).

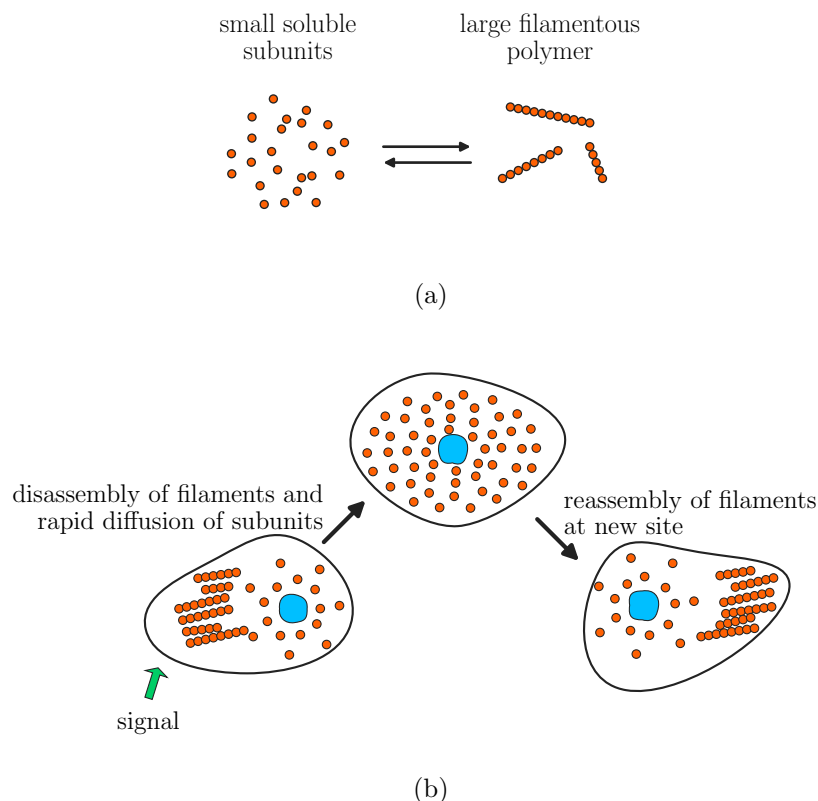


Figure 3.4: (a) Formation of filaments from smaller protein subunits and (b) rapid reorganisation of the cytoskeleton in a cell in response to an external signal. Figure adapted from [1].

3.1.3. Cell Adhesion

The contact between neighbouring cells or between a cell and the extracellular matrix is provided by cell junctions, which consist of multiprotein complexes. Three functional

3. Experimental and numerical methods for cell-substrate interactions

classes of cell junctions are occluding junctions, anchoring junctions and communicating junctions. Tight junctions (occluding junctions) act as barriers regulating the movement of water and solutes between epithelial layers, communicating (GAP) junctions enable communication between neighbouring cells, while anchoring junctions link cytoskeletal proteins in one cell to those in neighbouring cells as well as to proteins in the extracellular matrix. Anchoring junctions are usually classified into four main types, including adherens junctions, desmosomes, focal adhesions and hemidesmosomes. The first two types connect cells together and are formed by cadherins, whereas the last two types connect cells to extracellular matrix and are formed by integrins [1].

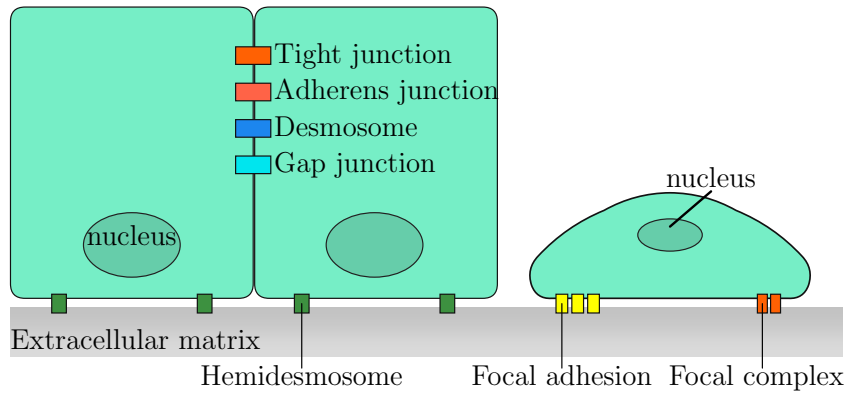


Figure 3.5: Cell-cell and cell-matrix adhesion apparatuses. Adherens junction, tight junction, desmosome and gap junction support cell-cell adhesion, while adhesion between cell and matrix is promoted by hemidesmosome, focal complex and focal adhesion. Figure adapted from [62].

Focal adhesions are junctions that mediate cell-matrix adhesion, force transmission, cytoskeletal regulation and signalling [43]. At the focal adhesions, extracellular matrix molecules, such as laminin or fibronectin, interact with cell-surface matrix receptors called integrins, which are linked to the actin cytoskeleton [1].

3.2. Experimental studies

The responses of cells to external stimuli have been measured using several force application techniques.

3. Experimental and numerical methods for cell-substrate interactions

Micro-pipette aspiration was introduced by Mitchison and Swann [61] to measure the mechanical properties of sea-urchin eggs. In this method, the amount of cell material which is pulled into a glass pipette under an applied pressure is examined (Fig. 3.6a). When combining with basic continuum models, this technique is able to measure the elastic and viscous properties of cells of different stiffness magnitudes [40]. It has been utilised to measure the Young's modulus and viscoelastic properties of cells of various types such as red blood cells, chondrocytes and endothelial cells [39, 73, 79, 93, 94].

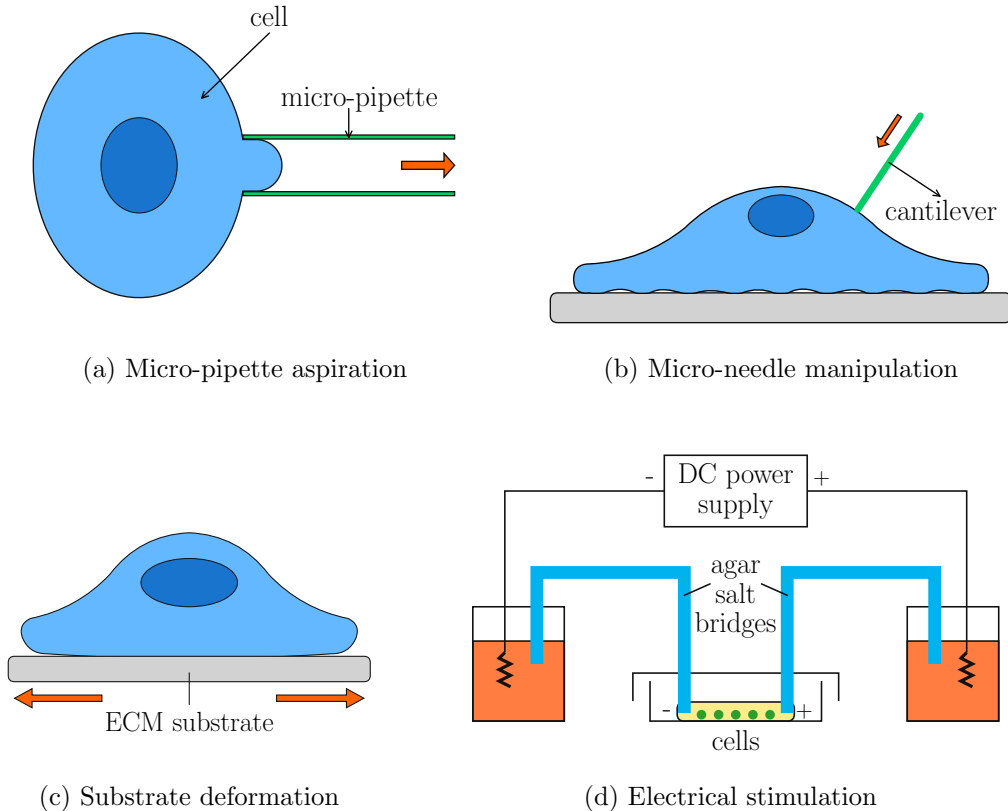


Figure 3.6: Some force application techniques. (a) The micro-pipette aspiration setup where a cell of circular shape is being aspirated into a pipette. (b) In micro-needle manipulation technique, a thin and flexible micro-needle is used to push and penetrate into cells. (c) Strain is applied to the cell by stretching the underlying substrate. (d) A chamber for electrical stimulation is used to apply electric field to the cells. Figures adapted from [56].

Micro-needle manipulation is a technique in which a thin and flexible glass micro-needle is used to push and penetrate into organelles of living cells or to indent into the cell membrane to measure the cellular elasticity [72] (Fig. 3.6b). This technique has

3. Experimental and numerical methods for cell-substrate interactions

been refined and applied to determine the mechanical material properties of different cell types [46, 73, 83] and to study structural connectivity in the cytoplasm and nucleus [54].

In the substrate deformation technique, cells are cultured on top of an elastic membrane or gel coated with extracellular matrix protein and a strain can be applied by stretching the underlying substrate using an indenter or vacuum pressure [73] (Fig. 3.6c). By applying various uniaxial loads, it is possible to assess the effect of substrate deformation on the morphology, genetic regulation, metabolic activity, injury and phenotype of cells [105]. Jones *et al.* [41] applied homogeneous strains to osteoblast-like cells and skin fibroblasts and observed that only periostal osteoblasts are sensitive to strains within the physiological range, while higher, unphysiological strains were needed to see the responses of osteoblasts derived from the haversian system and skin fibroblasts. Wang *et al.* [108] combined this technique with mathematical model to study the orientation response of human melanocytes under cyclic substrate strain. The response of primary human endothelial cells and smooth muscle cells to mechanical forces was investigated by Greiner *et al.* [29]. The external mechanical stimulation was implemented by applying stretches of different frequencies from 0.01 – 1.0Hz to elastic membranes on which the cells were cultured. A remarkable finding presented in [29] was the frequency dependence of the area of the focal adhesion and the reorganisation of the actin cytoskeleton as well as the focal adhesions system. Moreover, there exists a threshold frequency below which the responses of endothelial cells are not detectable.

One of electrical techniques is to apply electrochemical gradients or stimulation to a population of cells using metal electrodes or salt bridges (Fig. 3.6d). Using this technique, Gou *et al.* [33] found that with an electric field of 50–100mV/mm, human dermal fibroblasts migrated directionally toward the anode but the migration was slow and could only be detected after more than one hour. A stronger field 400mV/mm was required in order for the migration to happen within one hour. Under physiological electric fields, corneal epithelial sheets and bovine vascular endothelial cells migrated toward the cathode and their migration was also voltage dependent [51, 113]. Here, electric fields whose strengths lie in range of 1 – 200mV/mm are considered physiological, as suggested by Nuccitelli [68]. In addition to the cell migration, this technique has also been used to study the effect of electric field on cell contraction or cell orientation and organisation. Influenced by physiological electric fields, embryonic fibroblasts oriented their long axes in the direction perpendicular to the electric field [22]. Under a voltage gradient of 400mV/mm and greater, the cells elongated in the perpendicular

3. Experimental and numerical methods for cell-substrate interactions

direction [22, 36]. Using a steady voltage gradient of 1V/mm, Curtze *et al.* [14] found that osteoblast-like cells responded in two phases: they first retracted then aligned and elongated perpendicular to the electric field direction.

To quantify the forces generated by cells during their migration, contraction and development, several force-sensing techniques have been developed and applied.

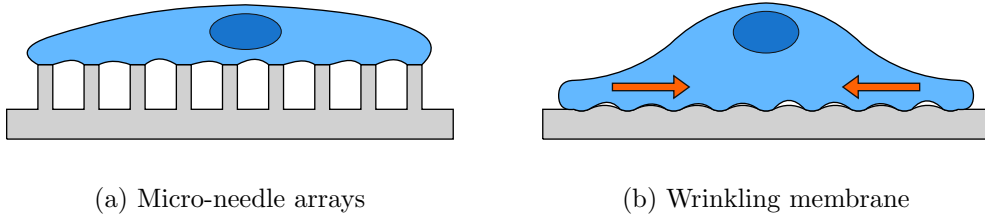


Figure 3.7: Some force sensing techniques. (a) Micro-needle arrays can be used to estimate local cell forces at different regions. (b) In the wrinkling membrane technique, force produced by the cells is estimated based on the number of wrinkles and the lengths of the wrinkles formed on the substrate [35]. Figures adapted from [89].

Traction Force Microscopy (TFM) is an experimental method in which cellular cultures are seeded on or within an optically transparent 3D ECM embedded with fluorescent microspheres. The traction forces generated by cells are estimated based on the displacement field computed from the images. Wang *et al.* [109] applied TFM to test the prediction that the stiffness of human airway smooth muscle cells increases proportionally with the level of the tensile stress borne by filamentous structures. Using TFM to measure the traction before and after treatment with the contractile agonist histamine, the contractility of smooth muscle cells was found to be controlled by cell spreading [91]. By analysing the dynamic characteristics of mechanical forces exerted by migrating fibroblasts, Munevar *et al.* [66] revealed several interesting results, for example, the changes in the pattern of traction forces often preceded changes in the direction of migration. Soiné *et al.* [85] applied a new type of TFM, where a biophysical model and additional images for cytoskeleton and adhesion are used, and found that in U2OS-cells, ventral stress fibers experienced a higher tension than dorsal stress fibers or transverse arcs.

Wrinkling membranes is a technique developed by Harris *et al.* [35] to measure the

3. Experimental and numerical methods for cell-substrate interactions

traction forces generated by cells (Fig. 3.7b). In this technique, cells are seeded on a thin and flexible membrane of silicon rubber and the force produced by the cells is estimated based on the number of wrinkles and the lengths of the wrinkles formed on the substrate. Utilising this method, a great difference in the strength of cellular traction was found between cell types. Moreover, the most mobile and invasive cells were found to deliver the weakest traction [34]. Burton and Taylor [11] extended this method by using substrata of new silicone polymer whose compliance can be adjusted precisely. They were able to recognise forces of nano-newtons to micro-newtons in dividing cells.

The approach using micropost arrays to measure mechanical interactions between cells and substrate was introduced by Tan *et al.* [89]. In this method, the compliance of the posts can be adjusted by changing their geometrical parameters such as the height or cross-sectional area. The cells are attached to the posts and when they move, the posts are deflected differently at different regions. The traction force by the cell at each post is then approximated by:

$$F = \left(\frac{3EI}{L^3} \right) \delta, \quad (3.1)$$

where E , I , L and δ are the Young's modulus, moment of inertia, height and the deflection of the post, respectively [89]. Using this method, Tan *et al.* [89] could quantify the traction forces for spread and unspread bovine pulmonary artery smooth muscle cells and found a positive correlation between the area of focal adhesions and the force generated at those adhesions. Combining this technique with a multiple-particle tracking method, du Roure *et al.* [21] could quantify the dynamic traction forces exerted by Madin-Darby canine kidney (MDCK) epithelial cells on a substrate. They found that the highest intensity of the forces is localised at the edge of the cell and the magnitude of the stresses at the edge of a cell monolayer is higher than that of a single cell. Schoen *et al.* [81] suggested a contribution of substrate warping to have a better accuracy when computing forces.

Since it was introduced, this method has been widely applied and extended in different manners. Sniadecki *et al.* [84] built a force application system from an array of magnetic and non-magnetic posts and used a magnetic field to apply external force to individual adhesions of cells. They revealed interesting results, such as an increase in local focal adhesion size at the regions where step forces were applied. Matschegowski *et al.* [55] used regular arrays of titanium cubic pillars and investigated the dependency on substrate characteristics of the architecture and function of human MG-63 osteoblasts. Based on this approach, the research of Mörke *et al.* [63] suggested that in order for osteoblasts

to maintain their function, implant biomaterials for bone replacement should provide enough cell-material contact area and enough surface sides or area to provide a good mechanical fixation of the implant in the native bone.

3.3. Mathematical modelling

Besides experimental studies, computational modelling has been a powerful approach to the understanding of the mechanisms for the interactions between cells and their surrounding environments, as it could give us an interpretation of the experimental outcomes. Several modelling approaches can be used in cell biology, including agent-based simulations, which are based on explicit tracking of all molecules in the cell, and partial differential equation (PDE) modelling, which involve solving numerically a set of PDEs on a continuous domain [64]. In cell mechanics, the latter is more widely used, where the models are usually based on continuum mechanics and are solved using the finite element method [73]. The models have different levels of complexity and hence can capture the bio-mechanical behaviour of cells to different extents. Passive models, in which cells are assumed to react passively to external stimuli, have the simplicity but a limited ability to reflect cell behaviour. Constructed with a higher complication, active models integrate active reactions and can simulate the remodelling of cells under physical stimuli exposure [73].

Liquid drop models were developed to explain the rheological response of leukocytes during micro-pipette aspiration. Their formulations were derived based on the assumption that cells are comprised of one or more layers of cytoplasmic fluids, surrounded by prestressed cortical shells [52, 73]. Tran-Son-Tay *et al.* [92] used a Newtonian liquid drop model, in which the cell's interior is assumed to be a homogeneous viscous Newtonian fluid (Fig. 3.8a), to analyse the recovery process of a human neutrophil in an experiment with micro-pipette. This model delivered a good agreement with the experimental data, but was not able to capture the case when the cell was held for only a very short time in the pipette [38, 92]. This limitation was overcome by using a compound Newtonian liquid drop model, in which three layers were used for the cell: an outer membrane surface, a shell layer, and a core [42] (Fig. 3.8b). In order to capture the rapid entry of cells into a micro-pipette at the starting point of an aspiration test, a Maxwell liquid drop model can be used. This model is an extension of the Newtonian liquid drop model, where the cytoplasm is assumed to act like a Maxwell element [73]. Using this model,

3. Experimental and numerical methods for cell-substrate interactions

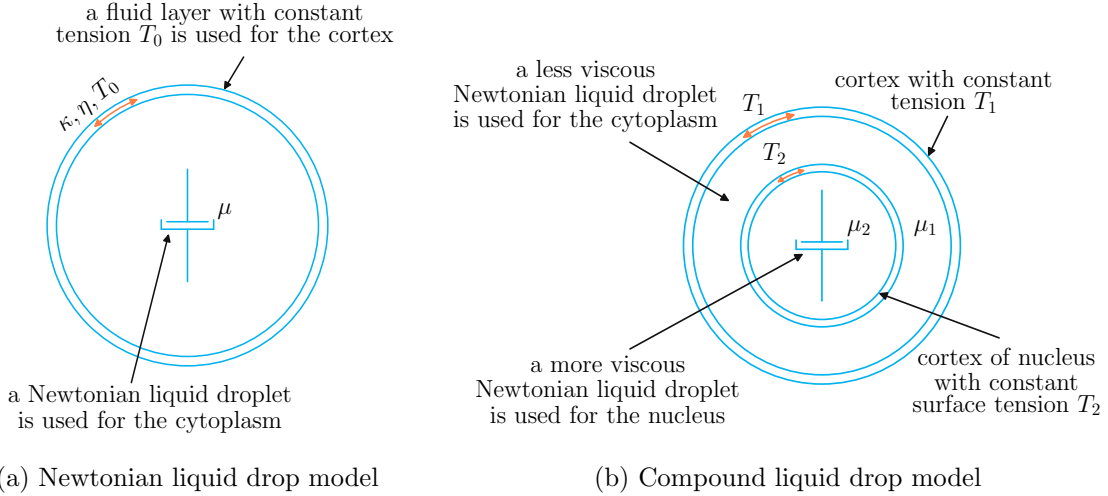


Figure 3.8: (a) A Newtonian liquid drop model considers the cell as a Newtonian liquid droplet contained in a cortical layer with a constant tension T_0 . The shear viscosity of the cytoplasm is μ , while the coefficients of viscosity for surface area dilation and shear of the membrane are κ and η , respectively. (b) Three layers of a compound liquid drop model: the membrane, the cytoplasm (with viscosity μ_1) and the nucleus (with viscosity μ_2 ; $\mu_2 > \mu_1$). Figures adapted from [52].

Dong *et al.* [19] could predict the results of experiments with micro-pipette for both cases: short-time small deformation and slow recovery after large deformation.

In solid models, the distinct cortical layer is not considered and the whole cell is often assumed as homogeneous. Different material models can be used, but two of them are widely accepted: elastic solid and visco-elastic solid [52]. Linear elastic solid models consider the cell as homogeneous, elastic material conducted by Hook's law. The relationship between the deviatoric stress τ_{ij} and the engineering strain γ_{ij} in linear elastic solid models is given by:

$$\tau_{ij} = G\gamma_{ij}, \quad (3.2)$$

where G is the shear modulus, which is related to the Young's modulus E and the Poisson's ratio ν by $E = 2(1 + \nu)G$. The models are applicable for the estimation of cell material properties, but they are generally inappropriate to describe the mechanics of the cells, due to the oversimplification on the material law [73]. In micropipette experiments where the pipette radius is much smaller than the local radius of the cell surface, Theret *et al.* [90] considered the cell as an incompressible elastic half-space.

3. Experimental and numerical methods for cell-substrate interactions

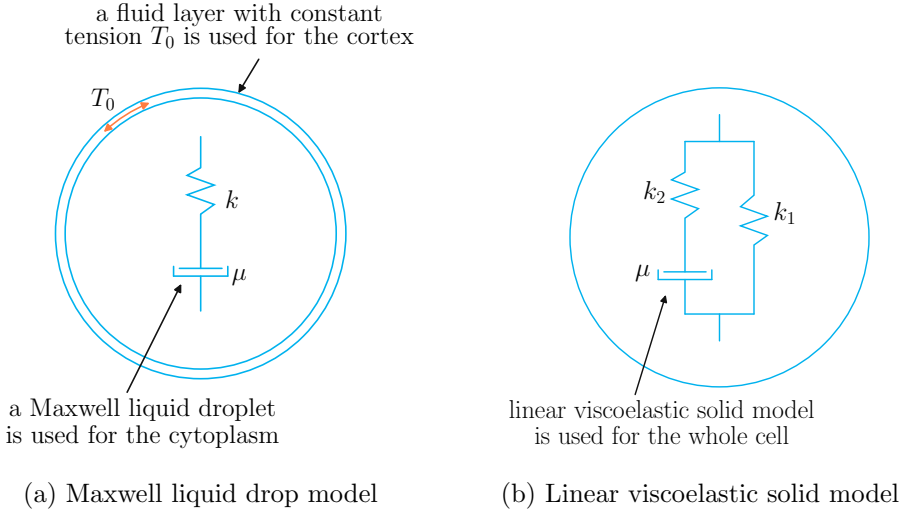


Figure 3.9: (a) In Maxwell liquid drop model, the cell is modelled as a Maxwell liquid droplet with a viscous constant μ and an elastic constant k bounded by a constant tension T_0 . (b) The whole cell is modelled as a homogeneous viscoelastic linear solid with a viscous constant μ and two elastic constants k_1 and k_2 . Figures adapted from [52].

Doing this, the formula for an effective Young's modulus of the cells could be derived and applied for the determination of the mechanical properties of bovine endothelial cells [52, 90]. Using a similar approach by modelling the cell as a linear elastic half-space in the cytoindenter experiments, Shin and Athanasiou [83] could estimate the permeability and the Poisson's ratio of MG63 osteoblast-like cells. For magnetic twisting cytometry experiment, Mijailovich *et al.* [59] modelled the cell as a three-dimensional slab, whose material is linear elastic and incompressible, and could relate the elastic modulus to the cell height and the degree of bead embedding.

In a linear visco-elastic solid model, the dependency of the stress in the cell on the loading history is considered. The material law describes the relationship between the deviatoric stress τ_{ij} and the engineering strain γ_{ij} and their rates of change as [80]:

$$\tau_{ij} + \frac{\mu}{k_2} \dot{\tau}_{ij} = k_1 \gamma_{ij} + \mu \left(1 + \frac{k_1}{k_2} \right) \dot{\gamma}_{ij} \quad (3.3)$$

where μ is the viscosity and k_1, k_2 are the spring constants (Fig. 3.9b). Guilak *et al.* [32] applied this theoretical model for the measurement of the osmotic and viscoelastic properties of articular chondrocytes. The results of DiMilla *et al.* [18] employing a viscoelastic-solid model could predict the influence of cell speed during migration on the

3. Experimental and numerical methods for cell-substrate interactions

cellular contractile force or the densities of ligand and receptor. Enhancing a viscoelastic model by a cable network of stress fibres modelling the actin cytoskeleton, Milner *et al.* [60] investigated the stress and strain in the cytoplasm and the nucleus of osteoblastic cells under the application of high-frequency mechanical loading.

The active responses of the cells to the external stimuli have been addressed in the active models with different levels of complexity. Zemel *et al.* [112] used actin-myosin dipoles to represent the active remodelling of cytoskeleton in their dipole polymerisation model. Under applied elastic strain, these dipoles respond by changing their orientation. For a population of cells with ρ being the number of cells per unit volume, the average value $\rho\langle p_{ij} \rangle$ can be used to measure the cell polarisation. Here, $p_{ij} = \sum f_i l_j$ is the force dipole tensor, where \mathbf{f} is the force vector at each adhesion contact between the cell and the matrix, \mathbf{l} is the radius vector to the contact, and the sum is taken over all contacts. In the direction of the principal strain, the polarisation of the cells is given in [112] as:

$$P_{ij} = \rho(\langle p_{ij} \rangle - \langle p_{ij} \rangle_0) \quad (3.4)$$

which measures the increase in the average dipole tensor compared to the case when the external forces are absent. This polarisation tensor P_{ij} and the applied stress σ_{ij}^a together produce the total excess stress in the system $\sigma_{ij} = \sigma_{ij}^a + P_{ij}$. The applied stress is usually expressed through the excess strain u_{ij} and the elastic moduli \mathbf{C} as $\sigma_{ij}^a = \epsilon \mathbf{C} u_{ij}$, where ϵ is the elastic permittivity tensor. Based on these definitions, an interaction energy W between the cellular dipole p_{ij} and the local strain u_{ij}^{loc} in the cell vicinity can be established and the optimal orientation of cells under the application of an elastic strain field can be predicted by solving an energy minimisation problem [112].

The model developed by Kaunas *et al.* [44] addresses the active response of the cell to mechanical stretching by describing the reorganisation of actin stress fibres based on constrained mixture theory. In the model, the assembly and disassembly of the fibres are assumed to obey a first-order kinetics relation:

$$\frac{d\Phi^i}{dt} = -k^i \Phi^i \quad (3.5)$$

where Φ^i expresses the mass fraction of the stress fibre i and k^i is the disassembly rate constant. Inspired by experimental observations, the constant k^i is expressed as a function of the fibre stretch α^i as:

$$k^i = k_0 \left[1 + k_1 \left(\frac{\alpha^i - \alpha_0}{\alpha_0} \right)^2 \right] = k_0[1 + k_1(\Delta\alpha^i)] \quad (3.6)$$

3. Experimental and numerical methods for cell-substrate interactions

where k_0 and k_1 are two constants and α_0 is the homeostatic level of stretch [44]. Employing this model, the results for the changes in the distributions of stress fibre orientations are in good agreement with experimental data [44].

In the constrained mixture model by Vernerey and Farsad [107], the development of the stress fibre network within the cell is described through the coupling between mechanics and chemistry. Using a multiphasic approach (with fluid, solid and solute mixture phases), the contraction of the cell is mainly governed by four constituents: solid cytoskeleton (s), fluid cytosol (f), stress fibre (p) and actin monomers (m). At every

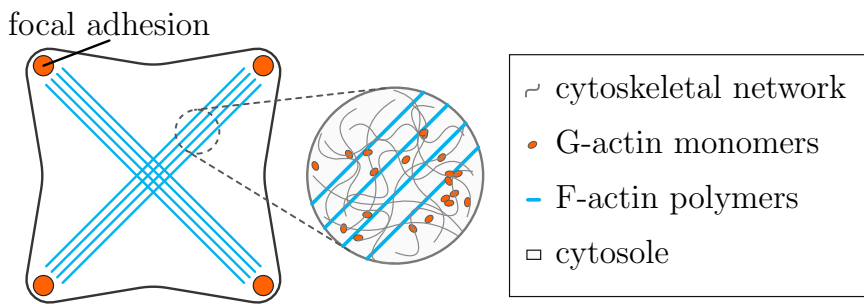


Figure 3.10: Illustration of a cell based on experiment of Parker *et al.* [70]. Every material point in the cytoplasm is considered as a mixture of four constituents including the cytoskeletal network, G-actin monomers, contractile stress fibre and cytosol. Figures adapted from [107].

material point, each constituent is associated with a volume fraction ϕ^α ($\alpha = s, f, m, p$) which is the ratio between the unit volume of the constituent and the unit volume of the mixture. With the assumption that the cell is made up by these four constituents, the relation $\phi^s + \phi^f + \phi^m + \phi^p = 1$ is hold. The main features of the model include:

- Bio-mechanical contraction of stress fibres is represented by length-tension and velocity-tension relationships of the fibre.
- The formation of the stress fibres is resulted by the mass exchange between them and the available actin monomers in the cytoplasm, where the rate of the formation and the dissociation is assumed to be dependent on the tension in the fibre. Moreover, the transport of fluid and monomers within the cell is assumed to obey the laws of diffusion-convection.
- In addition to passive elasticity, the contribution of the active contractile stress, which is based on the anisotropic distribution of stress fibres, is addressed.

3. Experimental and numerical methods for cell-substrate interactions

For a stress fibre in the direction associated with an angle θ between the fibre and the base vector \mathbf{e}_1 , the polymerisation rate is given as:

$$\Gamma_\theta^p = \left(k^f \frac{\phi^m}{\phi^f} - k^d \phi_\theta^p \right) \quad (3.7)$$

where k^f and k^d are the constants for the formation and the dissociation of the F-actin. Here, ϕ_θ^p is a distribution function representing the variation in stress fibre density with direction θ . A possible representation for this distribution is the π -periodic von Mises distribution function proposed by Gasser *et al.* [27]:

$$\phi_\theta^p = \phi^p \left[\frac{\exp(b \cos(2\theta - \theta_0))}{I_0(b)} \right] \quad (3.8)$$

where

$$I_0(b) = \frac{1}{\pi} \int_0^\pi \exp(b \cos \theta) d\theta \quad (3.9)$$

is the zero-order Bessel's function of the first kind, b represents the level of anisotropy of the stress fibres and θ_0 is corresponding to the direction which has the largest fibre density. The plot of the von Mises distributions for some different values of b is shown in Fig. 3.11.

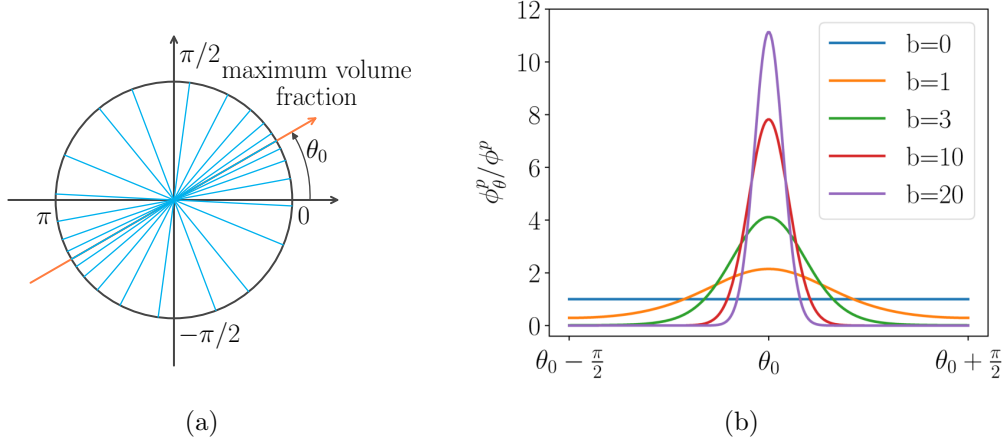


Figure 3.11: (a) An example of anisotropic distribution of stress fibres at a point in the cell and (b) plot of von Mises distribution for different levels of anisotropy. Figure adapted from [107].

The uni-axial contractile stress T_p in a fibre is assumed to be dependent on both the strain ε and the strain rate $\dot{\varepsilon}$ of the fibre and has the form as:

$$\frac{T^p}{\bar{T}} = T^*(\varepsilon, \dot{\varepsilon}) \quad (3.10)$$

3. Experimental and numerical methods for cell-substrate interactions

where \bar{T} is the isometric contraction of the fibre when it is not deformed ($\varepsilon = 0$) and at rest ($\dot{\varepsilon} = 0$). The function $T^*(\varepsilon, \dot{\varepsilon})$ was constructed based on the assumption that the strain and the strain rate affect the fibre tension independently. For this, $T^*(\varepsilon, \dot{\varepsilon})$ can be expressed as a product of two functions $f(\varepsilon)$ and $g(\dot{\varepsilon})$ representing the length-tension relation and velocity-tension relation, respectively. These two functions should capture several characteristics of the stress fibres in the experiments and are suggested to have the forms [107]:

$$f(\varepsilon) = \begin{cases} \exp \left[-\left(\frac{\varepsilon}{\varepsilon_0} \right)^2 \right] & \varepsilon < 0 \\ \exp \left[-\left(\frac{\varepsilon}{\varepsilon_0} \right)^2 \right] + \left(\frac{\varepsilon}{\varepsilon_1} \right)^2 & \varepsilon \geq 0 \end{cases}, \quad (3.11)$$

$$g(\dot{\varepsilon}) = 1 + \frac{\dot{\varepsilon}/\dot{\varepsilon}_0}{\sqrt{(\dot{\varepsilon}/\dot{\varepsilon}_0)^2 + 1}} \quad (3.12)$$

where the parameter ε_0 tells how fast the contraction decreases when the strain deviates from zero and the parameter ε_1 represents the passive strain hardening of the fibre. The plots for $f(\varepsilon)$ and $g(\dot{\varepsilon})$ are shown in Fig. 3.12.

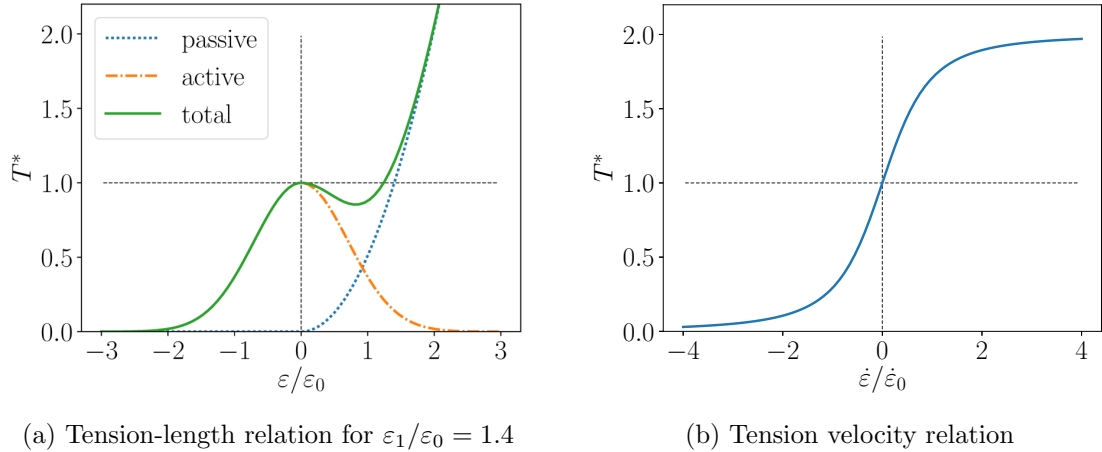


Figure 3.12: Plots for tension-length and tension-velocity relations. Active and passive responses of a stress fibre are addressed in the length-tension relationship. Figures adapted from [107].

The model has been successfully applied to predict the influence of the stiffness of the mechanical environment on the contraction of the cell as well as the development and

3. Experimental and numerical methods for cell-substrate interactions

orientation of a network of stress fibres in contracting fibroblasts [107]. The predictions of those results for the case when the cells are subjected to constant or cyclic stretch and are on substrates of different stiffnesses can also be obtained [24].

Addressing a similar level of detail compared to the model of Vernerey and Farsad [107], the bio-chemo-mechanical model by Deshpande *et al.* [15] is supplied with a bio-mechanical process and is shown to be efficient through numerous of its applications. Due to its advantages, this model is selected as a foundation for our model. The detail about the formulation as well as the applications of the model will be presented in the next chapter.

4. An efficient theoretical framework for cell contractility and adhesion

This chapter contains a part of our research article [99].

The bio-chemo-mechanical model proposed by Deshpande *et al.* [15] is one of the most successful active computational models for the mechanical responses of cells. The development of the model was inspired by the experiments of Tan *et al.* [89], where smooth muscle cells were laid on beds of micro-needles and the force on each needle was measured. By including the bio-chemical processes and describing the formation and dissociation of cytoskeleton based on experimental observations, the model can efficiently interpret a great number of results found from existing experiments on cell contraction. For example, it can explain the strong dependence of the forces generated by the cells on the substrate compliance and the influence of boundary conditions on the orientation and formation of stress fibres. With a description for the contact between the cell and the substrate, McGarry *et al.* [57] could apply the model for the simulations of smooth muscle cells and other cell lines on arrays of micro-posts. When combined with a bio-mechanical model for cell adhesion, this model could predict the distribution of high and low affinity integrins in addition to actin filaments [17, 71]. The three dimensional description of the model could give the actin distribution at the location near the cell nucleus as well as at the contact regions in the force indentation experiments [20, 74, 75].

In this chapter, the relevant concepts and the governing equations of the bio-chemo-mechanical model for cell contractility and the bio-mechanical model for cell focal adhesion are presented. Then, our approach for an efficient software implementation of the model is described. For our purpose of extending the model and applying it to our research, such a good implementation is necessary. Finally, several applications of the model are shown by comparing the results from our implementation to those in the literature.

4.1. The bio-chemo-mechanical model for cell contractility

4.1.1. Background and assumptions

The bio-chemo-mechanical model of Deshpande *et al.* [15] was developed based on their observations that the assembling of stress fibres is due to some signalling cascade in the cell [1, 10] and the dissociation is caused by decrement of tension in the cell cytoplasm [10, 25]. According to Deshpande *et al.* [15], the contractility of cells is driven by a mechanical term which is called active stress and is the result of tensions in stress fibres in all directions caused by the activation in the cell. This active stress and the level of activation are dependent on the rate of cell deformation and the remodelling of the actin cytoskeleton which is influenced by the concentration of signal.

For the validity of the model, three fundamental assumptions were made [15]. Firstly, the actin and myosin in the cell are assumed to be sufficient so that the activation of the stress fibres in each direction is not limited by their availability. Secondly, it is assumed that a fine scale network of fibres exists on a length scale much smaller than the dimensions of the cell. Finally, the stress fibres are assumed to be able to form in any direction with equal probability.

4.1.2. The equations

The bio-chemo-mechanical model [15] is defined for a single stress fibre and is described by three equations. First, as bio-chemical processes are complex and not well understood, a simple exponential function is used to represent the concentration:

$$C = \exp(-t/\theta) \in [0, 1], \quad (4.1)$$

where θ is the decay constant of a chemical compound, t is the time measured from the instant of the most recent signal. The plot of the function $C(t)$ for two sample values of θ is shown in Fig. 4.1a. Second, to describe the remodelling of the actin cytoskeleton, a non-dimensional term called activation level $\eta \in [0, 1]$ is introduced and the equation for evolution of η is established based on experimental observations as:

$$\dot{\eta} = [1 - \eta] \frac{C \bar{k}_f}{\theta} - \left[1 - \frac{\sigma_f}{\sigma_0} \right] \eta \frac{\bar{k}_b}{\theta}, \quad (4.2)$$

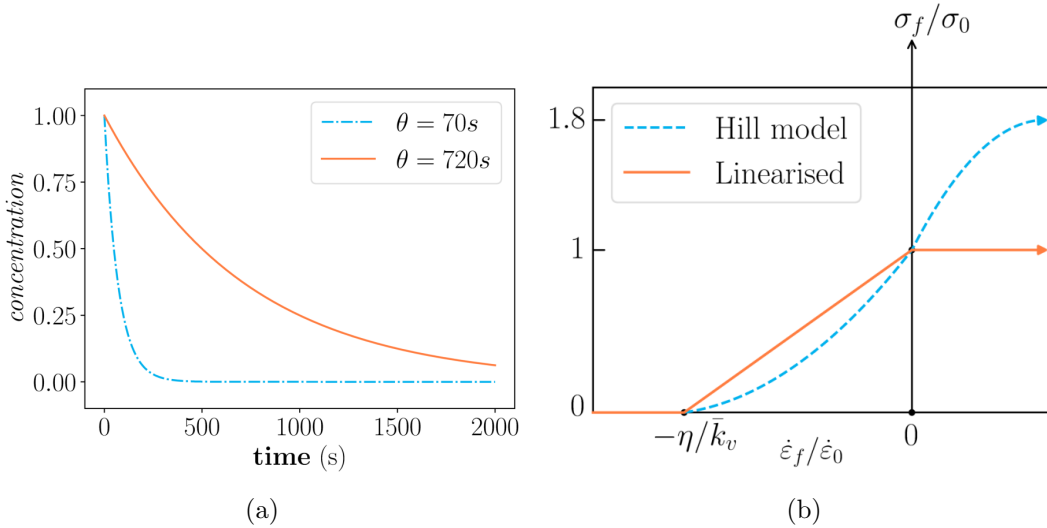


Figure 4.1: (a) The plot of the concentration for two different values of θ . The value θ determines the amount of time until the concentration is close to zero. (b) Hill-like equation for stress-strain rate relationship. Figure adapted from [16].

where the term $[1 - \eta] \frac{C \bar{k}_f}{\theta}$ expresses the rate of stress-fibre-formation dependent on the signal C , controlled by the constant \bar{k}_f . Similarly, the second term on the right hand side is a non-negative number that expresses the rate of stress fibre dissociation, which depends on the current tension relative to the isometric tension σ_0 and is controlled by the constant \bar{k}_b . Here, σ_0 is the maximum tension allowed in the stress fibre corresponding to the activation level η and is given as $\sigma_0 = \eta \sigma_{\max}$, where σ_{\max} is the maximum tension at $\eta = 1$, that is, when the stress fibre is fully activated. Finally, a linearised Hill equation [37] is used to describe the relationship between tension σ_f and the lengthening / shortening strain rate $\dot{\varepsilon}_f$ as:

$$\frac{\sigma_f}{\sigma_0} = \begin{cases} 0 & \frac{\dot{\varepsilon}_f}{\dot{\varepsilon}_0} < -\frac{\eta}{\bar{k}_v} \\ 1 + \frac{\bar{k}_v}{\eta} \left(\frac{\dot{\varepsilon}_f}{\dot{\varepsilon}_0} \right) & -\frac{\eta}{\bar{k}_v} \leq \frac{\dot{\varepsilon}_f}{\dot{\varepsilon}_0} \leq 0 \\ 1 & \frac{\dot{\varepsilon}_f}{\dot{\varepsilon}_0} > 0 \end{cases} \quad (4.3)$$

where \bar{k}_v is the fractional reduction in fibre stress upon increasing the shortening rate relative to $\dot{\varepsilon}_0$. The plot for this stress-strain rate relationship is shown in Fig. 4.1b.

4.1.3. Incorporating the bio-chemo-mechanical model into the framework of continuum mechanics

To apply the bio-chemo-mechanical model for a cell comprising a network of stress fibres, a representative volume element (RVE) is defined and the constitutive relation is established [16]. Due to generated tensions of stress fibres, the total stress in the cell should include the active stress, in addition to the passive non-contractile stress. The appearance of the active stress in the continuum mechanics frameworks is described by introducing an additional stress term to the Eq. (2.12) so that the equilibrium equation becomes:

$$\nabla \cdot (\mathbf{F} \mathbf{S}^{\text{total}}) + \rho_0 \mathbf{b} = \mathbf{0} \quad \forall \mathbf{X} \in \Omega_0 \quad (4.4)$$

where

$$\mathbf{S}^{\text{total}} = \mathbf{S}^{\text{active}} + \mathbf{S}^{\text{passive}} \quad (4.5)$$

and $\mathbf{S}^{\text{active}}$, $\mathbf{S}^{\text{passive}}$ denote the active and passive stress tensors, respectively. Usually, an elastic material model is used for the cell and $\mathbf{S}^{\text{passive}}$ becomes the second Piola-Kirchhoff stress tensor, which is related to the Green-Lagrange strain tensor \mathbf{E} by the constitutive equation $\mathbf{S}^{\text{passive}} = \mathbf{C} : \mathbf{E}$ with \mathbf{C} being the material stiffness tensor.

As stress fibres can form in any direction in the RVE, this active stress tensor is obtained as an integral with a coordinate transformation from the fibre direction to the Cartesian coordinate. In finite element implementation, only approximated values are obtained by choosing a set of N_d (relatively large) directions for stress fibres, each direction is represented by a unit vector \mathbf{m} . The equations (4.2), (4.3) are then solved for these N_d directions and active stresses are computed as numerical integrals.

2D modelling When it is assumed that the cell thickness is small compared to the other two dimensions and that only in-plane contractility occurs, then a 2D finite element analysis can be applied. A set of N_d directions is obtained by spacing equally N_d angles $\phi \in [-\pi/2, \pi/2]$, where ϕ is the angle between the stress fibre and the \mathbf{e}_1 axis, as shown in Figure 4.2a. The unit vector $\mathbf{m}(\phi)$ corresponding to the angle ϕ is then written as $\mathbf{m}(\phi) = \cos(\phi)\mathbf{e}_1 + \sin(\phi)\mathbf{e}_2$. Generally, the activation at each point in the cell is different in each direction (Fig. 4.2b).

The strain rate $\dot{\varepsilon}_f$ of the stress fibre associated with direction ϕ is calculated from the material strain rate \dot{E}_{ij} as

$$\dot{\varepsilon}_f \equiv \dot{E}_{11} \cos^2 \phi + \dot{E}_{22} \sin^2 \phi + \dot{E}_{12} \sin 2\phi \quad (4.6)$$

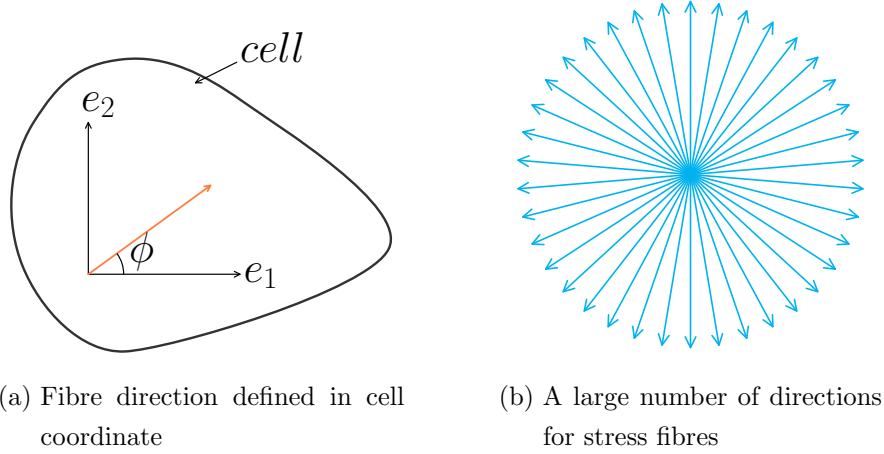


Figure 4.2: In 2D implementation, a set of fibre directions needs to be defined and the equations are solved in these directions. A possible sampling is the division of a circle into many equal angles.

and the average active stress in Cartesian coordinate generated by the fibres is obtained as

$$S_{ij} = \frac{1}{\pi} \int_{-\pi/2}^{\pi/2} \sigma_f m_i(\phi) m_j(\phi) d\phi \quad i, j = 1, 2 \quad (4.7)$$

where σ_f is the tension in the stress fibre. The value of this stress is calculated using numerical integration. The active stress tensor is written as

$$\mathbf{S}^{\text{active}} = \frac{1}{\pi} \int_{-\pi/2}^{\pi/2} \begin{pmatrix} \sigma_f(\phi) \cos^2 \phi & \frac{\sigma_f(\phi)}{2} \sin 2\phi \\ \frac{\sigma_f(\phi)}{2} \sin 2\phi & \sigma_f(\phi) \sin^2 \phi \end{pmatrix} d\phi \quad (4.8)$$

3D modelling In the general case where stress fibres can form in any direction in the space, a 3D analysis should be performed. The orientations of stress fibres are determined by distributing N_d unit vectors in 3D space such that the minimum distance from a vector to its neighbours is maximised [3, 74]. Each unit vector is defined by a pair of angles ω and ϕ (Figure 4.3a) as $\mathbf{m}(\omega, \phi) = \sin(\omega) \cos(\phi) \mathbf{e}_1 + \sin(\omega) \sin(\phi) \mathbf{e}_2 + \cos(\omega) \mathbf{e}_3$. The activation is generally different in each direction (Fig. 4.3b).

The strain rate $\dot{\epsilon}_f$ in the fibre associated with $\mathbf{m}(\omega, \phi)$ is related to the strain rate in

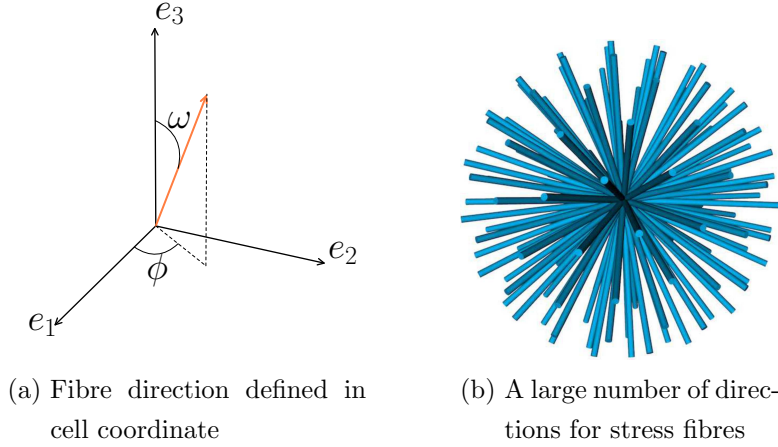


Figure 4.3: In 3D implementation, a possible sampling for fibre orientations is obtained by distributing a great number of unit vectors at the origin so that the minimum distance from each vector to its neighbours is maximised.

the RVE by:

$$\begin{aligned}\dot{\varepsilon}_f = \dot{E}_{ij} m_i m_j &= \dot{E}_{11} \sin^2 \omega \cos^2 \phi + \dot{E}_{22} \sin^2 \omega \sin^2 \phi + \dot{E}_{33} \cos^2 \omega \\ &+ 2\dot{E}_{12} \cos \phi \sin \phi \sin^2 \omega + 2\dot{E}_{23} \sin \omega \cos \omega \sin \phi \\ &+ 2\dot{E}_{13} \sin \omega \cos \omega \cos \phi\end{aligned}\quad (4.9)$$

and the active stress σ_f of each fibre contributes to the stress state in the RVE as

$$\mathbf{S}_{ij} = \frac{1}{V} \int_V \sigma_f(\omega, \phi) m_i(\omega, \phi) m_j(\omega, \phi) dV \quad \text{for } i, j = 1, \dots, 3 \quad (4.10)$$

which can be numerically calculated as an average value for all directions

$$\mathbf{S}_{ij}^{\text{active}} = \frac{1}{N_d} \sum_{k=1}^{N_d} \sigma_f(\omega_k, \phi_k) m_i(\omega_k, \phi_k) m_j(\omega_k, \phi_k) \quad (4.11)$$

Contact behaviour between cell and substrate At the region where the cell is in contact with the substrate, a behaviour for this contact needs to be described. McGarry *et al.* [57] used a simple adhesion model, in which the shear traction T_i between the cell membrane and the substrate at the contact region is given by a linear elastic relation as:

$$T_i = k_t \cdot \Delta_i, \quad (4.12)$$

where Δ_i is the relative sliding between the cell and the substrate, k_t (in $\text{nN}/\mu\text{m}^3$) is the shear stiffness of the adhesion. This shear stiffness can be understood as the product of

4. An efficient theoretical framework for cell contractility and adhesion

the concentration of focal adhesion complexes per unit area ($1/\mu\text{m}^2$) and the stiffness of the complex ($\text{nN}/\mu\text{m}$). An illustration for using this simple adhesion model together

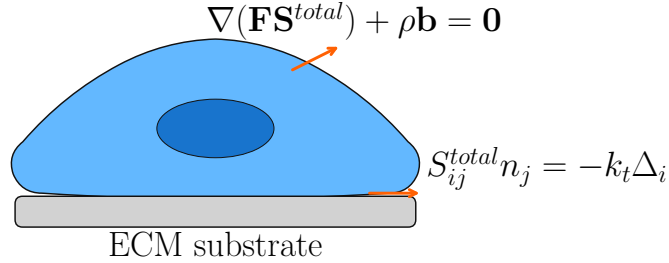


Figure 4.4: The adhesion behaviour needs to be described as a boundary condition at the region where the cell is in contact with the substrate.

with the bio-chemo-mechanical model is shown in Fig. 4.4.

Measure for actin distribution For every state of the activation level in the cell, there is a measure that is shown to be corresponding to the patterns of actin distribution [57]. This measure is defined as:

$$\Pi = \eta_{\max} - \bar{\eta}, \quad (4.13)$$

where η_{\max} is the maximum activation and $\bar{\eta}$ is the average activation in all directions. The mean value $\bar{\eta}$ is written as

$$\bar{\eta} = \frac{1}{\pi} \int_{-\pi/2}^{\pi/2} \eta(\phi) d\phi \quad (4.14)$$

for the 2D case, and

$$\bar{\eta} = \frac{1}{V} \int_V \eta(\omega, \phi) dV \quad (4.15)$$

in case of 3D. In the above configurations, these integrals are also computed numerically.

4.2. The bio-mechanical model for cell focal adhesion

The construction of the bio-mechanical model for cell focal adhesion (FA) of Deshpande *et al.* [17] is based on the investigation of the formation of FAs via the bonding of integrins in the cell surface to suitable ligands on the extracellular matrix (ECM). Integrins are known as adhesion receptors that are responsible for bidirectional transmission of signals

4. An efficient theoretical framework for cell contractility and adhesion

across the plasma membrane [111]. They exist in two conformational states: low-affinity (bent) and high-affinity (straight) integrins (Fig. 4.5), whereas only the latter form bonds.

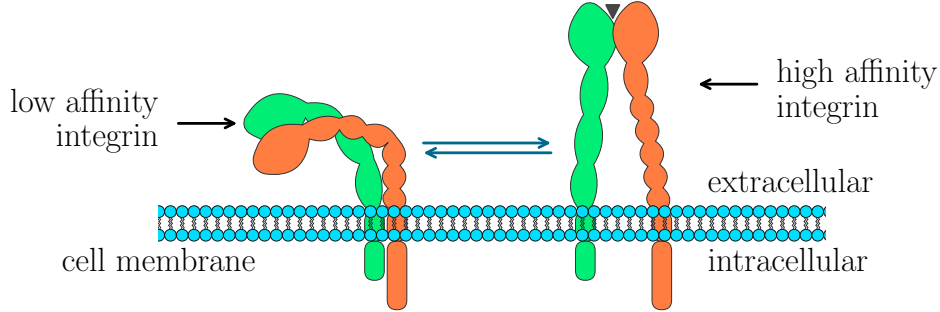


Figure 4.5: The bent (low-affinity) and extended-open (high-affinity) conformations of integrin. There exists a ligand-binding site in the high-affinity integrin, which is indicated by the triangle. Figure adapted from [45, 49].

Deshpande *et al.* [17] suggested that the chemical potential χ_L of low affinity integrins with a concentration ξ_L can be described as:

$$\chi_L = \mu_L + kT \ln \frac{\xi_L}{\xi_0} \quad (4.16)$$

where μ_L is the internal energy, ξ_0 is the total concentration of integrins, k is the Boltzmann constant and T is the absolute temperature.

Due to their straight configuration, high affinity integrins are less stable so it is expected that they have a higher reference potential compared to low affinity integrins ($\mu_H > \mu_L$). The chemical potential χ_H of high affinity integrins with a concentration ξ_H ($\xi_H + \xi_L = \xi_0$) when their bonds experience a stretching Δ_i is proposed as:

$$\chi_H = \mu_H + kT \ln \frac{\xi_H}{\xi_0} + \Phi(\Delta_i) - F_i \Delta_i \quad (4.17)$$

where Φ is the stretch energy stored in the integrin-ligand complex and $F_i \Delta_i$ is the mechanical work due to stretch Δ_i . The force F_i is dependent on the stretch energy and they are related by

$$F_i = \frac{\partial \Phi}{\partial \Delta_i} \quad (4.18)$$

As the formation of bonds and the conversion of the low affinity integrins to high affinity ones take place in a time scale much smaller than all other involved processes,

4. An efficient theoretical framework for cell contractility and adhesion

the concentrations of the integrins are determined from the thermodynamic equilibrium condition $\chi_H = \chi_L$. When this condition is met, the concentrations of high and low affinity integrins are obtained as:

$$\xi_H = \frac{\xi_0}{\exp\left[\frac{\mu_H - \mu_L + \Phi - F_i\Delta_i}{kT}\right] + 1} \quad (4.19)$$

$$\xi_L = \frac{\xi_0}{\exp\left[-\frac{\mu_H - \mu_L + \Phi - F_i\Delta_i}{kT}\right] + 1} \quad (4.20)$$

Finally, the stretch energy Φ is to be specified as a function of Δ_i to complete the model. As the integrin-ligand complexes have a finite rupture energy, the function Φ has to satisfy the condition that $\gamma \equiv \Phi(\Delta_i \rightarrow \infty)$ is a finite number. A simple piecewise quadratic function for the stretch energy is suggested as:

$$\Phi = \begin{cases} 0.5\kappa_s\Delta_e^2 & \Delta_e \leq \Delta_n \\ -\kappa_s\Delta_n^2 + 2\kappa_s\Delta_n\Delta_e - 0.5\kappa_s\Delta_e^2 & \Delta_n < \Delta_e \leq 2\Delta_n \\ \kappa_s\Delta_n^2 & \Delta_e > 2\Delta_n \end{cases} \quad (4.21)$$

where κ_s is the stiffness of the complex, $\Delta_e = \sqrt{\Delta_1^2 + \Delta_2^2}$ is the magnitude of the stretch. The plots for the stretch energy function and its derivative $\partial\Phi/\partial\Delta_e$ are shown in Fig. 4.6.

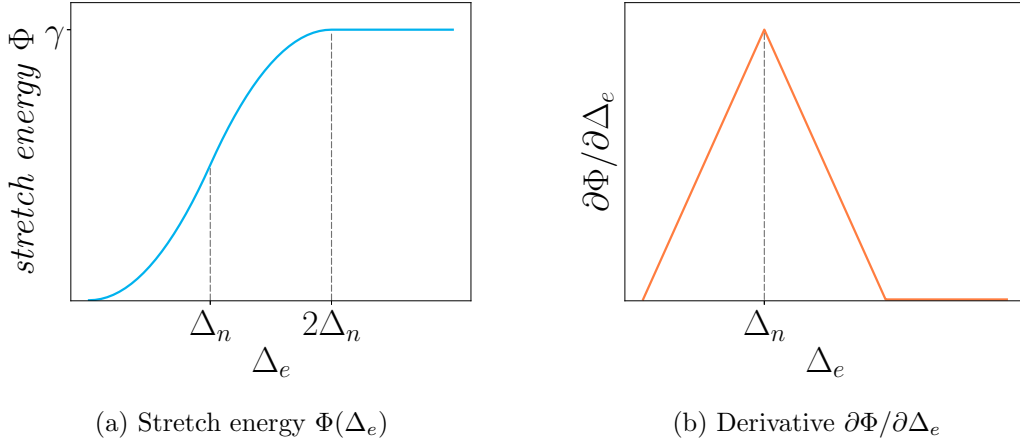


Figure 4.6: Plot for the stretch energy and its derivative with respect to the effective stretch.

To include the model of cell focal adhesion to simulations that use the continuum mechanics theory, the stretch of the complexes should be related to the deformation of

the system. In case of stiff substrate, a possible relation between the stretch Δ_i and the displacement u_i of the cell is given as follows [17, 71, 75, 77]:

$$\dot{\Delta}_i = \begin{cases} \dot{u}_i & \Delta_e \leq \Delta_n \quad \text{or} \quad \left[\frac{\partial \Phi}{\partial \Delta_e} \Delta_e < 0 \right], \\ 0 & \text{otherwise} \end{cases} \quad (4.22)$$

Moreover, the tractions on cell surface should be in equilibrium with the stresses at the boundary (Fig. 4.7). This equilibrium condition requires that $T_i = S_{ij}n_j = -\xi_H F_i$,

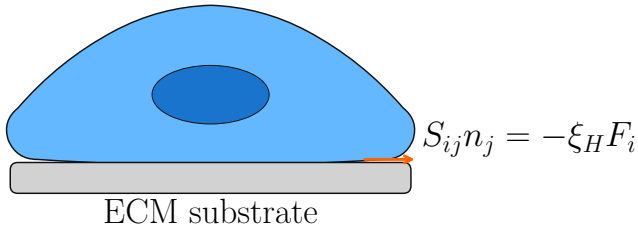


Figure 4.7: The model for cell focal adhesion is included as a boundary condition at the region where the cell is in contact with the substrate.

where n_j is the surface normal and S_{ij} are the components of the stress tensor \mathbf{S} in the cell. In 2D, the indexes $i, j \in \{1, 2\}$ refer to the horizontal and vertical directions. When coupling with the bio-chemo-mechanical model, this stress becomes $\mathbf{S}^{\text{total}} = \mathbf{S}^{\text{passive}} + \mathbf{S}^{\text{active}}$.

4.3. Finite element formulation for the coupled problem

In part due to its positive features and several advantages, the bio-chemo-mechanical has a high level of complexity compared to many other models. Devising an efficient software implementation that can be easily extended and applied for several simulations is therefore a demanding task. In this section, we present our approach to implementing the model in 2D in a way such that the generalisation in 3D can be obtained without much effort. We chose the simulation for cells on micro-post arrays, where the contact behaviour between the cell and the substrate needs to be described. For other 2D simulations, the implementation is often simpler and can be done in a similar way. In our approach, the mixed finite element method, in which several variables are approximated

simultaneously [9, 53, 86], is used for the contact problem. The solution space is then a mixed function space, which is the tensor product of several function spaces.

We utilise the open source framework *FEniCS* [53] to solve the system of partial differential equations. For the use of this software, the weak form of the system is derived in this section. The detail of the implementation in *FEniCS* is presented in the Appendix.

4.3.1. Time discretisation for the activation level

Applying the explicit Euler method for Eq. (4.2), we obtain:

$$\frac{\eta^{k+1} - \eta^k}{dt} = \left([1 - \eta^k] \frac{C\bar{k}_f}{\theta} - \left[1 - \frac{\sigma_f}{\sigma_0} \right] \eta^k \frac{\bar{k}_b}{\theta} \right) \quad (4.23)$$

where $dt = t^{k+1} - t^k$ is the time step and the superscript indicates the time step. For the detail of our implementation, Eq. (4.23) is solved at each element by multiplying it with a test function and integrating over the cell domain to obtain the weak form.

4.3.2. Computation of the active stress tensor

To obtain the active stress tensor, the integral in Eq. (4.8) has to be performed. In finite element implementation, a numerical integration scheme such as trapezoidal rule can be applied to compute this integral [16]. By dividing the interval $[-\pi/2, \pi/2]$ into N_d equal sub-intervals and letting ϕ_i be the grid points, with $i = 1, \dots, N_d + 1$, the components of the active stress tensors can be written as:

$$\begin{aligned} S_{11}^{\text{active}} &= \frac{1}{2N_d} \left(\sigma(\phi_1) \cos^2 \phi_1 + 2 \sum_{k=2}^{N_d} \sigma(\phi_k) \cos^2 \phi_k + \sigma(\phi_{N_d+1}) \cos^2 \phi_{N_d+1} \right) \\ S_{12}^{\text{active}} &= \frac{1}{4N_d} \left(\sigma(\phi_1) \sin 2\phi_1 + 2 \sum_{k=2}^{N_d} \sigma(\phi_k) \sin 2\phi_k + \sigma(\phi_{N_d+1}) \sin 2\phi_{N_d+1} \right) \\ S_{22}^{\text{active}} &= \frac{1}{2N_d} \left(\sigma(\phi_1) \sin^2 \phi_1 + 2 \sum_{k=2}^{N_d} \sigma(\phi_k) \sin^2 \phi_k + \sigma(\phi_{N_d+1}) \sin^2 \phi_{N_d+1} \right) \end{aligned} \quad (4.24)$$

4.3.3. Weak form for the coupled problem

The active stress is the only trigger for the deformation of the cell and there is no body force or surface traction applied. The cell is attached to the pillars via a simple adhesion

4. An efficient theoretical framework for cell contractility and adhesion

model, where the traction on the cell at the contact region is $T_i = k_t \cdot \Delta_i$, with k_t being a constant and Δ_i being the relative distance between the cell and the pillars. Assuming to have elastic behaviour and to be incompressible, the pillar is modelled as a disc of high Young's modulus value which is connected to a spring with stiffness constant k_s .

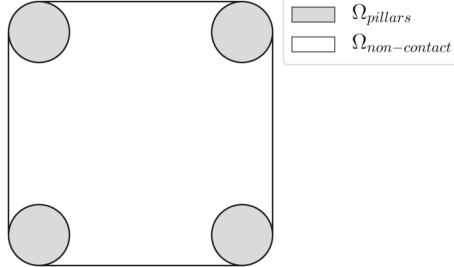


Figure 4.8: Division of the cell body into contact and non-contact regions. Illustrated is the cell on 2×2 pillars, but the same approach is used for other problems.

Our approach for solving the contact problem between the cell and the pillars is to first divide the cell domain into sub-domains:

$$\Omega = \Omega_{\text{pillars}} \cup \Omega_{\text{non-contact}}, \quad \text{with} \quad \Omega_{\text{pillars}} \cap \Omega_{\text{non-contact}} = \emptyset$$

where Ω_{pillars} is the sub-domain in which the cell is in contact with the pillars and $\Omega_{\text{non-contact}} = \Omega \setminus \Omega_{\text{pillars}}$ (Fig. 4.3.3). Then, using a mixed function space, the static problem is to find $\mathbf{u} = (\mathbf{u}_{\text{cell}}, \mathbf{u}_{\text{post}}) \in V \times V$, where V is the function space for the displacements, so that the equilibrium conditions are satisfied:

$$\nabla \cdot \mathbf{F}_{\text{cell}}(\mathbf{S}_{\text{cell}}^{\text{active}} + \mathbf{S}_{\text{cell}}^{\text{passive}}) = \mathbf{0} \quad \forall \mathbf{X} \in \Omega \quad (4.25)$$

$$\nabla \cdot \mathbf{F}_{\text{post}} \mathbf{S}_{\text{post}} = \mathbf{0} \quad \forall \mathbf{X} \in \Omega. \quad (4.26)$$

Here, the body weight is ignored and the gradient is taken with respect to the initial configuration. The transformation gradients for cell and posts are $\mathbf{F}_{\text{cell}} = \mathbf{1} + \nabla \mathbf{u}_{\text{cell}}$ and $\mathbf{F}_{\text{post}} = \mathbf{1} + \nabla \mathbf{u}_{\text{post}}$, while $\mathbf{S}_{\text{cell}}^{\text{passive}}$ and \mathbf{S}_{post} are the second Piola-Kirchhoff stresses in the cell and post domains, respectively.

Let $(\mathbf{w}_{\text{cell}}, \mathbf{w}_{\text{post}})$ be a test function in the mixed space $V \times V$, the weak form for the coupled problem can be written as:

$$\int_{\Omega} [\nabla \cdot \mathbf{F}_{\text{cell}}(\mathbf{S}_{\text{cell}}^{\text{active}} + \mathbf{S}_{\text{cell}}^{\text{passive}})] \cdot \mathbf{w}_{\text{cell}} \, dV + \int_{\Omega} [\nabla \cdot \mathbf{F}_{\text{post}} \mathbf{S}_{\text{post}}] \cdot \mathbf{w}_{\text{post}} \, dV = 0 \quad (4.27)$$

4. An efficient theoretical framework for cell contractility and adhesion

By applying the product rule $(\nabla \cdot \mathbf{FS}) \cdot \mathbf{w} = \nabla \cdot (\mathbf{FS} \cdot \mathbf{w}) - \nabla \mathbf{w} : (\mathbf{FS})$ and the divergence theorem for the integral of the term $\nabla \cdot (\mathbf{FS} \cdot \mathbf{w})$, the above weak form becomes:

$$\begin{aligned} & \int_{\Omega} \nabla \mathbf{w}_{\text{cell}} : [\mathbf{F}_{\text{cell}} (\mathbf{S}_{\text{cell}}^{\text{active}} + \mathbf{S}_{\text{cell}}^{\text{passive}})] \, dV - \int_{\Gamma_{\sigma}} \mathbf{T}_{\text{cell}}^* \cdot \mathbf{w}_{\text{cell}} \, dA \\ & + \int_{\Omega} \nabla \mathbf{w}_{\text{post}} : [\mathbf{F}_{\text{post}} \mathbf{S}_{\text{post}}] \, dV - \int_{\Gamma_{\sigma}} \mathbf{T}_{\text{post}}^* \cdot \mathbf{w}_{\text{post}} \, dA = 0 \end{aligned} \quad (4.28)$$

where $\mathbf{T}_{\text{cell}}^*$ and $\mathbf{T}_{\text{post}}^*$ are the tractions on the boundaries of the cell and the posts, respectively. With $\delta \mathbf{E}$ denoting the variation of the Green-Lagrange strain tensor, the identity $\nabla \mathbf{w} : (\mathbf{FS}) = \delta \mathbf{E} : \mathbf{S}$ holds. This identity is shown in [110] based on the fact that the scalar product of a symmetric tensor with the antisymmetric part of a tensor is zero and $\delta \mathbf{E}$ is the directional derivative of \mathbf{E} in the direction \mathbf{w} . The weak form is then written as:

$$\begin{aligned} & \int_{\Omega} (\mathbf{S}_{\text{cell}}^{\text{active}} + \mathbf{S}_{\text{cell}}^{\text{passive}}) : \delta \mathbf{E}_{\text{cell}} \, dV - \int_{\Gamma_{\sigma}} \mathbf{T}_{\text{cell}}^* \cdot \mathbf{w}_{\text{cell}} \, dA \\ & + \int_{\Omega} \mathbf{S}_{\text{post}} : \delta \mathbf{E}_{\text{post}} \, dV - \int_{\Gamma_{\sigma}} \mathbf{T}_{\text{post}}^* \cdot \mathbf{w}_{\text{post}} \, dA = 0 \end{aligned} \quad (4.29)$$

Now, on the boundaries where the cell is in contact with the posts, the traction due to the adhesion is applied on both the cell and the posts. Additionally, displacement of the post causes a traction due to the spring connected to it:

$$\mathbf{T}_{\text{cell}}^* = -k_t (\mathbf{u}_{\text{cell}} - \mathbf{u}_{\text{post}}) \quad (4.30)$$

$$\mathbf{T}_{\text{post}}^* = -k_t (\mathbf{u}_{\text{post}} - \mathbf{u}_{\text{cell}}) - \frac{k_s}{A_{\text{post}}} \mathbf{u}_{\text{post}} \quad (4.31)$$

where A_{post} is the cross-sectional area of each post. The final weak form is obtained as:

$$\begin{aligned} & \int_{\Omega} (\mathbf{S}_{\text{cell}}^{\text{active}} + \mathbf{S}_{\text{cell}}^{\text{passive}}) : \delta \mathbf{E}_{\text{cell}} \, dV + \int_{\Omega} \mathbf{S}_{\text{post}} : \delta \mathbf{E}_{\text{post}} \, dV \\ & + \int_{\Gamma_{\text{contact}}} \frac{k_s}{A_{\text{post}}} \mathbf{u}_{\text{post}} \cdot \mathbf{w}_{\text{post}} \, dA + \int_{\Gamma_{\text{contact}}} k_t (\mathbf{u}_{\text{cell}} - \mathbf{u}_{\text{post}}) \cdot \mathbf{w}_{\text{cell}} \, dA \\ & + \int_{\Gamma_{\text{contact}}} k_t (\mathbf{u}_{\text{post}} - \mathbf{u}_{\text{cell}}) \cdot \mathbf{w}_{\text{post}} \, dA = 0 \end{aligned} \quad (4.32)$$

In case that both the cell and the posts are thin flat plates, as assumed in the work of McGarry *et al.* [57], the plane stress problem can be applied. Then, the last three

boundary terms in the above equation can be written as volume integrals divided by the corresponding thickness. As \mathbf{u}_{post} is only defined in the post region, the following Dirichlet boundary condition is required for the convergence of the solution procedure: $\mathbf{u}_{\text{post}} = \mathbf{0}$ in $\Omega_{\text{non-contact}}$.

It should be noted that the obtained weak form for the coupled problem does not depend on the formulation of the activation level. To use the classical representation in [15], the only modifications in the implementation are the equation for the activation level and the construction of the active stress tensor.

4.4. Applications of the bio-chemo-mechanical model

The advantages of the bio-chemo-mechanical (BCM) model had led to it being employed to predict the results from several experimental studies on the mechanical responses of different cell types. Moreover, many *in silico* experiments have been performed based on the 2D and 3D versions of this mathematical model. In this section, a number of applications of the model are presented by showing the results obtained by our finite element software implementation in comparison with those in the literature.

4.4.1. Simulations of cells on micro-post arrays

Since the micro-needle array technique was introduced by Tan *et al.* [89] in their experiments, there have been many attempts for mathematical descriptions that can capture the behaviour of cells in such experiments. The analytical description of [65] suggests that the fibres experience some contraction when they are subjected to activated motor proteins or some chemical treatment. In this model, cell actin network is considered a discrete set of elastic filaments and a prestrain value is used to describe the fibre contraction. In the work of Nelson *et al.* [67], a prescribed thermal strain is also used to describe the contractility of the cell. However, instead of a set of discrete filaments, the cell is modelled as two layers with an isotropic incompressible elastic material: a contractile layer with a Young's modulus of 500Pa and a thinner passive layer with a value of 100Pa for Young's modulus.

Compared to such analytical descriptions, the bio-chemo-mechanical is more efficient in many aspects, for example in explaining the strong dependence of the forces generated by the cell on the post stiffness, or the distribution of actin filaments within the cells. By describing the focal adhesion between cells and posts at the contact area, McGarry

4. An efficient theoretical framework for cell contractility and adhesion

et al. [57] have shown that the model is applicable to numerical studies of the generated forces and the formation of actin within the cells of different cell lines.

Parameter	value	Parameter	value
σ_{\max}	3.9 [nN/ μm^2]	σ_{\max}	25 [nN/ μm^2]
θ	720 [s]	θ	70 [s]
\bar{k}_v	10	\bar{k}_v	7
\bar{k}_f	10	\bar{k}_f	10
\bar{k}_b	1	\bar{k}_b	1
$\dot{\varepsilon}_0$	$2.8 \cdot 10^{-4}$ [s $^{-1}$]	$\dot{\varepsilon}_0$	0.003 [s $^{-1}$]
E_{cell}	0.4 [nN/ μm^2]	E_{cell}	0.4 [nN/ μm^2]
ν_{cell}	0.3	ν_{cell}	0.3

(a)

(b)

Table 4.1: Two sets of parameters for the BCM model and cell material properties.

Smooth muscle cells on regular post-arrays McGarry *et al.* [57] performed the simulations of the development of actin in smooth muscle cells when they are cultured on arrays of 2×2 , 3×3 and 4×4 posts. Their results could capture several outcomes from the experiments of Tan *et al.* [89]. For example, the average deflection of the pillars and the highest concentration of actin were well predicted. Figure 4.9 shows the results for actin distribution of muscle cells from our implementation based on the models described by McGarry *et al.* [57]. Parameters for the BCM model are given in Table 4.1b. For the passive stress in the cell, the linear elasticity material model is used. The values for Young's modulus and Poisson's ratio can also be found in this table. The posts are with $1.5\mu\text{m}$ radius and $32\text{nN}/\mu\text{m}$ bending stiffness, the spacing between post centres is $10\mu\text{m}$. The cell thickness is $b = 1\mu\text{m}$ and the adhesion stiffness is $k_t = 500\text{nN}/\mu\text{m}^3$. For the simulations of cells on 2×2 and 3×3 posts, no difference was found in our results compared to those in [57]. In case of 4×4 posts, we observed a slight difference between our result and that in [57], but the prediction of experimental outcome remains valid. That is, the highest actin distribution is located near the cell periphery and the borders of the posts, while the cell central region appeared with a low distribution.

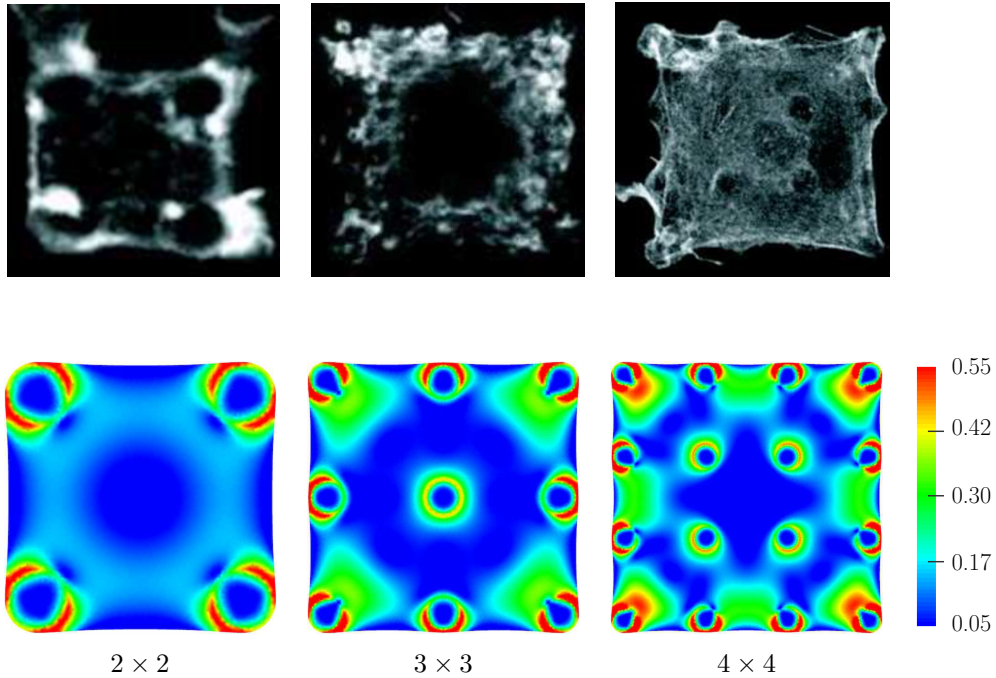


Figure 4.9: Predicted steady-state distribution of actin of smooth muscle cells on arrays of 2×2 , 3×3 and 4×4 micro-posts, in comparison with experimental results by Tan *et al.* [89]. The simulations were first done by McGarry *et al.* [57]. Shown are results using our implementation with FEniCS.

The influence of post stiffness An advantage of the bio-chemo-mechanical model is that it can capture the strong dependence of the stress generated by the cell and the formation of actin filaments on the compliance of the substrate. This feature of the model was demonstrated in [57] by investigating the responses of cells for different stiffness values of the posts, while the same geometry of the post arrays was used. For three values of post's normalised bending stiffness, which is defined as $\bar{k}_s = k_s / (\sigma_{\max} \cdot b)$, where b is the cell thickness, the steady-state actin distribution of a muscle cell on an array of 5×5 posts was computed. Figure 4.10 shows our results using the open source software FEniCS, which are in very good agreement with those in [57]. The results illustrated that for stiffer posts, the higher level of actin polymerisation within the cell is produced and therefore higher contractile forces by the cells are obtained.

The influence of post distance For posts of the same material properties, the geometrical parameters, such as their cross-sectional area or the spacing between them, have effects on the responses of cells. Figure 4.11 shows the plots of actin distribution

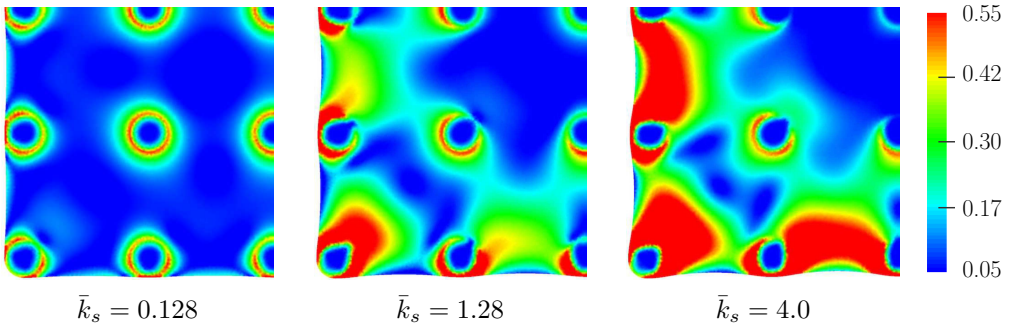


Figure 4.10: Our FEniCS result for a single muscle cell on 5×5 posts with three different normalised bending stiffnesses \bar{k}_s . The parameters in [57] are used (Tab. 4.1b). The post radius is $1.5\mu\text{m}$, while the distance between two posts is $10\mu\text{m}$.

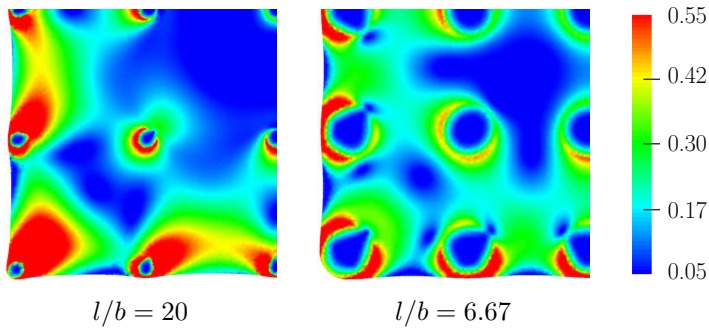


Figure 4.11: Our FEniCS results for a cell on an array of 5×5 posts with two different post distances. The value $b = 1\mu\text{m}$ is used for the cell thickness.

for two configurations of posts, where different values for the spacing between the posts are used ($l = 20\mu\text{m}$ and $l = 6.67\mu\text{m}$), from our implementation. The results are in very good agreement with those in [57], which illustrated the effect that a larger post spacing resulted in a higher actin distribution near the posts.

Fibroblast on an irregular array of 29 posts The bio-chemo-mechanical model is applicable for different cell lines and is not limited to symmetric geometries of the cells. Using a smaller value of the maximum stress, i.e. $\sigma_{\max} = 3.25\text{nN}/\mu\text{m}^2$, McGarry *et al.* [57] conducted a simulation for the response of a fibroblast on an irregular array of 29 posts. Their predicted steady-state actin distribution agreed very well with their experimental results. Figure 4.12c shows our FEniCS result, which has been done using

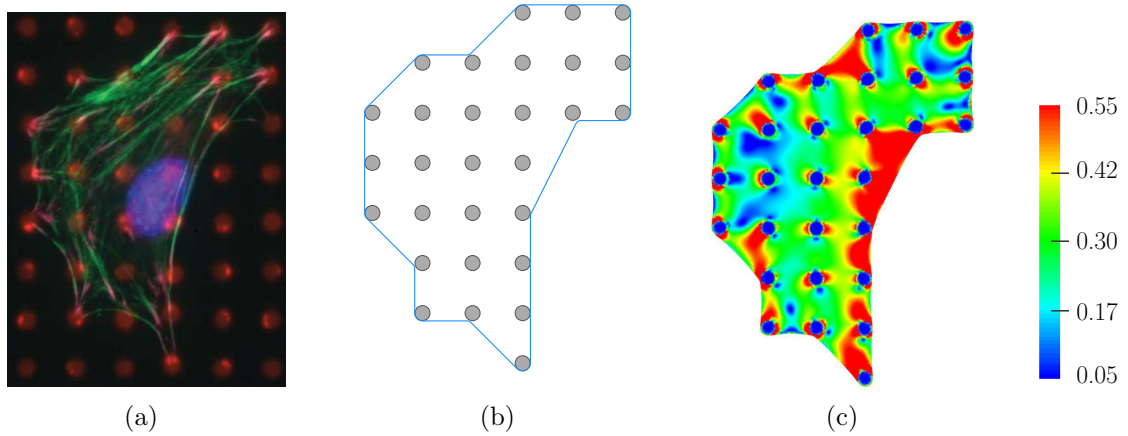


Figure 4.12: (a) A fibroblast cell spreads over 29 posts in the experiment of McGarry *et al.* [57]. (b) The shape of the cell in our simulation and the sub-domains where the cell is in contact with the posts. (c) Plot for our predicted steady-state distribution of actin filaments (characterised by the measure Π in Eq. (4.13)) for simulation of a fibroblast on an irregular of 29 posts. The study was first done by McGarry *et al.* [57].

the model and parameters described by McGarry *et al.* [57]. We constructed our cell shape using straight lines connected smoothly to their neighbours. Due to using a different geometry, we observed a slight difference in our result in comparison with that by McGarry *et al.* [57]. However, the steady-state actin distribution in the experiment is still very well predicted.

4.4.2. Development of actin cytoskeleton and focal adhesion

The bio-chemo-mechanical model can be combined with the bio-mechanical model for cell adhesion (presented in Section 4.2) to simulate the development of the stress fibres in the cell and the integrins at the contact regions. Pathak *et al.* [71] performed such simulations for cells of different shapes.

The features of the combination of the two models were demonstrated by studying a triangular cell and a circular cell on a ligand patch of the same shape. The dimensions of the cells are illustrated in Fig. 4.13. For both cell shapes, the parameters in Tab. 4.2 are used for the BCM model and the focal adhesion model. The variables to be solved for are the deformation of the cell, the activation with the cell, and the concentration of

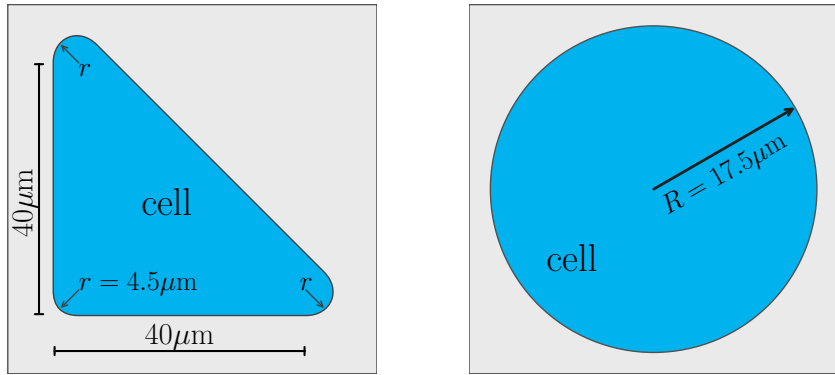


Figure 4.13: The size of a triangular and a circular cell. Figures adapted from [71].

high affinity integrins at contact regions.

Parameter	value	Parameter	value
σ_{\max}	4.0 [nN/μm ²]	T	310 [K]
θ	720 [s]	$\mu_H - \mu_L$	5 [kT]
\bar{k}_v	6	κ_S	0.015 [nN/μm]
\bar{k}_f	10	Δ_n	130 [nm]
\bar{k}_b	1	ξ_0	1000 [1/μm ²]
$\dot{\varepsilon}_0$	$2.8 \cdot 10^{-4}$ [s ⁻¹]		
E_{cell}	0.08 [nN/μm ²]		
ν_{cell}	0.3		

Table 4.2: The parameters for the BCM model (left) and the focal adhesion model (right).

The plots for the steady-state distributions of stress fibre concentration, which is characterised by $\Gamma = (\eta_{\max} - \bar{\eta})/\eta_{\max}$, and high affinity integrin concentration are shown in Fig. 4.14 and Fig. 4.15. Here are our results using our implementation with FEniCS, which are in very good agreement with those in [71]. The results demonstrated that, for both cell shapes, high actin distribution and high focal adhesion concentrations are found along the cell periphery. In the interior part of the cells, the network of actin

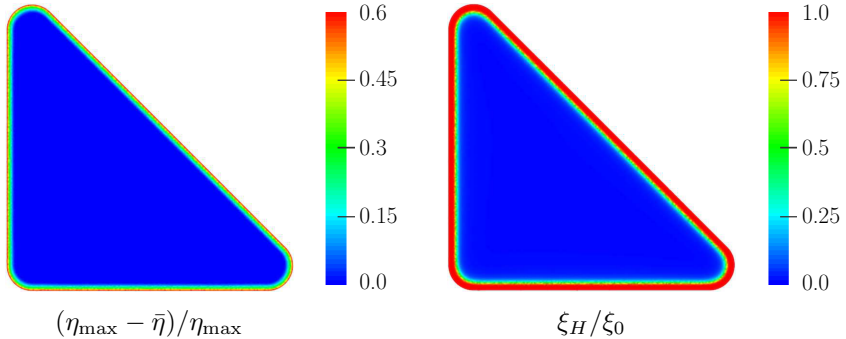


Figure 4.14: Plots for predicted steady-state distributions of the stress fibre (above) and high affinity integrins (below) concentrations for a triangular cell on a ligand pattern of the same shape as in [71]. Our FEniCS results using the BCM model in combination with the focal adhesion model. Obtained results are in very good agreement to those in [71].

filaments is almost isotropic [71].

The development of the focal adhesion over time was studied by computing the concentrations of the integrins at different time periods. Figure 4.16 shows these concentrations for the circular cell at different locations, determined by the distance r to the cell centre. At the initial state, the integrins are distributed uniformly in the cell, where the low affinity integrins are dominating. In response to the contractility of the cell, the focal adhesions developed and the evolution happened in a time scale much smaller than the stress fibre development. Large changes were found in the concentrations of the high and low affinity integrins within the time of $t = 0.5\theta$, while no significant change found after $t = 9\theta$. The deformation of the cell caused the transformation from low to high affinity integrins. At the cell periphery, where the cell experienced largest deformation, the concentration of high affinity integrins was highest.

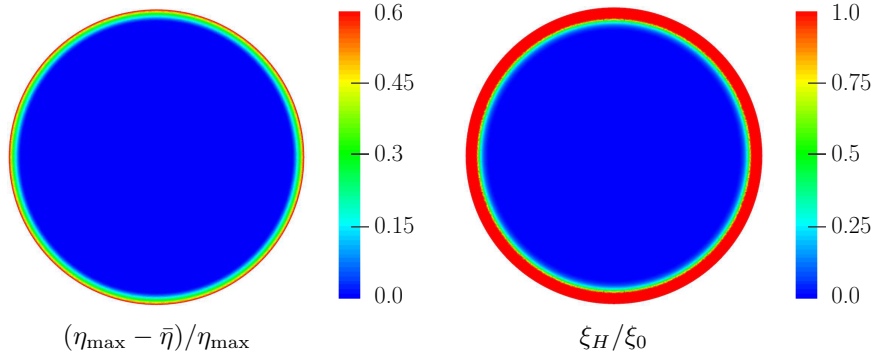


Figure 4.15: Plots for predicted steady-state distributions of the stress fibre (above) and high affinity integrins (below) concentrations for a circular cell on a ligand pattern of the same shape as in [71].

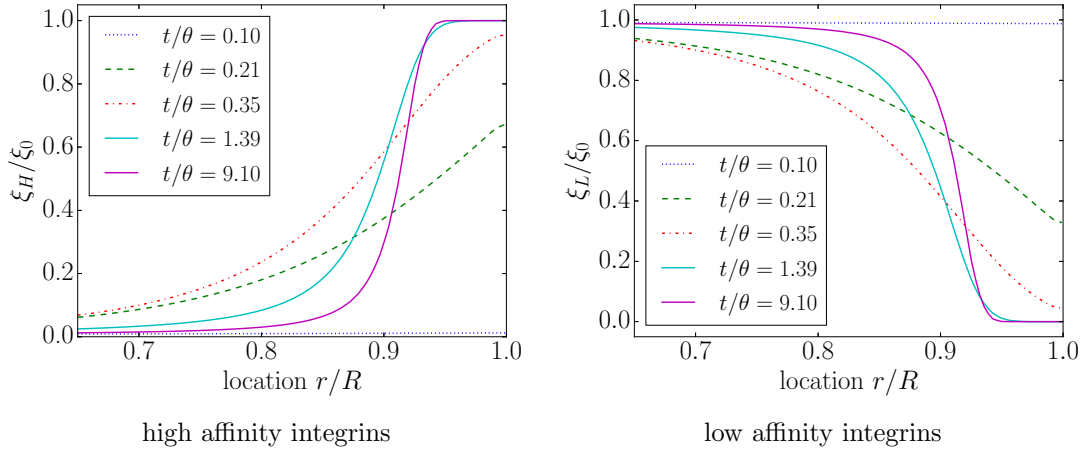


Figure 4.16: Normalised concentrations of high and low affinity integrins for the circular cell. Results obtained from our implementation and are in very good agreement with those in [71].

5. Model order reduction of the bio-chemo-mechanical model

This chapter includes my contribution to the journal article [3].

The applicabilities and the advantages of the bio-chemo-mechanical have been confirmed in numerous studies [15–17, 20, 57, 71, 73–77]. The very advantageous features of the model came at the cost of high complexity and hence high computation requirements. The solution procedure includes sampling a large number of stress fibre directions at every point in the cell and solving for the activation level in these directions. The number of degrees of freedom to be solved for is therefore very high in 3D analysis, and even in many 2D simulations. Presented in this chapter is our approach to reducing the complexity of the model by employing a quadratic form to approximate the activation level at every point in the cell. The results obtained with our formulation are close to those presented in the literature, while the computation time is significantly reduced.

5.1. Semi-analytical formulation

The key idea of coupling the bio-chemo-mechanical model to the equations of continuum mechanics is to add the active stress tensor to the computation of the total stress at every point in the cell. This active stress tensor is the average of active tension in stress fibres in all directions. Usually, a large number of directions is defined and the activation level in the cell, which is described in Eq. (4.2), is solved in these directions. Our semi-analytical formulation is derived based on the approximation of the distribution of the activation level η at every point in the cell by a quadratic function restricted to a circle in 2D and to a sphere in 3D.

In our quadratic representation, the activation level in the direction characterised by

5. Model order reduction of the bio-chemo-mechanical model

an angle ϕ is written as:

$$\eta(\phi) = a_{11} \cos^2(\phi) + 2a_{12} \cos(\phi) \sin(\phi) + a_{22} \sin^2(\phi) \quad (5.1)$$

where a_{11}, a_{12}, a_{22} are the coefficients of the ellipse and are different for different material points in the cell. The activation in any direction at a given point can be determined

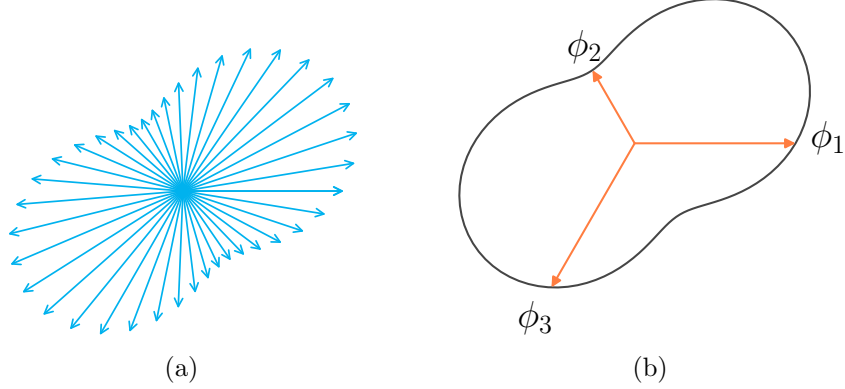


Figure 5.1: (a) A possible configuration for the activation level at a point in 2D using the classical representation and (b) an approximation using our quadratic representation and the basis directions that determine them. Here, a possible basis for the quadratic representation are the three vectors $(\cos(\phi_i), \sin(\phi_i))$ for $\phi_i \in \{0, 2\pi/3, 4\pi/3\}$.

when the values of these coefficients are known. So, instead of solving the activation for a large number of directions, it is sufficient to solve for these three values. The formulation is completed by establishing the evolution equation for the a_{ij} coefficients based on Eq. (4.2).

Let ϕ_1, ϕ_2 and ϕ_3 be the three angles corresponding to the basis directions that determine the quadratic form (Fig. 5.1b), the evolution of the activation level in these directions is obtained as:

$$\dot{\eta}(\phi_i) = \dot{a}_{11} \cos^2(\phi_i) + 2\dot{a}_{12} \cos(\phi_i) \sin(\phi_i) + \dot{a}_{22} \sin^2(\phi_i), \quad i = 1, \dots, 3 \quad (5.2)$$

As $\cos(\phi_i)$ and $\sin(\phi_i)$ are constant values for the known angles ϕ_i , the above equation can be written in matrix form as:

$$\begin{pmatrix} \dot{\eta}(\phi_1) \\ \dot{\eta}(\phi_2) \\ \dot{\eta}(\phi_3) \end{pmatrix} = \mathbf{C}_e \cdot \begin{pmatrix} \dot{a}_{11} \\ \dot{a}_{12} \\ \dot{a}_{22} \end{pmatrix} \quad (5.3)$$

5. Model order reduction of the bio-chemo-mechanical model

where \mathbf{C}_e is the 3×3 matrix whose components c_{ij} are as follow:

$$c_{i1} = \cos^2(\phi_i), c_{i2} = 2 \cos(\phi_i) \sin(\phi_i), c_{i3} = \sin^2(\phi_i), \quad i = 1, \dots, 3.$$

Then the time derivative of the a_{ij} coefficients can be achieved as:

$$\begin{pmatrix} \dot{a}_{11} \\ \dot{a}_{12} \\ \dot{a}_{22} \end{pmatrix} = \mathbf{C}_e^{-1} \cdot \begin{pmatrix} \dot{\eta}(\phi_1) \\ \dot{\eta}(\phi_2) \\ \dot{\eta}(\phi_3) \end{pmatrix} \quad (5.4)$$

Since η is an expression of a_{ij} , this equation describes the rate of change of a_{ij} as a function of a_{ij} .

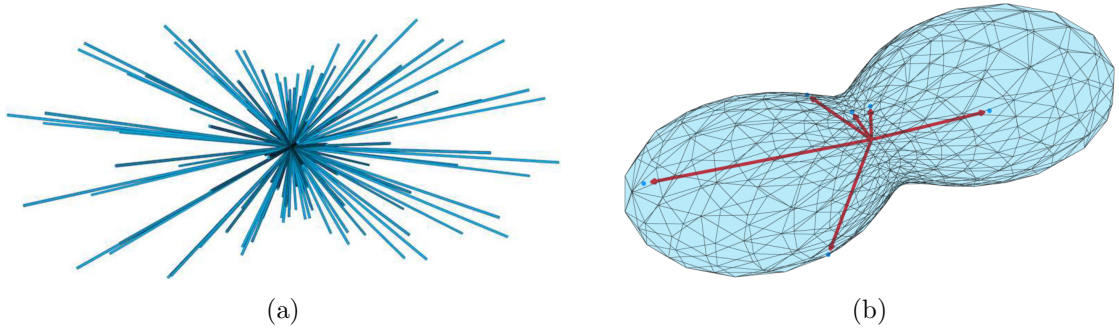


Figure 5.2: (a) A possible configuration for the activation level at a point in 3D using the classical representation and (b) an approximation using our 3D quadratic representation and the directions that determine them. The six directions for the quadratic representation are corresponding to the vectors $(0, \lambda_1, \pm\lambda_2), (\lambda_1, \pm\lambda_2, 0), (\pm\lambda_2, 0, \lambda_1)$ in the Cartesian coordinate system, where $\lambda_1 = 1/\sqrt{1 + \phi^2}, \lambda_2 = \lambda_1 \cdot \phi$ with $\phi = (1 + \sqrt{5})/2$.

In a similar way, the approximation of the activation level in 3D by a quadratic form suggests that its value in the direction associated with the pair of angles (ω, ϕ) in the spherical coordinate system has the form:

$$\begin{aligned} \eta(\omega, \phi) = & a_{11} \sin^2 \omega \cos^2 \phi + a_{22} \sin^2 \omega \sin^2 \phi + a_{33} \cos^2 \omega \\ & + 2a_{12} \cos \phi \sin \phi \sin^2 \omega + 2a_{23} \sin \omega \cos \omega \sin \phi \\ & + 2a_{13} \sin \omega \cos \omega \cos \phi \end{aligned} \quad (5.5)$$

Let $(\omega_i, \phi_i), i = 1, \dots, 6$ be the six basis directions that determine the quadratic form

5. Model order reduction of the bio-chemo-mechanical model

(Fig. 5.2), the components c_{ij} of the matrix \mathbf{C}_e are obtained as:

$$\begin{aligned} c_{i1} &= \sin^2 \omega_i \cos^2 \phi_i, & c_{i2} &= 2 \cos \phi_i \sin \phi_i \sin^2 \omega_i, \\ c_{i3} &= 2 \sin \omega_i \cos \omega_i \cos \phi_i, & c_{i4} &= \sin^2 \omega_i \sin^2 \phi_i, & i &= 1, \dots, 6 \\ c_{i5} &= 2 \sin \omega_i \cos \omega_i \sin \phi_i, & c_{i6} &= \cos^2 \omega_i, \end{aligned}$$

so that the evolution in time for the coefficients a_{ij} is written as:

$$\begin{pmatrix} \dot{a}_{11} \\ \dot{a}_{12} \\ \dot{a}_{13} \\ \dot{a}_{22} \\ \dot{a}_{23} \\ \dot{a}_{33} \end{pmatrix} = \mathbf{C}_e^{-1} \cdot \begin{pmatrix} \dot{\eta}(\omega_1, \phi_1) \\ \dot{\eta}(\omega_2, \phi_2) \\ \dot{\eta}(\omega_3, \phi_3) \\ \dot{\eta}(\omega_4, \phi_4) \\ \dot{\eta}(\omega_5, \phi_5) \\ \dot{\eta}(\omega_6, \phi_6) \end{pmatrix} \quad (5.6)$$

Average and maximum value of activation level The average value for the activation level η can be obtained as an expression of the coefficients a_{ij} by an analytic integration. For instance, $\bar{\eta}$ can be written as:

$$\begin{aligned} \bar{\eta} &= \frac{1}{\pi} \int_{-\pi/2}^{\pi/2} \eta d\phi = \frac{1}{\pi} \int_{-\pi/2}^{\pi/2} (a_{11} \cos^2(\phi) + 2a_{12} \cos(\phi) \sin(\phi) + a_{22} \sin^2(\phi)) d\phi \\ &= \frac{1}{2} a_{11} + \frac{1}{2} a_{22} \end{aligned} \quad (5.7)$$

In a similar way, an integration of (5.5) over the domain $[0, 2\pi] \times [0, \pi]$ gives

$$\bar{\eta} = \frac{1}{3} a_{11} + \frac{1}{3} a_{22} + \frac{1}{3} a_{33}$$

for the 3D case.

The maximum and minimum values of η are actually evaluated at the angles associated with the minor and the major axes of the corresponding ellipse, which is the isosurface of the quadratic form. Finding these values involves solving an eigenvalue problem for the matrix of coefficients a_{ij} . In 2D, they are simply the maximum and minimum values of η evaluated at two angles:

$$\begin{aligned} \alpha_{\text{crit1}} &= \frac{1}{2} \arctan \left(\frac{a_{11} - a_{22}}{2a_{12}} \right) \\ \alpha_{\text{crit2}} &= \alpha_{\text{crit1}} + \pi/2 \end{aligned}$$

There are no such simple explicit formulas in 3D, but applying an eigenvalue solver still makes the implementation simple.

5. Model order reduction of the bio-chemo-mechanical model

Components of the active stress tensor In 2D, by replacing η and $\dot{\varepsilon}$ in Eq. (4.3) by those in Eq. (5.1) and Eq. (4.6), the integrals in Eq.(4.7) are obtained as:

$$\begin{aligned} S_{11}^{\text{active}} &= \frac{1}{2}\sigma_{\max} \left(\frac{3a_{11} + a_{22}}{4} + \bar{k}_v \frac{3\dot{E}_{11} + \dot{E}_{22}}{4\dot{\varepsilon}_0} \right) \\ S_{22}^{\text{active}} &= \frac{1}{2}\sigma_{\max} \left(\frac{a_{11} + 3a_{22}}{4} + \bar{k}_v \frac{\dot{E}_{11} + 3\dot{E}_{22}}{4\dot{\varepsilon}_0} \right) \\ S_{12}^{\text{active}} &= \frac{1}{2}\sigma_{\max} \left(\frac{a_{12}}{2} + \bar{k}_v \frac{\dot{E}_{12}}{4\dot{\varepsilon}_0} \right) \end{aligned} \quad (5.8)$$

In a similar way, the components of the active stress tensor in 3D can be related to the coefficients a_{ij} and the strain rate $\dot{\mathbf{E}}$ as:

$$\begin{aligned} S_{11}^{\text{active}} &= \sigma_{\max} \left(\frac{3a_{11} + a_{22} + a_{33}}{15} + \bar{k}_v \frac{3\dot{E}_{11} + \dot{E}_{22} + \dot{E}_{33}}{15\dot{\varepsilon}_0} \right) \\ S_{22}^{\text{active}} &= \sigma_{\max} \left(\frac{a_{11} + 3a_{22} + a_{33}}{15} + \bar{k}_v \frac{\dot{E}_{11} + 3\dot{E}_{22} + \dot{E}_{33}}{15\dot{\varepsilon}_0} \right) \\ S_{33}^{\text{active}} &= \sigma_{\max} \left(\frac{a_{11} + a_{22} + 3a_{33}}{15} + \bar{k}_v \frac{\dot{E}_{11} + \dot{E}_{22} + 3\dot{E}_{33}}{15\dot{\varepsilon}_0} \right) \\ S_{12}^{\text{active}} &= \sigma_{\max} \left(\frac{2a_{12}}{15} + \bar{k}_v \frac{2\dot{E}_{12}}{15\dot{\varepsilon}_0} \right) \\ S_{13}^{\text{active}} &= \sigma_{\max} \left(\frac{2a_{13}}{15} + \bar{k}_v \frac{2\dot{E}_{13}}{15\dot{\varepsilon}_0} \right) \\ S_{23}^{\text{active}} &= \sigma_{\max} \left(\frac{2a_{23}}{15} + \bar{k}_v \frac{2\dot{E}_{23}}{15\dot{\varepsilon}_0} \right) \end{aligned} \quad (5.9)$$

5.2. Weak formulation for finite element implementation

For finite element software implementation, a weak formulation for the coupled problem using our quadratic representation has to be derived. Compared to the classical representation in section 4.3, only the equation of the activation level and the construction of the active stress tensor are different.

Integration of the Eq. (5.4) over the cell domain gives:

$$\int_{\Omega} \begin{pmatrix} \dot{a}_{11} \\ \dot{a}_{12} \\ \dot{a}_{22} \end{pmatrix} dx = \int_{\Omega} \mathbf{C}_e^{-1} \cdot \begin{pmatrix} \dot{\eta}(\phi_1) \\ \dot{\eta}(\phi_2) \\ \dot{\eta}(\phi_3) \end{pmatrix} dx \quad (5.10)$$

Applying the explicit-time integration method for the above equation, we obtain:

$$\frac{1}{dt} \int_{\Omega} \begin{pmatrix} a_{11}^{k+1} - a_{11}^k \\ a_{12}^{k+1} - a_{12}^k \\ a_{22}^{k+1} - a_{22}^k \end{pmatrix} dx = \frac{1}{dt} \int_{\Omega} \mathbf{C}_e^{-1} \cdot \begin{pmatrix} \eta^{k+1}(\phi_1) - \eta^k(\phi_1) \\ \eta^{k+1}(\phi_2) - \eta^k(\phi_2) \\ \eta^{k+1}(\phi_3) - \eta^k(\phi_3) \end{pmatrix} dx \quad (5.11)$$

where $dt = t^{k+1} - t^k$ is the time step and the superscript indicates the time step. The right hand side can be obtained from the values of the activation level at the previous time step using Eq. (4.2) as:

$$\int_{\Omega} \frac{\eta^{k+1}(\phi_i) - \eta^k(\phi_i)}{dt} dx = \int_{\Omega} \left([1 - \eta^k(\phi_i)] \frac{C \bar{k}_f}{\theta} - \left[1 - \frac{\sigma_f^k}{\sigma_0} \right] \eta^k(\phi_i) \frac{\bar{k}_b}{\theta} \right) dx \quad (5.12)$$

For the active stress tensor, its components are computed as in Eq. (5.8), instead of using a numerical integration.

5.3. Results and error analysis

In order to evaluate our semi-analytical formulation, we have compared the results using our approach and those in the literature. Different simulations with various range of complexity have been reproduced. Moreover, an error analysis was performed to confirm the appropriateness of our quadratic representation.

5.3.1. Results

We have performed all the simulations presented in Section 4.4, where our semi-analytical formulation was used instead of the classical representation. Our obtained results are almost identical to those in the literature. The good agreement of our results shows that the applicability of our method is not limited to some simple problems, but also to simulations of high complexity, such as those which include a contact behaviour between the cell and the substrate, or those which are coupled with the focal adhesion model.

To further demonstrate our approach, we present here two more examples: a 2D problem where an analytical solution can be derived; and the use of our quadratic

5. Model order reduction of the bio-chemo-mechanical model

representation in 3D simulation. The advantage in computing time of our method is also illustrated by a performance analysis.

Cell under bi-axial isometric tension We use the demonstrating example by Deshpande *et al.* [16], where a rectangular cell is subjected to a single activation signal at $t = 0$. The cell is constrained such that the top and the bottom sides cannot move vertically, the left and the right sides of the cell cannot move horizontally (Fig. 5.3a). Under these conditions, the strain has a zero value at every time step ($\mathbf{E} = \dot{\mathbf{E}} = \mathbf{0}$) resulting that the active stresses always get the isometric value ($\sigma_f = \sigma_0$) in any direction. Thus, the activation level η has the same value in any direction and increases

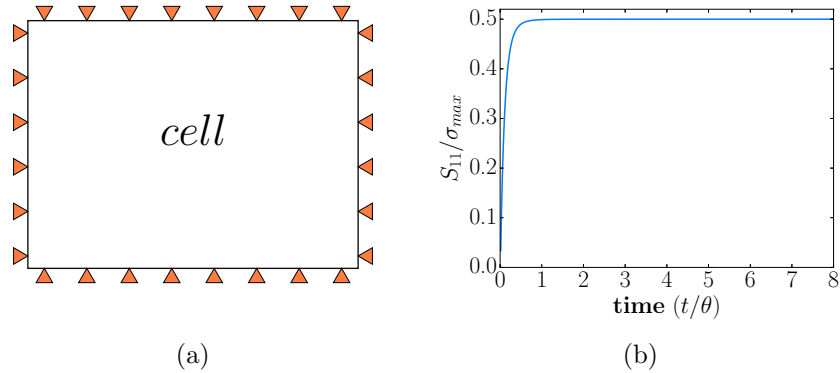


Figure 5.3: Cell under bi-axial isometric tension and the plot for the normalised active stress S_{11} over time. The parameters from Table 4.1a are used. The left figure is adapted from [16], the right figure is the result using our elliptic representation.

until the maximum value ($\eta = 1$) is reached at the steady state. In our formulation, this means that at every point, the coefficient a_{12} is zero, and the distribution of the activation level η is a circle with radius $a_{11} = a_{22}$ (see Eq. (5.1)). At the steady state, the average activation level is obviously $\bar{\eta} = 1$ (as from Eq. (5.7) with $a_{11} = a_{22} = 1$) and the components of the active stress tensor obtained analytically from Eq. (5.8) are $S_{11} = S_{22} = 0.5 \cdot \sigma_{\max}$ (Fig. 5.3b), which are exactly the results described in [16].

Improvement in computing time In order to evaluate the advantage in computing time of the quadratic representation, we set up three configurations to use the BCM model:

- with the divisions of the interval $[-\pi/2, \pi/2]$ into 36 and 72 equal angles,

5. Model order reduction of the bio-chemo-mechanical model

- with the elliptic distribution of the activation level

and applied it for two different simulations:

- the bi-axial isometric tension example with a mesh such that the number of degrees of freedom (DOFs) to solve for the cell displacement is 442, with the timestep $\Delta t = 1\text{s}$ until the time $t = 10,000\text{s}$ is reached,
- the example with a cell on a micro-post array with 37,372 DOFs for the displacement, with the time-step $\Delta t = 1\text{s}$ and the end time is at 400s,

on a computer with 32GB RAM, Intel(R) Xeon(R) CPU E5-1607 v2 @ 3.00GHz. No parallelism like OpenMP is utilised.

	72 directions	36 directions	quadratic form
Bi-axial tension	2356.0	682.0	53.8
Cell on posts	5852.6	2109.3	553.8

Table 5.1: Computing time (in seconds) for three different configurations of two simulation set-ups: the bi-axial isometric tension example with a mesh of 221 nodes and the cell on micro-post arrays with a mesh of 18,686 nodes.

It can be seen from Tab. 5.1 that for both simulation set-ups, using our quadratic representation gives a much better performance compared to dividing the half circle into many equal angles. Moreover, it can also be noticed that less advantage is obtained from the elliptic representation when the mesh is finer. The explanation is that the computing time spent to compute the cell deformation is dominant when the size of the system matrix is large. Nevertheless, the computation is still 5-10 times faster. This will be especially important when the problem under study is more complex and realistic.

A 3D example To demonstrate the quadratic representation in 3D, we run a simulation for a round cell on a stiff substrate. Its geometry is adapted from Ronan *et al.* [74]. Two configurations are set up: (i) with the ellipsoidal approximation for the activation level, and (ii) with 120 directions for stress fibres spaced so that the minimum distance between each fibre and its neighbours is maximised. As in [74], the cell nucleus and the cytoplasm are assumed to have different material properties. The linear elasticity model is used for the passive stresses of both nucleus and cytoplasm whereas the active stress caused by stress fibre activation is only applied to the cytoplasm. The parameters from Table 4.1b are used where the value $E_{\text{nuc}} = 4.0\text{nN}/\mu\text{m}^2$ is suggested for the Young's modulus of the

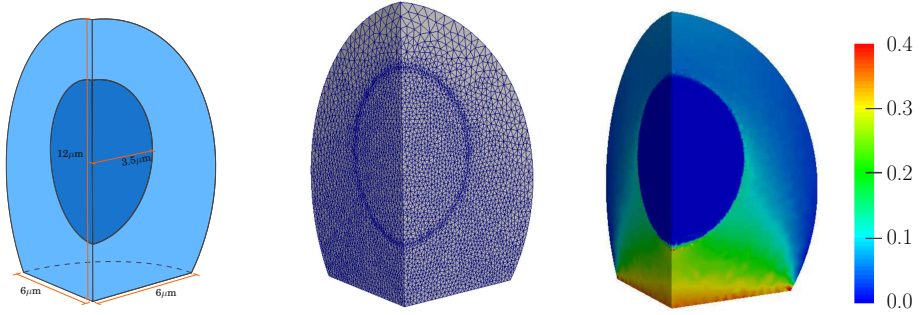


Figure 5.4: Dimensions of a round cell (left, adapted from [74]), mesh (middle) and plot for the average activation level $\bar{\eta}$ at the steady state (right). Our quadratic representation for the BCM model is used with the six basic directions specified in Fig. 5.2b.

nucleus. As in [57], a simple shear adhesion is used for the contact between the cell and the substrate, with the shear stiffness value $k_t = 500\text{nN}/\mu\text{m}^3$. Two meshes with 58,566 and 173,024 tetrahedral elements are used where a refinement is done at the transition between the cytoplasm and the nucleus and at the contact region. The computation on

	$\sim 58k$ elements	$\sim 173k$ elements
quadratic repr.	1.38 hours	10.64 hours
120 directions	15.92 hours	not possible due to insufficient memory

Table 5.2: Computation time of the 3D simulation on two meshes for our quadratic approximation and the classical representation with 120 directions. The computer used is with 32GB RAM, Intel(R) Xeon(R) CPU E5-1607 v2 @ 3.00GHz.

the finer mesh was only possible with our quadratic representation, using our computer with 32GB RAM, Intel(R) Xeon(R) CPU E5-1607 v2 @ 3.00GHz. In case of the coarser mesh, we obtained almost identical results for both configurations, with the maximum relative error for cell displacement being around 3.4%. A plot for the steady state value of the average activation level $\bar{\eta}$ is shown in Fig. 5.4 and the processing time for two configurations on two meshes is depicted in Tab. 5.2.

5.3.2. Error analysis

In order to assess the consistency of our quadratic representation, we have estimated the error in simulation results using our method compared to the classical approach. Since our formulation uses only a linearised part of the fibre tension-strain rate relationship instead of the tri-linear equation, as described in Eq. (4.3), the error produced by this relaxation is also analysed. We performed different simulations using three configurations:

- the classical representation with the divisions of the interval $[-\pi/2, \pi/2]$ into 36 directions and the tri-linear fibre tension-strain rate relationship
- the classical representation with the divisions of the interval $[-\pi/2, \pi/2]$ into 36 directions and the linearised fibre tension-strain rate relationship
- our quadratic representation which was derived using the linearised fibre tension-strain rate relationship

The results using the first configuration are used as the reference values.

For the cell under bi-axial isometric tension, which is shown in Section 5.3.1, the zero strain rate leads to the same equations for all three configurations. Therefore, the solutions for the cell deformation and activation level are identical up to the machine precision (Fig. 5.5).

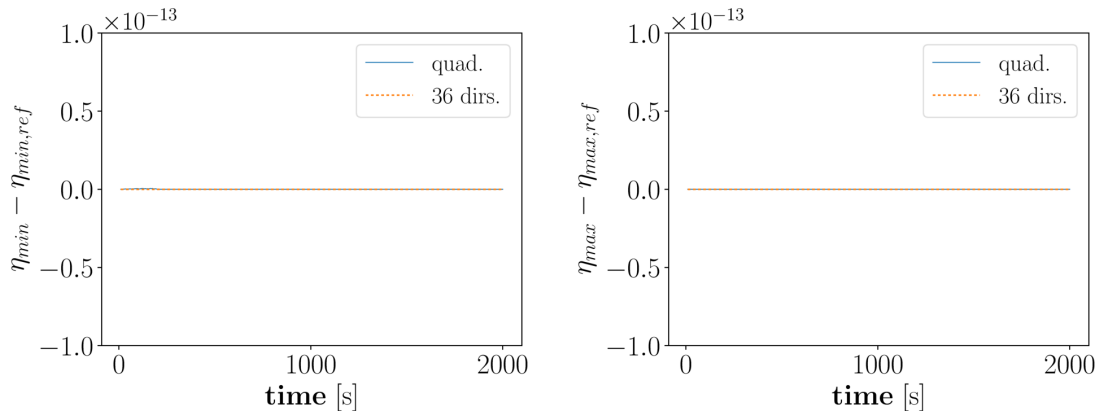


Figure 5.5: The plot for the differences in minimum and maximum activation level at any point in the cell.

For the case of non-homogeneous activation level in the cell, we investigate a square

5. Model order reduction of the bio-chemo-mechanical model

cell suspended by springs at four corners, which was demonstrated by Deshpande *et al.* [15]. Using the parameters in [15], we obtained similar results, where the average activation levels at four different periods of time are shown in Fig. 5.6. The values for

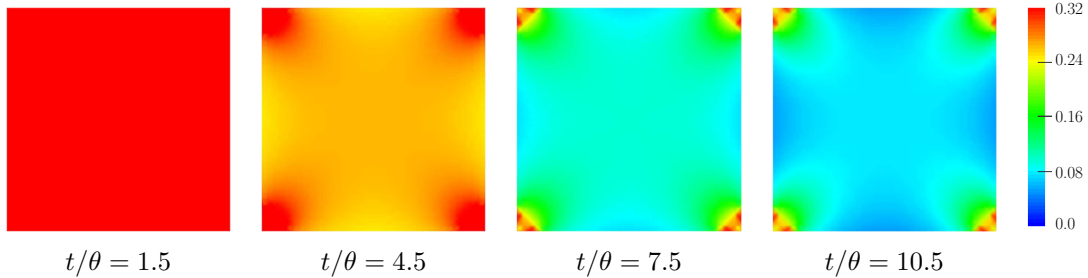


Figure 5.6: The distribution of average activation level at four selected times. FEniCS results using our quadratic representation.

active stress and the activation level are high at the corners, where the cell is connected to the springs.

Figure 5.7 shows the relative error in cell displacement at three points with different activation levels for using the linearised tension-strain rate relation compared to the reference configuration. It can be seen from the plot that there is almost no error between

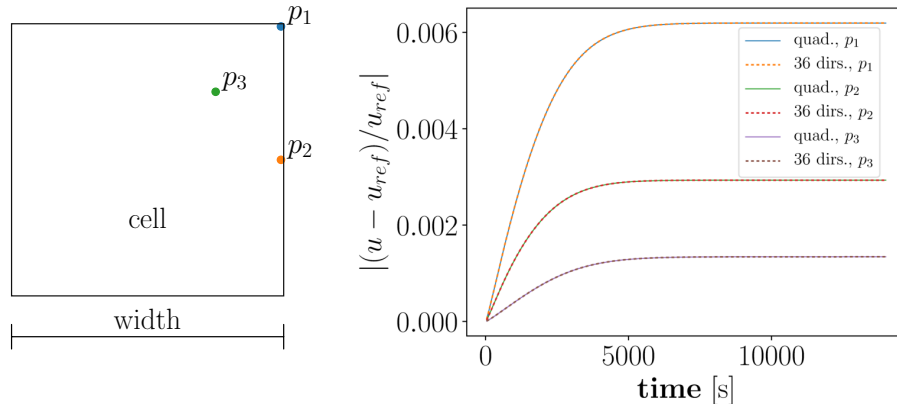


Figure 5.7: The three points of interest and the plot of relative error $|(u - u_{\text{ref}})/u_{\text{ref}}|$ in cell displacement.

using our quadratic representation and the classical representation. The error of using the linearised equation for tension-strain rate relationship is larger at the location where

5. Model order reduction of the bio-chemo-mechanical model

the activation level is higher. However, the relative error is around 0.006 and still in an acceptable range.

6. Numerical study on actin formation of osteoblasts on titanium arrays

This chapter closely follows our journal article [97].

Knowledge about the interaction between bone cells and their surrounding biomaterials is essential for the improvement in quality of an implant. Numerous experiments have been done to measure mechanical interaction between cells and the underlying substrates. Well-known methods include those introduced by Harris *et al.* [34], Burton *et al.* [11], Balaban *et al.* [4]. A more efficient method was introduced by Tan *et al.* [89], in which cells are laid on a bed of micro-needles so that forces exerted by cells can be measured from the individual displacements of the needles. This method was widely applied and adapted to achieve further understanding on behaviour of the cells. For example, Sniadecki *et al.* [84] used magnetic and non-magnetic posts to apply external forces and monitor traction forces. Matschegewski *et al.* [55] investigated the difference in actin concentration of bone cells when they are laid on either a planar surface or cubic pillar structures of different dimensions.

In this chapter, we aim to apply the bio-chemo-mechanical model to predict the tendency for the concentration of actin in osteoblasts observed in the experiments of Matschegewski *et al.* [55], where they were laid on arrays of regular titanium pillars. It is revealed from the experimental results that for osteoblasts actin was distributed in short fibres on the titanium pillar structure. While in the experiments of Tan *et al.* [89] for smooth muscle cells, actin was found as long fibres distributed intensely around the pillars. Therefore, simply applying the approach of McGarry *et al.* [57], which was applied for smooth muscle cells, will not be feasible. We will propose a set of parameters and a hypothesis for inhomogeneous adhesion and show that the bio-chemo-mechanical model can help predict the tendency of the osteoblast actin distribution.

6.1. Description for cell-pillar adhesion

It is revealed from the experiments of Matschegewski *et al.* [55] that cell adhesion was not uniform in the contact region between the cell and the pillars, and spot-adherence existed. To model this inhomogeneity of the adhesion, we use a scaling function $g(x, y)$, whose value is in the range $[0, 1]$, to represent the concentration level of the adhesion on a single pillar. The value 1 is assigned to the regions where spot-adherence occurs, while the zero value indicates the disappearance of the adhesion. The pillars are assumed to have square shape with blunt corners, which are close to those used in the experiments of Matschegewski *et al.* [55]. For simplicity and from the observation that spot-adherence

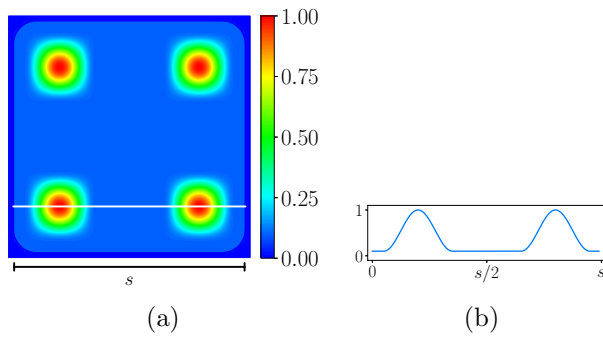


Figure 6.1: Plot of an exemplary function for the concentration level of the adhesion on a single pillar (left) and plot of a slice through two spots (right). Outside of the pillar, the function vanishes. Maximal function values are reached near the four corners of the pillar.

usually appeared near the periphery of the pillars, especially the corners, we constructed a smooth function that holds a small value everywhere except for the regions near the four corners of the pillar. The left part of Fig. 6.1 displays a possible choice for our function, while the right figure shows the 1D plot of a slice through two spots. With s being the side of the pillar and we denote:

$$f(x) = \frac{1}{2} \left(\cos \left(6\pi \frac{x - 0.5s}{0.9s} \right) + 1 \right) \in [0, 1], \text{ for } x \in [0, s], \quad (6.1)$$

the expression for the adhesion level that we used is:

$$g(x, y) = \begin{cases} 0.9 * f(x) * f(y) + 0.1, & \text{if } |x - 0.5s|, |y - 0.5s| \in [0.15s, 0.45s] \\ 0.1, & \text{otherwise} \end{cases} \quad (6.2)$$

6. Numerical study on actin formation of osteoblasts on titanium arrays

for $(x, y) \in [0, s] \times [0, s]$ representing a point on the pillar structure. The values of the function g are in the range $[0.1, 1]$. This is equivalent to the assumption that the adhesion at the peak points is ten times stronger than that at those points where the strength of adhesion is lowest. When desired, the function can easily be adjusted to meet other assumptions. The simple adhesion model in [57] is then modified so that the traction in the cell at the contact region becomes

$$T_i = g(x, y) \cdot k_t \cdot \Delta_i, \quad (6.3)$$

where k_t is the shear stiffness constant of the adhesion, when the cell moves a distance Δ_i from the pillar.

6.2. Results and discussion

We apply the bio-chemo-mechanical model together with our suggested model for the adhesion of the cell to the pillar structure to simulate the actin distribution of osteoblasts on titanium arrays of different dimensions. The parameters for the bio-chemo-mechanical model, the material properties of the pillars as well as the passive mechanical material

Parameter	Value	Description
σ_{\max}	$0.15[\text{nN}/\mu\text{m}^2]$	maximum fibre tension
θ	$70 [\text{s}]$	decay constant of signal
\bar{k}_v	7	tension reduction coefficient with respect to strain rate
\bar{k}_f	10	formation rate constant
\bar{k}_b	1	dissociation rate constant
$\dot{\varepsilon}_0$	$10^{-5} [\text{s}^{-1}]$	initial fibre contraction rate
k_t	$500[\text{nN}/\mu\text{m}^3]$	focal adhesion stiffness
E_{cell}	$0.4[\text{nN}/\mu\text{m}^2]$	Young's modulus of the cells
ν_{cell}	0.3	Poisson's ratio of the cells
E_{pillar}	$1.0 \cdot 10^3[\text{nN}/\mu\text{m}^2]$	Young's modulus of the pillars
ν_{pillar}	0.35	Poisson's ratio of the pillars

Table 6.1: Parameters for the BCM model, material properties of the pillars and passive mechanical material properties of the cell.

6. Numerical study on actin formation of osteoblasts on titanium arrays

properties of the cell are shown in Table 6.1. The values for θ , \bar{k}_f , \bar{k}_b and \bar{k}_v are the same as those in [57]. From experimental observation we know that osteoblasts generate a very small contraction force. Thus, the values that we used for σ_{\max} and $\dot{\varepsilon}_0$ are $0.15[\text{nN}/\mu\text{m}^2]$ and $10^{-5}[\text{s}^{-1}]$, respectively, which are much smaller than the values in [57]. At the regions where the cell is in contact with the pillars, the value $k_t = 500\text{nN}/\mu\text{m}^3$ is used for the focal adhesion stiffness, which is also the same as that in [57] and Eq. (6.3) is used for the shear traction.

The system of governing equations, which includes the equilibrium condition and Eq. (4.2), is solved using finite element analysis. Since almost no deflection of the pillars was found in the experiments, the usual approach is considering the pillars as rigid bodies and applying a homogeneous Dirichlet boundary condition. Here, we used the approach in [57] and modelled the pillars as rounded rectangular surfaces connected to springs of a large stiffness. This relaxation allows the stability of the solution procedure, while the obtained displacement of the pillars is small enough to be ignored. The linear elastic material model is used for both the cell and the pillars.

We used the *gmsh* generator [28] to create the meshes and the open source framework *FEniCS*, version 2016.2 [53] to compute the solution. For time discretisation, we used an explicit method with a maximum time step of 2 seconds and performed a convergence study to make sure that the solution is stable with our choice of time step.

To demonstrate the applicability of our model using an inhomogeneous adhesion function, we carried out the simulations for osteoblasts on arrays of square pillars of different sizes: $5\mu\text{m} \times 5\mu\text{m}$ and $3\mu\text{m} \times 3\mu\text{m}$. For simplicity, we used the same function $g(x, y)$ (Eq. (6.2)) for the adhesion at all pillars.

6.2.1. Osteoblast on arrays of titanium coated pillars of $5\mu\text{m} \times 5\mu\text{m}$

We first apply the model to a cell patch on 26 pillars in our experiment, as shown in Fig. 6.2a. We constructed a cell geometry with the assumption that the initial cell has straight edges between pillars and it fits perfectly to the 26-pillar sub-array depicted in Fig. 6.2b. Moreover, we also assume that the pillars are of perfect square shape with blunt corners. The side length of the pillars is $5\mu\text{m}$, while the radius of the corner fillet is $0.5\mu\text{m}$ (area $\approx 24.77\mu\text{m}^2$). The distance between two neighbouring pillars is also $5\mu\text{m}$. The stiffness of the springs connected to the surfaces representing the pillars is $7.5\text{nN}/\mu\text{m}$.

The simulation result for actin formation is shown in Fig. 6.2c. It can be seen that the

6. Numerical study on actin formation of osteoblasts on titanium arrays

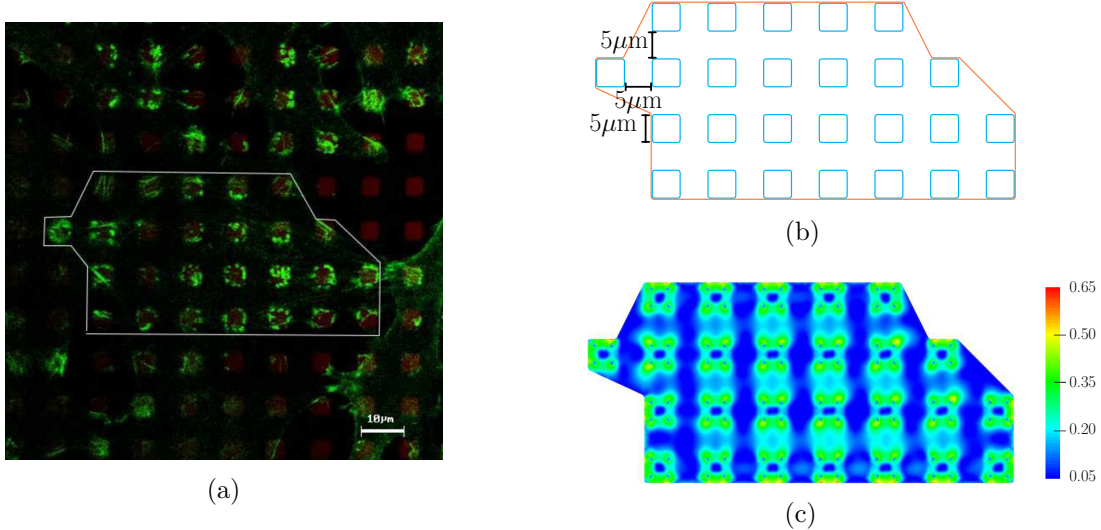


Figure 6.2: (a) Fluorescence image of the actin filament distribution in MG-63 osteoblasts (actin in green, LSM 780, bar $10\mu\text{m}$; with courtesy of H. Rebl and R. Lange). The white line demonstrates a simplified form of one cell. (b) Sketch of the patch of a cell used in the simulation. (c) Our predicted result for actin distribution (characterised by the measure Π) using the bio-chemo-mechanical model and our description for the cell-pillar adhesion.

highest amount of actin is on the pillars and it is distributed non-uniformly. Moreover, at the longest edges of the cell, there is more actin than at other edges. The obtained maximum displacement of the pillars is around 7nm, which is 0.14% of the side length of the pillar. Analogous outcome is achieved when we apply the model for an osteoblast on an array of 19 pillars, which is illustrated in Fig. 6.3.

It should be noted that without our adaptation of the model for the adhesion of muscle cells to the adhesion of osteoblasts involving an inhomogeneous adhesion behaviour, the result would not agree with the experiment, as the predicted actin would form around the pillars and there would be a uniform low level of actin on the pillars. To further improve the agreement between the results using our approach, the complexity of the model should be increased: a more complex function $g(x, y)$ should be constructed and the function could also be different for each pillar.

6. Numerical study on actin formation of osteoblasts on titanium arrays

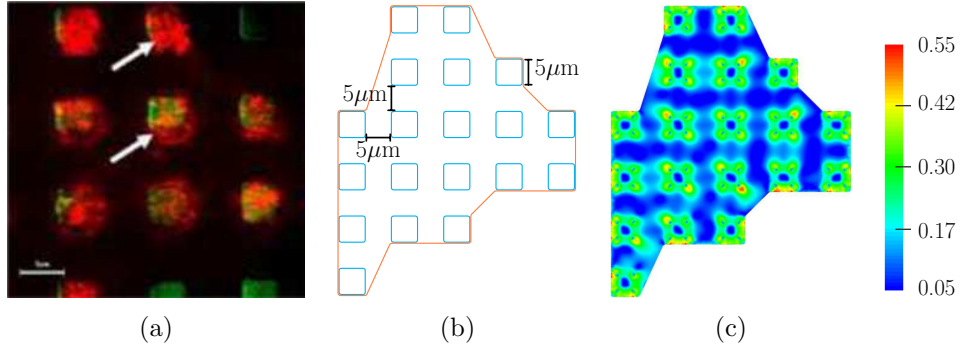


Figure 6.3: (a) Experimental result for the actin distribution of a MG-63 osteoblast on a $5\mu\text{m} \times 5\mu\text{m}$ pillar array by Matschegewski *et al.* [55], (b) sketch of the cell used in the simulation and (c) our predicted actin distribution (characterised by the measure Π in Eq. (4.13)) for this cell.

6.2.2. Osteoblast on array of titanium coated pillars of $3\mu\text{m} \times 3\mu\text{m}$

Similar steps are applied for the simulation of osteoblast on an array of 25 pillars of dimension $3\mu\text{m} \times 3\mu\text{m}$. The radius for the rounded corners is chosen to be $0.4\mu\text{m}$ and the distance between two neighbouring pillars is $3\mu\text{m}$, as in the experiment in [55]. As the area of the pillar is around $8.85\mu\text{m}^2$, which is smaller than that in the previous example, the corresponding spring stiffness is set to $2.68\text{nN}/\mu\text{m}$.

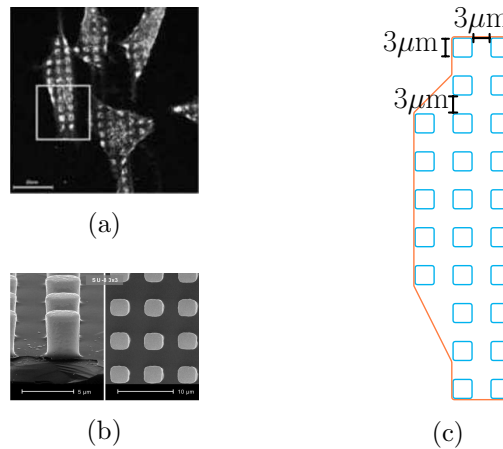


Figure 6.4: (a) Experimental result for the actin distribution of a MG-63 osteoblast on a $3\mu\text{m} \times 3\mu\text{m}$ pillar array by Matschegewski *et al.* [55], (b) dimensions of the pillars and (c) sketch of the cell used in the simulation.

The predicted actin distribution is shown in Figure 6.5. As in the previous case, the

6. Numerical study on actin formation of osteoblasts on titanium arrays

highest concentration of actin is located on the pillars. Since the distance between the pillars is small, a relatively high level of actin can also be found in the parts of the cell connecting the pillars. In the experiment, at some regions, the actin concentration in those parts is similar to that on the pillars.

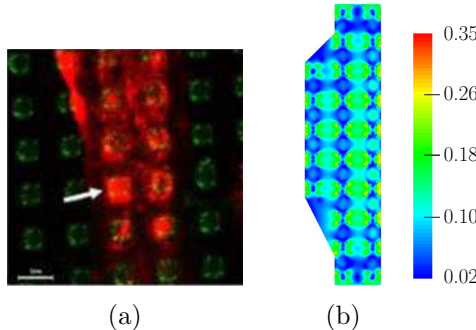


Figure 6.5: (a) Actin formation of osteoblasts as described by Matschegewski *et al.* [55] and (b) our simulation result for MG-63 osteoblasts on $3\mu\text{m} \times 3\mu\text{m}$ pillar structures. The predicted actin distribution is characterised by the Π measure in Eq. (4.13).

6.2.3. Effect of the adhesion scaling function

To study numerically the dependency of actin patterns on the adhesion between the cell and the pillars, we constructed different configurations for our adhesion scaling function.

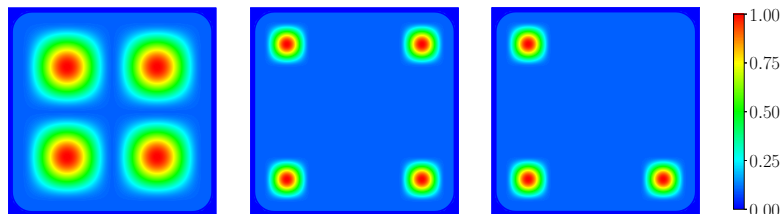


Figure 6.6: Different adhesion scaling functions for a single pillar. In the left figure, the strongest adhesions locate at four spots with a large area distributed uniformly on the pillar. In the middle and right figures, peak adhesions are at four and three spots, respectively, with a small area distributed near the corners of each pillar. The definition of these functions are provided in Tab. 6.2.

6. Numerical study on actin formation of osteoblasts on titanium arrays

We varied the location and the area of strong adhesion near the peak points. We also used different number of peak points on each pillar. Examples of our adhesion scaling functions defined on a single pillar are shown in Fig. 6.6.

$f_1(x) = \frac{1}{2} \left(\cos \left(4\pi \frac{x - 0.5s - 0.225s}{0.9s} \right) + 1 \right) \in [0, 1], \text{ for } x \in [0, s],$
$g_1(x, y) = \begin{cases} 0.9 * f_1(x) * f_1(y) + 0.1, & \text{if } x - 0.5s \leq 0.45s \text{ and } y - 0.5s \leq 0.45s \\ 0.1, & \text{otherwise} \end{cases}$
$f_2(x) = \frac{1}{2} \left(\cos \left(8\pi \frac{x - 0.5s - 0.3375s}{0.9s} \right) + 1 \right) \in [0, 1], \text{ for } x \in [0, s],$
$g_2(x, y) = \begin{cases} 0.9 * f_2(x) * f_2(y) + 0.1, & \text{if } x - 0.5s , y - 0.5s \in [0.225s, 0.45s] \\ 0.1, & \text{otherwise} \end{cases}$
$f_3(x) = \frac{1}{2} \left(\cos \left(8\pi \frac{x - 0.5s - 0.3375s}{0.9s} \right) + 1 \right) \in [0, 1], \text{ for } x \in [0, s],$
$g_3(x, y) = \begin{cases} 0.9 * f_3(x) * f_3(y) + 0.1, & \text{if } x - 0.5s , y - 0.5s \in [0.225s, 0.45s] \\ & \text{and } (x < 0.5s \text{ or } y < 0.5s) \\ 0.1, & \text{otherwise} \end{cases}$

Table 6.2: Three different scaling functions for the adhesion on a single pillar. Here, s is the side length of the square pillar and a point on the pillar is represented by $(x, y) \in [0, s] \times [0, s]$.

Using these scaling functions for the adhesion, we performed the analysis for the actin distribution of an osteoblast on an array of 19 pillars of $5\mu\text{m} \times 5\mu\text{m} \times 5\mu\text{m}$. It can be seen from the analysis results, which are shown in Fig. 6.3 and Fig. 6.7, that changing the size of the peak adherence does not affect much the trend of the actin formation on the pillars. However, the small area of these peak points gives a more smooth actin distribution. Modifying the number of peak points could deliver a different pattern of actin on the pillars, where the amount of actin is affected. This result supports our suggestion that using different scaling functions for different pillars could give a better agreement between simulation and experimental results.

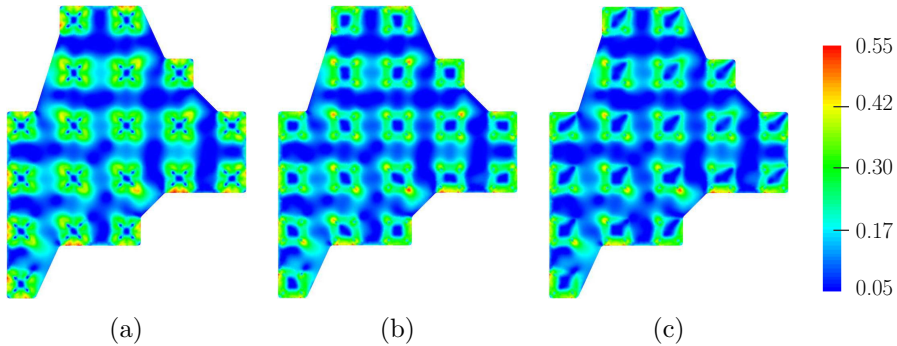


Figure 6.7: Predicted results for actin distribution of an osteoblast on an array of 19 pillars using different adhesion scaling functions. Each function is applied for all 19 pillars in every simulation.

6.3. Conclusion

The bio-chemo-mechanical model proposed by Deshpande *et al.* has the capability to simulate the contractility and actin formation of biological cells when they are laid on different kinds of substrate. Using this model and a simple model for the adhesion between cell and substrate, McGarry *et al.* [57] successfully simulated the actin distribution in smooth muscle cells and fibroblasts on arrays of polydimethylsiloxane posts. Direct application of the approach of McGarry *et al.* to the experiments with osteoblasts on titanium pillar arrays of Matschegewski *et al.* [55] would lead to a great disagreement between experimental and simulated results. We suggested a mathematical model for inhomogeneous adhesion and constructed a function that represents the different concentrations of adhesion at different regions on a pillar. We demonstrated our approach by applying it to our experiments and to experimental results by Matschegewski *et al.* [55]. Using our model, the predicted actin distribution agrees better to the experimental results than with other existing models. Our finding reconfirms a feature of the bio-chemo-mechanical model that it is able to capture the strong influence of the boundary condition on the formation of actin within the cells.

7. Contractility of fibroblasts and osteoblasts under DC electric field

This chapter closely follows a paper draft intended to be published with the title “Modelling effects of DC electric field on contractility and cytoskeleton of fibroblasts and osteoblast-like cells using a bio-chemo-mechanical model” [98].

It is significant to understand and utilise different biophysical and biochemical stimuli to improve the quality of engineered tissue implants. Electrical stimulation is important in the physiology and development of the majority of all human tissues and is a potential type of stimulus for further improvement of implants [5].

Numerous observations on the responses of various cells to direct-current (DC) electric field have been obtained through experimental methods [14, 36, 69]. In the work of Harris *et al.* [36], a DC electric field of 1V/mm was applied to embryonic chick fibroblasts on silicone rubber substrata and the contractility and cytoskeleton of the cells were investigated. Several interesting results were found, where there are some remarkable effects of the electric field on fibroblast contractility and actin orientation. First, the cell was found to retract in the axis parallel to the electric field and the cell contractility was found to be weaker in this direction. After that, the alignment and the elongation of the cells and a higher contractility were observed in the direction perpendicular to the electric field. Those responses of fibroblasts were not different for three different substratum materials: silicone rubber sheets, glass and polystyrene. In case of silicone rubber, the changes in the patterns of wrinkling in the substrate were found: the wrinkles that run transversely to the voltage gradient disappeared progressively, while new wrinkles that run in the parallel direction were formed. These changes indicate that the concentration of the cellular traction forces became dominant in the direction perpendicular to the electric field.

Using similar approaches, Curtze *et al.* [14] observed that osteoblast-like cells delivered analogous behaviours when they are exposed to a DC electric field, but the process

7. Contractility of fibroblasts and osteoblasts under DC electric field

happened in a different time scale. In addition to that, the changes in cytoskeletal contraction were obtained by culturing the cells on collagen-coated flexible polyacrylamide sheets containing fluorescent marker beads and analysing the traction forces based on the obtained images.

The underlying mechanisms of the migration and orientation are still poorly understood. Harris *et al.* [36] suggested three possible mechanistic causes for morphological reorientation: (i) the electric field could stimulate the protrusion in the direction perpendicular to the voltage gradient, or (ii) the contraction in the direction parallel to the field, and / or (iii) weaken the adhesions between the cells and the substrate at those parts of the cells that face the field.

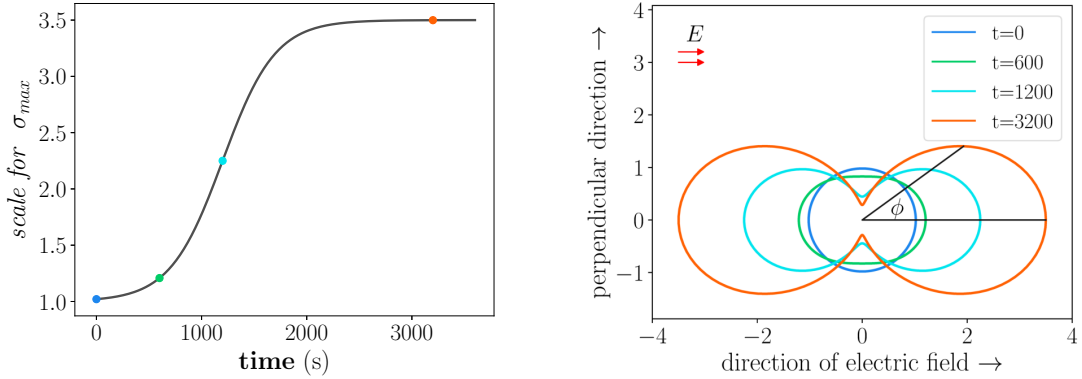
Several numerical models have been proposed to describe the cell contractility and the interaction between cells and substrate. The bio-chemo-mechanical model proposed by Deshpande *et al.* [15] takes into account the dynamic reorganisation of the cytoskeleton and has many advantages compared to other models [15]. In this chapter, we will supply this model with a description for the effects of DC electric field to study numerically the contractility and cytoskeleton of fibroblasts and osteoblast-like cells under electric field exposure.

7.1. Modelling the effects of DC electric field

Stimulation of contraction in the direction of the electric field To address the influence of the DC electric field to the contraction of the cells, we suggest a change of the two constants, the maximum fibre tension σ_{\max} and the initial shortening rate $\dot{\varepsilon}_0$, so that they become dependent on the directions of the fibres and on time. The argument for the choice of these parameters is that they significantly determine the magnitude and the speed of cell contraction. Note that the modification of $\dot{\varepsilon}_0$ is equivalent to that of the constant \bar{k}_v relating the tension and the shortening rate of the fibres. Alternatively, the other parameters such as the controlling constants for the formation and dissociation rates can also be modified, but we observed that the two parameters we chose are most significant.

Our suggestion for addressing the effects of the DC electric field is that the parameters σ_{\max} and $\dot{\varepsilon}_0$ should be larger in the direction parallel to the electric field and smaller in the perpendicular direction. To formulate this, we introduce a scaling function $s(t) \geq 1$ and assume that at time t , the two parameters σ_{\max} and $\dot{\varepsilon}_0$ increase $s(t)$ times in the

7. Contractility of fibroblasts and osteoblasts under DC electric field



(a) A proposed scaling function for the maximum active tension in the direction of electric field.

(b) The scaling for the maximum active tension in different directions at four periods of time.

Figure 7.1: (a) A possible scaling function to represent the raise of the maximum tension in the direction parallel to the electric field and (b) a possible function to represent stimulation of the active stress in different directions at four time periods.

parallel direction and decrease $s(t)$ times in the perpendicular direction. As the electric field gradually affects the cells within a period of time, the function $s(t)$ should increase slowly in a time interval before it reaches a maximum value. For example, to express the idea that the maximum fibre tension can rise up to 3.5 times in the direction of the electric field and in around 40 minutes, we use the function $s(t) \in [1, 3.5]$ as follows:

$$s(t) = \frac{5}{2} \left(\frac{1}{2} - \frac{1}{2} \tanh \left(\frac{t - 1200}{500} \right) \right) + 1 \quad (7.1)$$

The plot of this function is shown in Fig. 7.1a. Compared to the case where the electric field is absent, at the time t , the maximum fibre tension is scaled by $s(t)$ in the direction of the electric field and by $1/s(t)$ in the perpendicular direction. We further assume that the scaling factor for the maximum tension in the direction that makes an angle ϕ to the electric field is given by:

$$s(\phi, t) = s(t) \cos^2 \phi + (1/s(t)) \sin^2 \phi \quad (7.2)$$

The plot of this scaling function at four periods of time is shown in Fig. 7.1b. Here we would like to note that ideally these functions should include dependency on the cell types and the magnitudes of the electric field. In this work, we slightly modify the

7. Contractility of fibroblasts and osteoblasts under DC electric field

functions for each simulation, but later when there are sufficient experimental data, they can be easily parametrised.

Decrease in cell-substrate adhesion at the regions facing the electrodes To model the reduction in the strength of the adhesions between the cells and their substrate in the regions of the cells facing the electrodes, we introduce a scaling function for the adhesion shear stiffness k_t in Eq. (4.12). This function is defined so that for every line parallel to the electric field cutting the cell, the function value should hold the value 1 at the middle of the line and decrease at the two ends. An example for this function

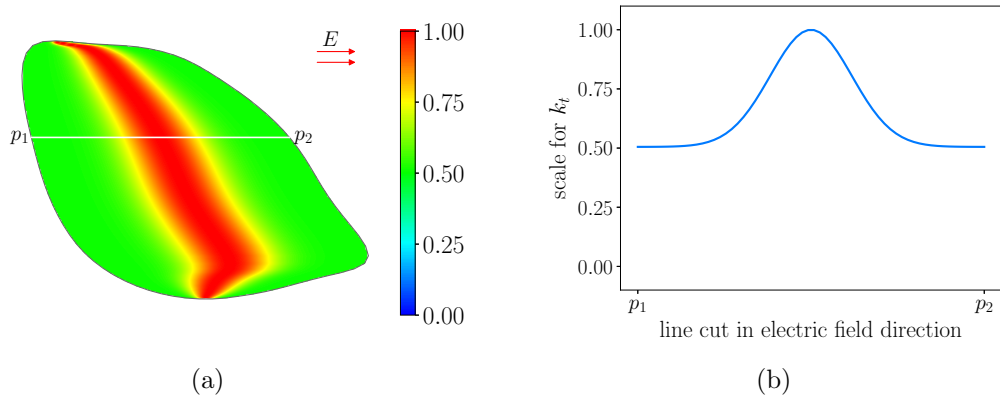


Figure 7.2: (a) A function for the scaling of the adhesion between the cell and the substrate when assuming that under the electric field, the strength of the adhesion is reduced two times at the cell peripheries facing the electrodes. (b) Plot for the scaling function on a line through the cell and parallel to the electric field.

is illustrated in Fig. 7.2, where it is assumed that the adhesion at the cell peripheries facing the electrodes are two times weaker than in the middle part of the cell. Let p_1 and p_2 be the intersecting points between the cell and a line parallel to the electric field, the function on the line segment between p_1 and p_2 is defined as follows:

$$g(d) = \frac{1}{2} \exp \left[- \left(\frac{6d}{L} \right)^2 \right] + \frac{1}{2} \quad (7.3)$$

where d is the distance to the middle point and L is the length of the line segment. Thus, given a scaling value at the cell peripheries facing the electrodes, the value of the scaling function $g(x, y)$ is determined for every point (x, y) in the cell.

7.2. Results

We used the *mshr* library [2] to create the meshes and the open source framework *FEniCS*, version 2016.2 [53] to compute the solution. For time discretisation, we used an explicit method with a maximum time step of 2 seconds and performed a convergence study to make sure that the solution is stable with our choice of time step.

7.2.1. Magnitude of the Maxwell stress tensor

We examine the total electromagnetic force on the cell by computing the value of the Maxwell stress tensor. Suppose a cell of a typical size is suspended in a culture medium and is exposed to a DC electric field of strength 1V/mm (Fig. 7.3a). The distribution

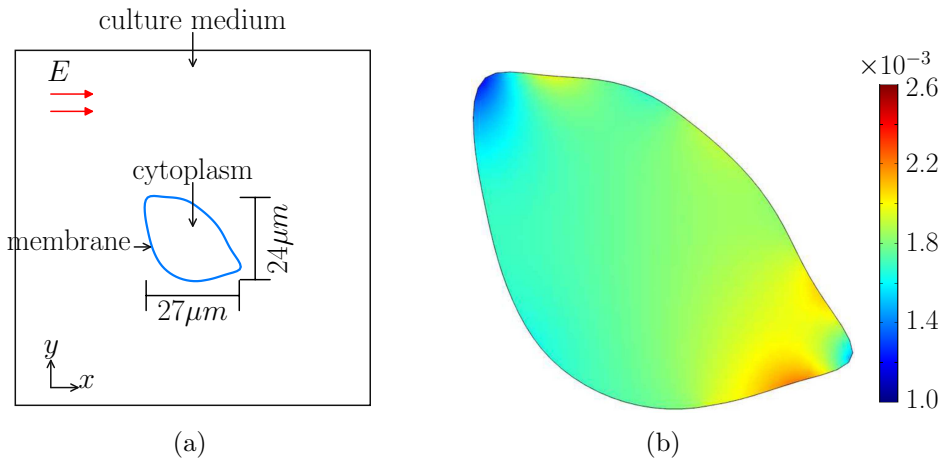


Figure 7.3: (a) Sketch of a typical cell under a DC electric field exposure and (b) plot of electric field magnitude (V/mm) in the cell. The applied field is in horizontal direction and with a strength of 1V/mm. The parameters in Tab. 7.1 are used for the electrical properties of the cell membrane, cell cytoplasm and the culture medium. The computation is done using the software COMSOL MULTIPHYSICS®.

of the electric field in the cell can be obtained by solving Eq. (2.40). The plot of the electric field distribution is shown in Fig. 7.3b, where the values in Tab. 7.1 are used for the electrical properties of cell cytoplasm, membrane and the culture medium.

Then, the Maxwell stress tensor can be computed from the electric field using Eq. (2.41). The plot of the components of the Maxwell stress is shown in Fig. 7.4. We can see that the highest value of the Maxwell stress in the cell is around $2 \cdot 10^{-10}$ Pa. This value is too

7. Contractility of fibroblasts and osteoblasts under DC electric field

Parameter	value
Cytoplasmic conductivity	$\sigma_{\text{cyto}} = 1.5 \text{ [S/m]}$
Cytoplasmic relative permittivity	$\epsilon_{\text{cyto}} = 80$
Membrane conductivity	$\sigma_{\text{mem}} = 5 \cdot 10^{-7} \text{ [S/m]}$
Membrane relative permittivity	$\epsilon_{\text{mem}} = 11.3$
Culture medium conductivity	$\sigma_{\text{medium}} = 1.5 \text{ [S/m]}$
Culture medium relative permittivity	$\epsilon_{\text{medium}} = 80$
Membrane thickness	$d = 5 \text{ nm}$

Table 7.1: Electrical properties of the cell membrane, cell cytoplasm and the culture medium. The values are taken from [58] and [88].

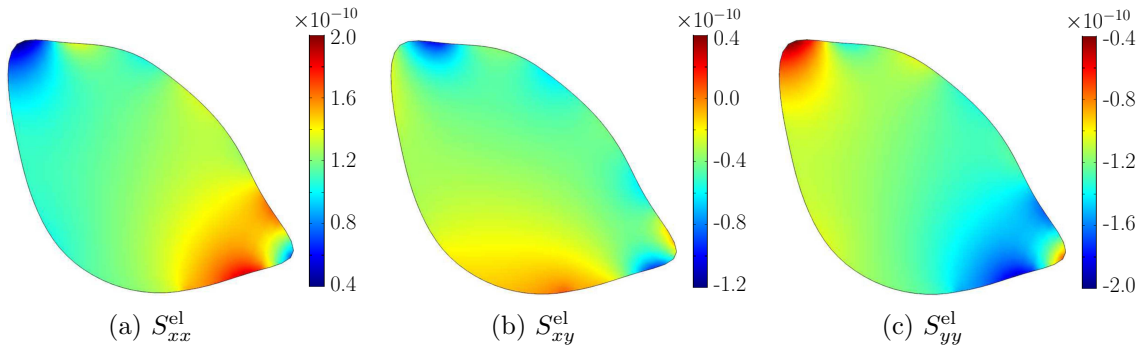


Figure 7.4: Plot of the components of the Maxwell stress tensor \mathbf{S}^{el} (in Pa). The computation is done using the software COMSOL MULTIPHYSICS®.

small compared to the active stress in the bio-chemo-mechanical model, which is usually in the range 0.2 – 25kPa. Therefore, we will ignore the contribution of the Maxwell stress in our simulations.

7.2.2. Fibroblast contractility and cytoskeleton

We first apply the bio-chemo-mechanical model together with our description for the effects of DC electric field for the simulation of the contractility and actin formation in fibroblasts observed in the experiments of Harris *et al.* [36]. A fibroblast cell of typical dimension is used in our simulation. The shape of the cell is constructed based on an image from the experiments of Harris *et al.* [36] and is shown in Fig. 7.5. A DC electric field of 1V/mm is applied in the vertical direction, as in [36].

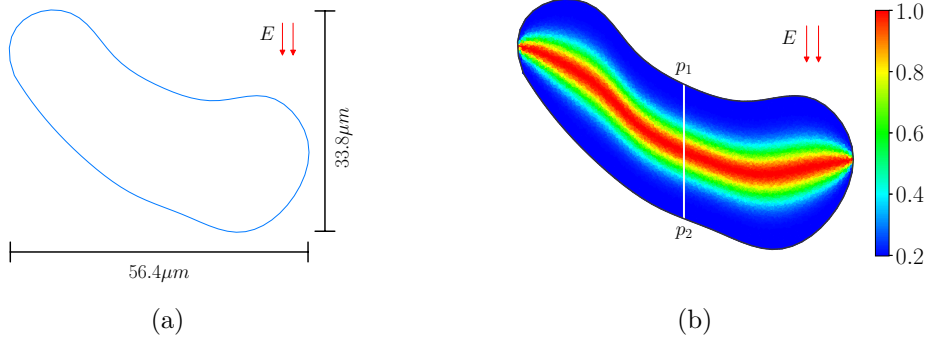


Figure 7.5: Shape and size of a fibroblast cell used in our simulation and the scaling function for the adhesion.

The parameters for the bio-chemo-mechanical model and the mechanical material properties of the cell are shown in Tab. 7.2. The value for the decay constant θ is

Parameter	σ_{\max}	θ	\bar{k}_v	\bar{k}_f	\bar{k}_b	$\dot{\varepsilon}_0$	E_{cell}	ν_{cell}
Unit	[nN/μm ²]	[s]				[s ⁻¹]	[nN/μm ²]	
Value	3.25	720	7	10	1	0.003	0.4	0.3

Table 7.2: Parameters for the BCM model and cell material properties that are used for fibroblasts.

720s, as in [15], while other parameters are the same as those in [57]. For the substrate, we used the value 0.4 for the Poisson's ratio. As the Young's modulus is not given in [36], we used the value of 6nN/μm², which is close to the values described in [14], and observed that changing this value by 30% does not affect the results significantly. For the contact between the cell and the substrate, we also use the same value as in [57], which is $k_t = 500$ nN/μm³, for the shear stiffness of the adhesion.

With these parameters used, we suppose that under the electric field, the value of σ_{\max} rises up to 2.5 times in around 50 minutes after the start of applying the electric field. In other words, the following scaling function (as in Eq. (7.1)) is used for fibroblasts with the field strength of 1V/mm and the given set of parameters:

$$s(t) = \frac{3}{2} \left(\frac{1}{2} + \frac{1}{2} \tanh \left(\frac{t - 1600}{400} \right) \right) + 1 \quad (7.4)$$

In addition to that, it is assumed that the strength of the adhesion at the cell margins

7. Contractility of fibroblasts and osteoblasts under DC electric field

facing the electrodes decreases to 10% of the initial value. This means that the equation (7.3) for fibroblasts is modified to:

$$g(d) = \frac{9}{10} \exp \left[- \left(\frac{6d}{L} \right)^2 \right] + \frac{1}{10} \quad (7.5)$$

The scaling function for the adhesion is shown in Fig. 7.5b.

Our simulation results for the changes over time of the bounding box of the cell in the parallel and perpendicular directions are shown in Fig. 7.6. It can be clearly seen that with the introduction of our scaling function for the active stress, the cell retracts in around 20 minutes then it elongates perpendicular to the electric field. In the model,

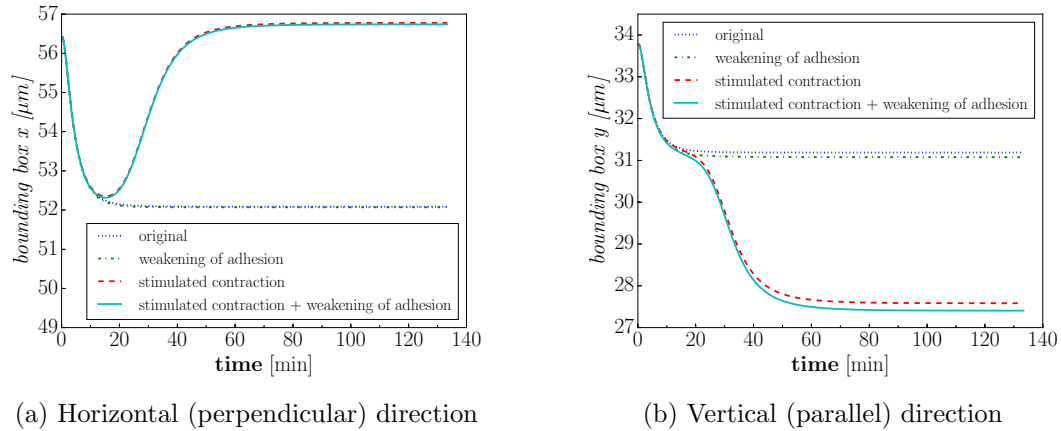


Figure 7.6: Change of the bounding box of a fibroblast cell over time.

the weakening of the adhesion at the margins facing the electrodes can indeed predict the increase of the cell contraction in the direction parallel to the field. However, the effect is very small and without the modification of the active stress, a large retraction in the parallel direction and the elongation of the cell in the perpendicular direction cannot be obtained. Using a very small value for the strength of the adhesion at the cell margins facing the electrodes would allow a higher contraction of the cell in the electric field direction, but the adhesion would not be realistic as a major part of the cell would be no longer in contact with the substrate.

7.2.3. Dynamic changes in traction forces by osteoblasts under DC electric field exposure

We then apply the model to simulate the response of osteoblast-like cells observed in the experiments of Curtze *et al.* [14]. The parameters in Tab. 7.3 are used. As osteoblasts

Parameter	σ_{\max}	θ	\bar{k}_v	\bar{k}_f	\bar{k}_b	$\dot{\varepsilon}_0$	E_{cell}	ν_{cell}
Unit	[nN/ μm^2]	[s]				[s^{-1}]	[nN/ μm^2]	
Value	0.2	720	7	10	1	0.0004	0.4	0.3

Table 7.3: Parameters for the BCM model and cell material properties that are used for osteoblast-like cells.

generate very small contraction in absence of an electric field, the values used for σ_{\max} and $\dot{\varepsilon}_0$ are smaller compared to those for fibroblasts. The value $k_t = 500\text{nN}/\mu\text{m}^3$ is again used for the shear stiffness of the adhesion.

Since the contraction of the cells is reported to be high under the electric field exposure, we suggest that the value of σ_{\max} rises up to 9 times in around 20 minutes after the start of applying the electric field. In other words, the following scaling function (as in Eq. (7.1)) is used for osteoblasts with the field strength of 1V/mm and the given set of parameters:

$$s(t) = 8 \left(\frac{1}{2} + \frac{1}{2} \tanh \left(\frac{t - 600}{200} \right) \right) + 1 \quad (7.6)$$

For the weakening of the adhesion at the cell margins facing the electrodes, we use the same scaling function as for fibroblasts, which is provided in Eq. (7.5).

The simulation is done first for an osteoblast cell of around 27 μm width and 24 μm height. The geometry of the cell is constructed from an image provided in [14] (Fig. 7.7a). In this simulation, the value $E_{\text{sub}} = 4.32\text{nN}/\mu\text{m}^2$ is used for the Young's modulus of the substrate, which is the same as in the experiment in [14].

We used different values for the initial maximum fibre active tension σ_{\max} while other parameters in Tab. 7.3 remain unchanged and observed the change of the bounding box of the cell over time. Figure 7.8 shows our simulation results for the change of the bounding box of the cell in the parallel and perpendicular directions together with the experimental results by Curtze *et al.* [14]. It can be seen that with the value $\sigma_{\max} = 2.0$, the change of the bounding box in the parallel direction agrees very well

7. Contractility of fibroblasts and osteoblasts under DC electric field

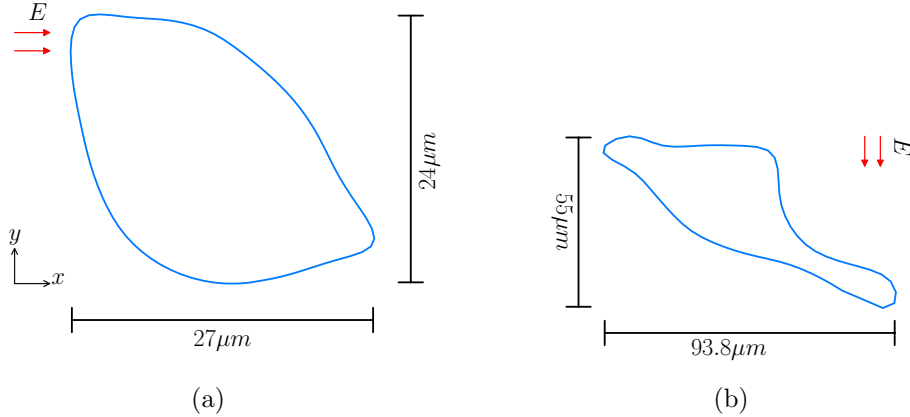


Figure 7.7: Cell geometries and the direction of DC electric field. Two osteoblast-like cells of different shape are investigated in our simulation. The geometries are constructed based on the images in Fig. 1 and Fig. 7 in [14]. The electric field is in the horizontal direction and of strength 10V/cm.

with the experiment. In the perpendicular direction, the simulation can predict the trend that there is a contraction in the first 20 minutes then the cell starts to elongate. However, the magnitudes of the contraction and the elongation are smaller by a factor of about 2 compared to the experiment and the cell cannot reach its initial size. The smaller values of σ_{\max} (e. g. $\sigma_{\max} = 0.2$ and $\sigma_{\max} = 0.8$) can better predict the elongation, but again the magnitudes are not in agreement with the experimental results, especially in the parallel direction. In this case, an improvement in the results can be obtained by using a smaller value for the adhesion at the margins of the cell facing the electrodes. However, as we already pointed out in the case of fibroblasts, this adhesion is not realistic and can lead to the instability of the cell structure.

The simulation is repeated for another geometry of the cell, which is also constructed based on an image from [14] and is shown in Fig. 7.7b. The value for the substrate stiffness is changed to $6\text{nN}/\mu\text{m}^2$ as in the experiment, while other parameters are not modified. Figure 7.9 shows the differential substrate displacement vectors at the cell boundary for six periods of time. To obtain these results, we first computed the deformation of the substrate using the parameters in Tab. 7.3 together with our description for the effects of the electric field. Then, the displacement of the substrate in absence of the electric field was calculated. In this case, again the parameters in Tab. 7.3 were applied, but the value $\dot{\varepsilon}_0 = 0.0002[1/s]$ was used for the initial strain rate, as the contractility in osteoblasts is usually weak without electrical stimulation. Finally, the differences

7. Contractility of fibroblasts and osteoblasts under DC electric field

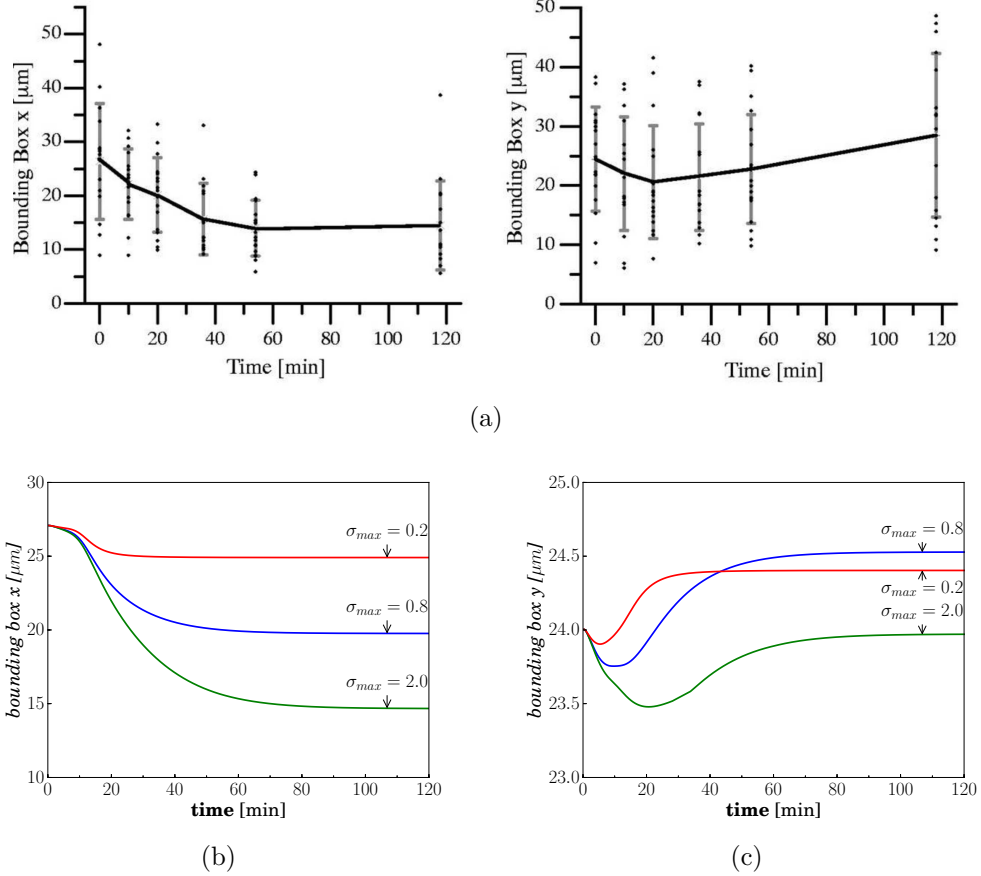


Figure 7.8: (a) The change over time of the bounding box around every cell in the direction along parallel and perpendicular to the electric field (Figure from [14]). The strength of the field is 10V/cm. (b, c) Our simulation results.

in the substrate displacement were obtained for two cases. In a short period of time, the change in the displacement of the substrate is linearly related to the change of the traction forces by the cell. Therefore, these results give some insights on the differential traction forces during cellular alignment, which are obtained by Curtze *et al.* [14] by solving an inverse problem. The trend of the displacement changes is in good agreement with the traction force change in the experiment in [14] at many regions and periods of time. However, in Fig. 7.9e and 7.9f, the highest values of the displacement changes are at the peripheries facing the electrodes, which is not the case in the experiment. Our explanation for this disagreement is that the strength of the adhesion at those regions should be weaker than our suggested value. Again this reconfirms the remaining weak points of the simple adhesion model that is used in our simulation. To improve the results, it is necessary to build a more efficient description for the adhesion. Neverthe-

less, by explaining several effects found in the existing experiments, our mathematical description based on the bio-chemo-mechanical model support the hypothesis by Harris *et al.* [36] that the cell contraction is promoted in the direction of the electric field and the adhesion is weakened at the regions facing the electrodes.

7.3. Conclusion

We enhanced the bio-chemo-mechanical model [15] with our description for the effects of the DC electric field based on the proposed mechanisms of Harris *et al.* [36]. We then applied this extended model for the simulation of the experiments on fibroblasts by Harris *et al.* [36] and osteoblasts by Curtze *et al.* [14]. Our conclusions can be summarised as follow:

- The bio-chemo-mechanical model is very efficient in simulating the dynamics of actin formation in cells of different types, as it addresses the bio-chemical process. Together with our description for the DC electric field, this model can predict very well many experimental results in [14] and [36], for example, the retraction in the direction parallel to the electric field and the elongation in the perpendicular direction, or the dynamic change of the substrate displacement.
- In order to explain the experimental results using this model, it is necessary to include the idea proposed by Harris *et al.* [36] that under the electric field exposure, the strength of the adhesion is weakened at those parts of the cell facing the electrodes. However, considering only the weakening of the adhesion is not sufficient. Instead, a stimulation of the contraction in the direction parallel to the field or a stimulation of the protrusion in the perpendicular direction also needs to be addressed.
- Our mathematical description was able to predict several effects of DC electric field on both fibroblasts and osteoblasts that are found in the existing experiments. To overcome the remaining weak points, our further investigation will focus on a more efficient model for the adhesion between the cell and the substrate. The bio-mechanical model for focal adhesion by Deshpande *et al.* [17] is a possibility for use as a foundation. Moreover, in order to better predict the elongation of the cell in the direction perpendicular to the electric field, we will investigate the contribution of cell spreading in the model.

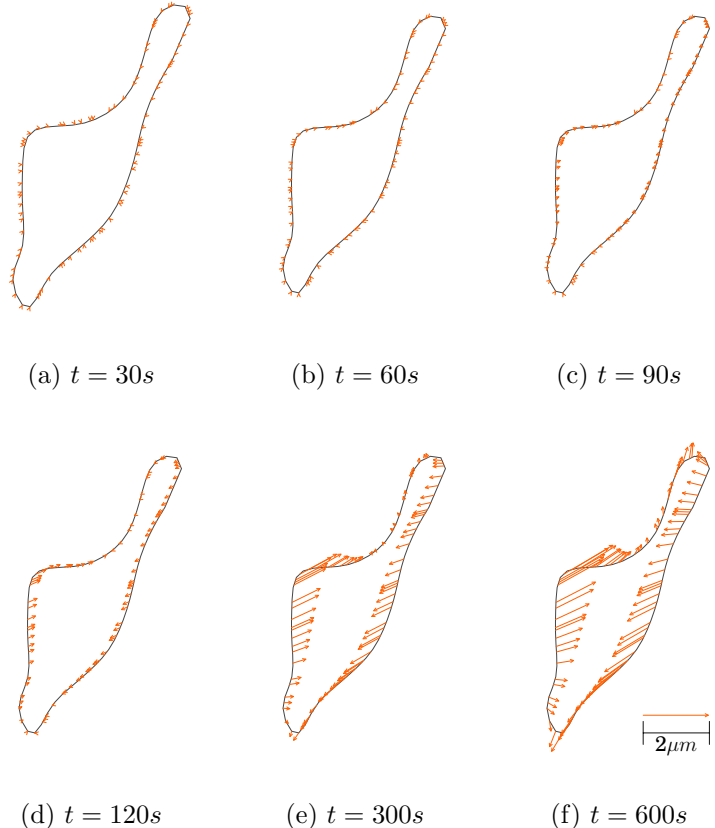


Figure 7.9: Dynamic change of the difference in substrate displacements near the cell peripheries obtained by our simulations. The arrows present the increase in substrate deformation under the effect of electric field and were computed by the subtraction of the substrate displacements for two cases: with and without the presence of the electric field. As in the experiment of Curtze *et al.* [14], the substrate stiffness is 6000Pa.

8. Summary and perspectives

The aim of this thesis is to study the underlying mechanisms of the interactions between osteoblasts and their surrounding bio-materials using computational approaches. Successful theoretical description for those interactions can bring us an improved understanding of cell behaviour and give us a better control over actin formation and cell adhesion. Such knowledge about cells helps further improving the quality of implants and approaching the final aim of tissue engineering, which is to build an implant having structural organisation and functionality similar to a healthy tissue. Particularly, in this thesis, we focused on two main targets of our numerical model: (i) it should predict the formation of actin in osteoblasts when they are cultured on titanium arrays, which were carried out in the experiments at the Department of Cell Biology, University Medical Center Rostock, (ii) it should address the effects of electric field on the contractility of cells and explain the outcomes in existing experiments on different cell types.

We developed our model based on the bio-chemo-mechanical model of Deshpande *et al.* [15], which has been widely applied in modelling cell contractility and shown to have more advantages compared to most other mathematical descriptions in the literature. The model is based on partial differential equations and is an active model, in which the cell reacts actively to external stimulation instead of being a passive material. The active response of the cell is addressed in the model by including the bio-chemical processes, where a variable is introduced to represent the activation of the stress fibres in the cell. The levels of activation are associated with the direction of the fibre and allowed to be different at various locations in the cell. They are dependent on the strength of signal and the current stress state of the cell. To use the bio-chemo-mechanical model in the continuum mechanics framework, an active stress tensor, which results from the activation of stress fibres, is added to the total stress and the equilibrium condition is solved at each time step. The steady state of the cell is reached when the signal strength approaches zero and there is almost no change in cell deformation and activation over time. At that state, a measure defined as the subtraction between the maximum and the average activation level in all directions can give a good prediction in the distribution

8. Summary and perspectives

of the stress fibres in the cell.

The bio-chemo-mechanical model has many applications in modelling mechanical interactions between cells and substrate. It has been used to numerically study the actin distribution in the cells as well as the forces generated by cells of different types, when they are laid on arrays of micro-posts. The simulations can capture very well the deflection of the posts and the highest distribution of stress fibres within the cell that are found in experimental studies. The model has been combined with a bio-mechanical model for cell focal adhesion, which was proposed by Deshpande *et al.* [17], to study the formation of stress fibres in the cell and the development of focal adhesions at the contact regions between the cell and the substrate. The 3D model was applied for different geometries of cells to study cell behaviour in the force indentation experiment.

In part due to its positive features and numerous advantages, the bio-chemo-mechanical model does have a drawback that its order of complexity is very high. At every point in the cell, the activation level needs to be computed for a large number of directions of stress fibres. Together with the deformation of the cell, a great number of degrees of freedom has to be solved for at each time step, even for some 2D simulations. Therefore, significant computer resources are required and a great amount of computation time is demanded. In our attempt to reduce the complexity order of the model, we introduced a semi-analytical approach where a quadratic form is used to approximate the distribution of activation level at every point in the cell. Doing this, instead of sampling a large number of directions for stress fibres, we need to solve for the activation level in three directions for the 2D case and six directions in the 3D case. In addition to describing the formulation, we have provided the derivation of the weak forms that are suitable for using finite element methods. These weak forms can be easily transformed to code in our efficient software implementation that can be applied for a wide range of simulations. We have confirmed the appropriateness of our quadratic representation by comparing the results using our approach with those using the classical representation in the literature. Our formulation delivered similar outcomes, while the computation time was significantly reduced. Moreover, we observed numerically the error produced by our method and confirmed that it is small and in an acceptable range.

Although the bio-chemo-mechanical model has been applied by McGarry *et al.* [57] to simulate cells of different types on arrays of micro-posts, the same approach cannot be directly used for simulating the interaction between osteoblastic cells and titanium arrays in the experiments done at the Department of Cell Biology, University Medical Center Rostock. The linear elastic adhesion model cannot capture the effect that the

8. Summary and perspectives

actin distribution tends to be higher on top of the pillars, instead of at the peripheries of the pillars. We have introduced our mathematical description for the inhomogeneous adhesion of the cell, based on the experimental outcomes that spot-adherence appeared on the pillars. We constructed a smooth function representing the different strength of adhesion at different location on the pillars. The results using our approach can predict several effects in the experiments done by Matschegowski *et al.* [55]. Our finding reconfirms a feature of the bio-chemo-mechanical model that it can capture the strong influence of the boundary condition on the formation of actin filaments in the cells.

The contractility and cytoskeleton of cells of different types under external electric field exposure have been observed experimentally in the literature. Harris *et al.* [36] proposed a technique using silicone rubber substrate to study the influence of DC electric field on the contraction and stress fibre reorientation of fibroblasts. They found a cell retraction accompanied by a gradual weakening in cell contractility in the axis parallel to the electric field followed by an elongation and a reorientation in the direction perpendicular to the field. A similar approach was applied by Curtze *et al.* [14] for osteoblast-like cells and analogous behaviour of the cells was found, where the response to the electric field happened in a different time scale. Moreover, based on the obtained images of substrate displacement, they estimated the dynamic changes in the traction forces in the cells. The bio-chemo-mechanical model is efficient in modelling the contractility and the dynamic reorganisation of the cytoskeleton, but the effects of electric field have not been addressed. We proposed a mathematical description for these effects based on the alternative mechanisms suggested by Harris *et al.* [36]. To express the weakening of the adhesion at the cell margins facing the electrodes, we constructed a smooth scaling function that holds a smaller value at those margins compared to the inner part of the cell. We addressed the stimulation of the contraction in the electric field direction by introducing another scaling function for the maximum tension in stress fibres. This function has an initial value of 1 in every direction. Under the electric field exposure, its value gradually increases in the direction of the field and decreases in the perpendicular direction. Enhanced with our scaling functions, the bio-chemo-mechanical model was then able to predict several results in the experiments of Curtze *et al.* [14] and Harris *et al.* [36], despite a few disagreements. Our finding suggested that the weakening of adhesion at cell regions facing the electrode did indeed contribute the contraction of cell in the direction of the field and the elongation in the perpendicular direction. However, regarding only the decrease in the strength of adhesion is not sufficient. Instead, a stimulation of contraction in the direction of the field or the protrusion

8. Summary and perspectives

in the perpendicular direction should be included. Another suggestion from our finding is that a more efficient model for cell-substrate adhesion and addressing cell spreading in the bio-chemo-mechanical model will give an improved prediction of the experimental results.

The future research based on the work done in this thesis can be driven in many directions. First, a more advanced model for the adhesion between cell and substrate can be used in the simulations of contractility of fibroblasts and osteoblasts under electric field exposure. An alternative is to refine the bio-mechanical model for cell focal adhesion by Deshpande *et al.* [17]. An efficient model such as this could not only better predict experimental results by Curtze *et al.* [14] and Harris *et al.* [36], but also provide the possibility to study the development of focal adhesion under the applied electric field. Second, the effect of external electric field on the formation of actin in osteoblasts when they are cultured on different titanium substrates, including micro-pillar structures, can be studied numerically. Additional experiments can be set up for the verification and further improvement of the model. Finally, the study of actin and electric field distribution in a 3D cell under external electrical stimulation can be performed using Maxwell's equations and the 3D version of the bio-chemo-mechanical model. Addressing and analysing the electric field will increase the complexity of the model. However, thank to our quadratic representation, the computation time promises to remain acceptable.

Bibliography

- [1] Alberts, B., Bray, D., Lewis, J., Raff, M., Roberts, K., and Watson, J. (2002). *Molecular Biology of the Cell*. Garland, 4th edition.
- [2] Alnæs, M. S., Blechta, J., Hake, J., Johansson, A., Kehlet, B., Logg, A., Richardson, C., Ring, J., Rognes, M. E., and Wells, G. N. (2015). The FEniCS project version 1.5. *Archive of Numerical Software*, 3(100).
- [3] Bahls, C. R., Truong, D., and van Rienen, U. (2018). Semi-analytical representation of the activation level in stress fibre directions as alternative to the angular representation in the bio-chemo-mechanical model for cell contractility. *Journal of the Mechanical Behavior of Biomedical Materials*, 77:527 – 533.
- [4] Balaban, N., Schwarz, U., Riveline, D., Goichberg, P., Tzur, G., Sabanay, I., Mahalu, D., Safran, S., Bershadsky, A., Addadi, L., and Geiger, B. (2001). Force and focal adhesion assembly: a close relationship studied using elastic micropatterned substrates. *Nature Cell Biology*.
- [5] Balint, R., Cassidy, N. J., and Cartmell, S. H. (2013). Electrical Stimulation: A Novel Tool for Tissue Engineering. *Tissue Engineering Part B-Reviews*, 19(1):48–57.
- [6] Belytschko, T., Liu, W. K., and Moran, B. (2000). *Nonlinear finite elements for continua and structures*. J. Wiley & sons, Chichester, New York, Weinheim.
- [7] Berthiaume, F. and Yarmush, M. (1999). *Tissue Engineering*, chapter 109. CRC Press.
- [8] Boonen, K. J. M., Langelaan, M. L. P., Polak, R. B., Schaft, D. W. J. V. D., Baaijens, F. P. T., and Post, M. J. (2010). Effects of a combined mechanical stimulation protocol: Value for skeletal muscle tissue engineering. *Journal of Biomechanics*, 43(8):1514–1521.

Bibliography

- [9] Brezzi, F., Hager, W., and Raviart, P. (1978/79). Error estimates for the finite element solution of variational inequalities. part ii. mixed methods. *Numerische Mathematik*, 31:1–16.
- [10] Burridge, K. and Chrzanowska-Wodnicka, M. (1996). Focal adhesions, contractility, and signaling. *Annual review of cell and developmental biology*, 12:463–518.
- [11] Burton, K. and Taylor, D. (1997). Traction forces of cytokinesis measured with optically modified elastic substrata. *Nature*.
- [12] Crisfield, M. (1991). *Non-linear finite element analysis of solids and structures. Volume 1. , Essentials*. Wiley, Chichester, New York.
- [13] Crisfield, M. (1997). *Non-linear finite element analysis of solids and structures. volume 2. , Advanced topics*. John Wiley & Sons, Chichester, New-York.
- [14] Curtze, S., Dembo, M., Miron, M., and Jones, D. B. (2004). Dynamic changes in traction forces with dc electric field in osteoblast-like cells. *Journal of Cell Science*, 117(13):2721–2729.
- [15] Deshpande, V. S., McMeeking, R. M., and Evans, A. G. (2006). A bio-chemo-mechanical model for cell contractility. *Proc. Natl Acad. Sci. USA*, 103:14015–14020.
- [16] Deshpande, V. S., McMeeking, R. M., and Evans, A. G. (2007). A model for the contractility of the cytoskeleton including the effects of stress-fibre formation and dissociation. *Proc. R. Soc. A*, 463:787–815.
- [17] Deshpande, V. S., Mrksich, M., McMeeking, R. M., and Evans, A. G. (2008). A bio-mechanical model for coupling cell contractility with focal adhesion formation. *J. Mech. Phys. Solids*.
- [18] DiMilla, P., Barbee, K., and Lauffenburger, D. (1991). Mathematical model for the effects of adhesion and mechanics on cell migration speed. *Biophysical Journal*, 60(1):15–37.
- [19] Dong, C., Skalak, R., Sung, K.-L. P., Schmid-Schönbein, G. W., and Chien, S. (1988). Passive deformation analysis of human leukocytes. *Journal of Biomechanical Engineering*, 110(1):27–36.

Bibliography

- [20] Dowling, E., Ronan, W., Ofek, G., Deshpande, V., McMeeking, R., Athanasiou, K., and McGarry, J. (2012). The effect of remodelling and contractility of the actin cytoskeleton on the shear resistance of single cells: A computational and experimental investigation. *Journal of the Royal Society Interface*, 9(77):3469–3479.
- [21] du Roure, O., Saez, A., Buguin, A., Austin, R. H., Chavrier, P., Siberzan, P., and Ladoux, B. (2005). Force mapping in epithelial cell migration. *Proceedings of the National Academy of Sciences of the United States of America*, 102(7):2390–2395.
- [22] Erickson, C. A. and Nuccitelli, R. (1984). Embryonic fibroblast motility and orientation can be influenced by physiological electric fields. *Journal of Cell Biology*, 98(1):296–307.
- [23] Feller, L., Jadwat, Y., Khammissa, R. A. G., Meyerov, R., Schechter, I., and Lemmer, J. (2015). Cellular responses evoked by different surface characteristics of intraosseous titanium implants. *BioMed Research International*, 2015:8.
- [24] Foucard, L. and Vernerey, F. J. (2012). A thermodynamical model for stress-fiber organization in contractile cells. *Applied Physics Letters*, 100(1):013702.
- [25] Franke, R.-P., Gräfe, M., Seiffge, D., Mittermayer, C., and Drenckhahn, D. (1984). Induction of human vascular endothelial stress fibres by fluid shear stress.
- [26] Frantz, C., Stewart, K., and Weaver, V. (2010). The extracellular matrix at a glance. *Journal of Cell Science*, 123(24):4195–4200. cited By 442.
- [27] Gasser, T. C., Ogden, R. W., and Holzapfel, G. A. (2006). Hyperelastic modelling of arterial layers with distributed collagen fibre orientations. *Journal of The Royal Society Interface*, 3(6):15–35.
- [28] Geuzaine, C. and Remacle, J.-F. (2009). Gmsh: A 3-d finite element mesh generator with built-in pre- and post-processing facilities. *International Journal for Numerical Methods in Engineering*, 79(11):1309–1331.
- [29] Greiner, A., Biela, S., Chen, H., Spatz, J., and Kemkemer, R. (2015). Featured article: Temporal responses of human endothelial and smooth muscle cells exposed to uniaxial cyclic tensile strain. *Experimental Biology and Medicine*, 240(10):1298–1309.
- [30] Griffiths, D. (1999). *Introduction to Electrodynamics*. Prentice Hall.

Bibliography

- [31] Grodzinsky, A. (2011). *Electrical Interaction Forces: From Intramolecular to Macroscopic*, chapter 4, pages 193–242. Garland Science.
- [32] Guilak, F., Erickson, G. R., and Ting-Beall, H. P. (2002). The Effects of Osmotic Stress on the Viscoelastic and Physical Properties of Articular Chondrocytes. *Bio-physical Journal*, 82(2):720–727.
- [33] Guo, A., Song, B., Reid, B., Gu, Y., Forrester, J. V., Jahoda, C. A., and Zhao, M. (2010). Effects of physiological electric fields on migration of human dermal fibroblasts. *The Journal of investigative dermatology*, 130(9):2320–2327.
- [34] Harris, A., Stopak, D., and Wild, P. (1981). Fibroblast traction as a mechanism for collagen morphogenesis. *Nature*.
- [35] Harris, A., Wild, P., and Stopak, D. (1980). Silicone rubber substrata: a new wrinkle in the study of cell locomotion. *Science*, 208(4440):177–179.
- [36] Harris, A. K., Prysor, N. K., and Paydarfar, D. (1990). Effects of electric fields on fibroblast contractility and cytoskeleton. *Journal of Experimental Zoology*, 253(2):163–176.
- [37] Hill, A. (1938). The heat of shortening and the dynamic constants of muscle. *Proc. R. Soc. B*.
- [38] Hochmuth, R., Ting-Beall, H., Beaty, B., Needham, D., and Tran-Son-Tay, R. (1993). Viscosity of passive human neutrophils undergoing small deformations. *Bio-physical Journal*, 64(5):1596–1601.
- [39] Hochmuth, R. M. (1993). Measuring the mechanical properties of individual human blood cells. *Journal of Biomechanical Engineering*, 115(4B):515–519.
- [40] Hochmuth, R. M. (2000). Micropipette aspiration of living cells. *Journal of Biomechanics*, 33(1):15 – 22.
- [41] Jones, D. B., Nolte, H., Scholübers, J. G., Turner, E., and Veltel, D. (1991). Biochemical signal transduction of mechanical strain in osteoblast-like cells. *Biomaterials*, 12(2):101–110.
- [42] Kan, H.-C., Udaykumar, H. S., Shyy, W., and Tran-Son-Tay, R. (1998). Hydrodynamics of a compound drop with application to leukocyte modeling. *Physics of Fluids*, 10(4):760–774.

Bibliography

- [43] Kanchanawong, P., Shtengel, G., Pasapera, A. M., Ramko, E. B., Davidson, M. W., Hess, H. F., and Waterman, C. M. (2010). Nanoscale architecture of integrin-based cell adhesions. *Nature*, 468(7323):580–584.
- [44] Kaunas, R. and Hsu, H.-J. (2009). A kinematic model of stretch-induced stress fiber turnover and reorientation. *Journal of Theoretical Biology*, 257(2):320–330.
- [45] Kinbara, K., Goldfinger, L. E., Hansen, M., Chou, F.-L., and Ginsberg, M. H. (2003). Ras GTPases: integrins' friends or foes? *Nat Rev Mol Cell Biol*, 4(10):767–778.
- [46] Koay, E. J., Shieh, A. C., and Athanasiou, K. A. (2003). Creep indentation of single cells. *Journal of Biomechanical Engineering*, 125(3):334–341.
- [47] Kronenberg, N. M., Liehm, P., Steude, A., Knipper, J. A., Borger, J. G., Scarelli, G., Franze, K., Powis, S. J., and Gather, M. C. (2017). Long-term imaging of cellular forces with high precision by elastic resonator interference stress microscopy. *Nat Cell Biol*, 19(7):864–872.
- [48] L.E., M. (1969). *Introduction to the Mechanics of a Continuous Medium*. Prentice-Hall, New Jersey.
- [49] Ley, K., Rivera-Nieves, J., Sandborn, W. J., and Shattil, S. (2016). Integrin-based therapeutics: biological basis, clinical use and new drugs. 15:173.
- [50] Li, B. and Wang, J. H.-C. (2010). Application of sensing techniques to cellular force measurement. *Sensors (Basel, Switzerland)*, 10(11):9948–9962.
- [51] Li, X. and Kolega, J. (2002). Effects of direct current electric fields on cell migration and actin filament distribution in bovine vascular endothelial cells. *J Vasc Res*, 39(5):391–404.
- [52] Lim, C., Zhou, E., and Quek, S. (2006). Mechanical models for living cells—a review. *Journal of Biomechanics*, 39(2):195–216.
- [53] Logg, A., Mardal, K.-A., Wells, G. N., et al. (2012). *Automated Solution of Differential Equations by the Finite Element Method*. Springer.
- [54] Maniotis, A. J., Chen, C. S., and Ingber, D. E. (1997). Demonstration of mechanical connections between integrins, cytoskeletal filaments, and nucleoplasm that stabilize

Bibliography

nuclear structure. *Proceedings of the National Academy of Sciences of the United States of America*, 94(3):849–854.

[55] Matschegowski, C., Staehlke, S., Loeffler, R., Lange, R., Chai, F., Kern, D. P., Beck, U., and Nebe, B. J. (2010). Cell architecture-cell function dependencies on titanium arrays with regular geometry. *Biomaterials*, 31:5729–5740.

[56] McCaig, C. D., Rajnicek, A. M., Song, B., and Zhao, M. (2005). Controlling cell behavior electrically: Current views and future potential. *Physiological Reviews*, 85(3):943–978.

[57] McGarry, J. P., Fu, J., Yang, M. T., Chen, C. S., McMeeking, R. M., Evans, A. G., and Deshpande, V. S. (2009). Simulation of the contractile response of cells on an array of micro-posts. *Proc. R. Soc. A*, 367:3477–3497.

[58] Meny, I., Burais, N., Buret, F., and Nicolas, L. (2007). Finite-element modeling of cell exposed to harmonic and transient electric fields. *IEEE Transactions on Magnetics*, 43(4):1773–1776.

[59] Mijailovich, S. M., Kojic, M., Zivkovic, M., Fabry, B., and Fredberg, J. J. (2002). A finite element model of cell deformation during magnetic bead twisting. *Journal of Applied Physiology*, 93(4):1429–1436.

[60] Milner, J. S., Grol, M. W., Beauchage, K. L., Dixon, S. J., and Holdsworth, D. W. (2012). Finite-element modeling of viscoelastic cells during high-frequency cyclic strain. *Journal of Functional Biomaterials*, 3(1):209–224.

[61] Mitchison, J. M. and Swann, M. M. (1954). The mechanical properties of the cell surface. *Journal of Experimental Biology*, 31(3):461–472.

[62] Mizutani, K. and Takai, Y. (2016). Nectin spot: a novel type of nectin-mediated cell adhesion apparatus. *Biochemical Journal*, 473(18):2691–2715.

[63] Moerke, C., Mueller, P., and Nebe, B. (2016). Attempted caveolae-mediated phagocytosis of surface-fixed micro-pillars by human osteoblasts. *Biomaterials*, 76:102–114.

[64] Mogilner, A. and Odde, D. (2011). Modeling cellular processes in 3D. *Trends in Cell Biology*, 21(12):692–700.

Bibliography

- [65] Mohrdieck, C., Wanner, A., Roos, W., Roth, A., Sackmann, E., Spatz, J., and Arzt, E. (2005). A theoretical description of elastic pillar substrates in biophysical experiments. *Chem. Phys. Chem.*
- [66] Munevar, S., Wang, Y., and Dembo, M. (2001). Traction force microscopy of migrating normal and h-ras transformed 3t3 fibroblasts. *Biophysical Journal*, 80(4):1744–1757.
- [67] Nelson, C., Jean, R., Tan, J., Liu, W., Sniadecki, N., Spector, A., and Chen, C. (2005). Emergent patterns of growth controlled by multicellular form and mechanics. *Proc. Natl Acad. Sci. USA*, 102(33).
- [68] Nuccitelli, R. (1988). Physiological electric fields can influence cell motility, growth, and polarity. In Miller, K. R., editor, *A Research Annual*, volume 2 of *Advances in Molecular and Cell Biology*, pages 213 – 233. Elsevier.
- [69] Onuma, E. K. and Hui, S. W. (1988). Electric field-directed cell shape changes, displacement, and cytoskeletal reorganization are calcium dependent. *Journal of Cell Biology*, 106(6):2067–2075.
- [70] Parker, K. K., Tan, J., Chen, C. S., and Tung, L. (2008). Myofibrillar architecture in engineered cardiac myocytes. *Circulation Research*, 103(4):340–342.
- [71] Pathak, A., Deshpande, V., McMeeking, R., and Evans, A. (2008). The simulation of stress fibre and focal adhesion development in cells on patterned substrates. *Journal of the Royal Society Interface*, 5(22):507–524.
- [72] Pelling, A. E. and Horton, M. A. (2008). An historical perspective on cell mechanics. *Pflügers Archiv - European Journal of Physiology*, 456(1):3–12.
- [73] Rodriguez, M. L., McGarry, P. J., and Sniadecki, N. J. (2013). Review on cell mechanics: Experimental and modeling approaches. *Applied Mechanics Reviews*, 65(6).
- [74] Ronan, W., Deshpande, V., McMeeking, R., and McGarry, J. (2012). Numerical investigation of the active role of the actin cytoskeleton in the compression resistance of cells. *Journal of the Mechanical Behavior of Biomedical Materials*, 14:143–157.
- [75] Ronan, W., Deshpande, V., McMeeking, R., and McGarry, J. (2014). Cellular contractility and substrate elasticity: a numerical investigation of the actin cytoskeleton and cell adhesion. *Biomech Model Mechanobiol.*

Bibliography

[76] Ronan, W., McMeeking, R., Chen, C., McGarry, J., and Deshpande, V. (2015). Co-operative contractility: The role of stress fibres in the regulation of cell-cell junctions. *Journal of Biomechanics*, 48(3):520–528.

[77] Ronan, W., Pathak, A., Deshpande, V., McMeeking, R., and McGarry, J. (2013). Simulation of the mechanical response of cells on micropost substrates. *Journal of Biomechanical Engineering*, 135(10).

[78] Santos, L., Reis, R., and Gomes, M. (2015). Harnessing magnetic-mechano actuation in regenerative medicine and tissue engineering. *Trends in Biotechnology*, 33(8):471–479.

[79] Sato, M., Ohshima, N., and Nerem, R. (1996). Viscoelastic properties of cultured porcine aortic endothelial cells exposed to shear stress. *Journal of Biomechanics*, 29(4):461 – 467.

[80] Schmid-Schönbein, G. W., Sung, K. L., Tözeren, H., Skalak, R., and Chien, S. (1981). Passive mechanical properties of human leukocytes. *Biophysical Journal*, 36(1):243–256.

[81] Schoen, I., Hu, W., and Klotzsch, E. (2010). Probing cellular traction forces by micropillar arrays: Contribution of substrate warping to pillar deflection. *Nano Lett.*

[82] Shepherd, D. E. T. and Azangwe, G. (2007). Synthetic versus tissue-engineered implants for joint replacement. *Applied Bionics and Biomechanics*, 4(4).

[83] Shin, D. and Athanasiou, K. (1999). Cytoindentation for obtaining cell biomechanical properties. *Journal of Orthopaedic Research*, 17(6):880–890.

[84] Sniadecki, N., Anguelouch, A., Yang, M., Lamb, C., Liu, Z., Kirschner, S., Liu, Y., Reich, D., and Chen, C. (2007). Magnetic microposts as an approach to apply forces to living cells. *Proc. Natl Acad. Sci. USA*.

[85] Soiné, J. R. D., Brand, C. A., Stricker, J., Oakes, P. W., Gardel, M. L., and Schwarz, U. S. (2015). Model-based traction force microscopy reveals differential tension in cellular actin bundles. *PLOS Computational Biology*, 11(3):1–16.

[86] Süli, E. (2013). *A brief excursion into the mathematical theory of mixed finite element methods*. Lecture Notes, University of Oxford.

Bibliography

- [87] Süli, E. and Mayers, D. F. (2003). *An introduction to numerical analysis*. Cambridge: Cambridge University Press.
- [88] Taghian, T., Narmoneva, D. A., and Kogan, A. B. (2015). Modulation of cell function by electric field: a high-resolution analysis. *Journal of the Royal Society, Interface / the Royal Society*, 12(107):21–25.
- [89] Tan, J. L., Tien, J., Pirone, D. M., Gray, D. S., Bhadriraju, K., and Chen, C. S. (2003). Cells lying on a bed of microneedles: An approach to isolate mechanical force. *Proc. Natl Acad. Sci. USA*, 100:1484–1489.
- [90] Theret, D. P., Levesque, M. J., Sato, M., Nerem, R. M., and Wheeler, L. T. (1988). The application of a homogeneous half-space model in the analysis of endothelial cell micropipette measurements. *Journal of Biomechanical Engineering*, 110(3):190–199.
- [91] Tolić-Nørrelykke, I. M. and Wang, N. (2005). Traction in smooth muscle cells varies with cell spreading. *Journal of Biomechanics*, 38(7):1405–1412.
- [92] Tran-Son-Tay, R., Needham, D., Yeung, A., and Hochmuth, R. (1991). Time-dependent recovery of passive neutrophils after large deformation. *Biophysical Journal*, 60(4):856–866.
- [93] Trickey, W. R., Baaijens, F. P., Laursen, T. A., Alexopoulos, L. G., and Guilak, F. (2006). Determination of the poisson’s ratio of the cell: recovery properties of chondrocytes after release from complete micropipette aspiration. *Journal of Biomechanics*, 39(1):78 – 87.
- [94] Trickey, W. R., Lee, G. M., and Guilak, F. (2000). Viscoelastic properties of chondrocytes from normal and osteoarthritic human cartilage. *Journal of Orthopaedic Research*, 18(6):891–898.
- [95] Truong, D., Bahls, C., Nebe, B., and van Rienen, U. (2016a). The cell contractility model and the cell adhesion model: Reducing the complexity and preparing the coupling to electrical forces. *11th International Conference on Scientific Computing in Electrical Engineering, St. Wolfgang, Austria*.
- [96] Truong, D., Bahls, C., Nebe, B., and van Rienen, U. (2016b). An implementation for the simulation of cells on micro-post arrays. *38th Annual International Conference of the IEEE Engineering in Medicine and Biology Society, Florida, USA*.

Bibliography

[97] Truong, D., Bahls, C., Nebe, B., and van Rienen, U. (2017a). Simulation of actin distribution of osteoblasts on titanium pillar arrays using a bio-chemo-mechanical model. *Submitted to Int. J. Numer. Meth. Biomed Engng.*

[98] Truong, D., Bahls, C., Nebe, B., and van Rienen, U. (2018). Modelling effects of dc electric field on contractility and cytoskeleton of fibroblasts and osteoblast-like cells using a bio-chemo-mechanical model. *In preparation.*

[99] Truong, D., Bahls, C., and van Rienen, U. (2017b). An efficient 2d implementation of a bio-chemo-mechanical model employing a quadratic representation to study cells on micro-post arrays. *Submitted to Finite Elements in Analysis and Design.*

[100] Truong, D., Mörke, C., Nebe, B., and van Rienen, U. (2015a). Numerical study on actin filament patterns on various micro-structured pillar arrays. *5th International Symposium Interface Biology of Implants (IBI), Rostock-Warnemünde, Germany.*

[101] Truong, D., Nebe, B., and van Rienen, U. (2015b). Application of bio-chemo-mechanical models on actin filament patterns of mg63 osteoblasts on micro-structured titanium arrays. *Joint ISCA-Inspire workshop on Electrically Active Materials of Medical Devices (EAMMD), Limerick, Ireland.*

[102] Truong, D., Nebe, B., and van Rienen, U. (2015c). The bio-chemo-mechanical model for cell contractility: an implementation and application. *27th Workshop on “Advances in Electromagnetic Research” (KWT), Riezlern, Austria.*

[103] Truong, D., Nebe, B., and van Rienen, U. (2015d). An implementation for the bio-chemo-mechanical model of cell contractility. *37th Annual International Conference of the IEEE Engineering in Medicine and Biology Society (EMBC), Milano, Italy.*

[104] van Rienen, U. (2001). *Numerical Methods in Computational Electrodynamics.* Springer, Berlin Heidelberg.

[105] Van Vliet, K., Bao, G., and Suresh, S. (2003). The biomechanics toolbox: experimental approaches for living cells and biomolecules. *Acta Materialia*, 51(19):5881–5905.

[106] Vaziri, A. and Gopinath, A. (2008). Cell and biomolecular mechanics in silico. *Nat Mater*, 7(1):15–23.

Bibliography

- [107] Vernerey, F. J. and Farsad, M. (2011). A constrained mixture approach to mechano-sensing and force generation in contractile cells. *Journal of the Mechanical Behavior of Biomedical Materials*, 4(8):1683–1699.
- [108] Wang, H., Ip, W., Boissy, R., and Grood, E. S. (1995). Cell orientation response to cyclically deformed substrates: Experimental validation of a cell model. *Journal of Biomechanics*, 28(12):1543–1552.
- [109] Wang, N., Tolic-Norrelykke, I. M., Chen, J., Mijailovich, S. M., Butler, J. P., Fredberg, J. J., and Stamenovic, D. (2002). Cell prestress. i. stiffness and pre-stress are closely associated in adherent contractile cells. *Am J Physiol Cell Physiol*, 282(3):C606–16.
- [110] Wriggers, P. (2008). *Nonlinear Finite Element Methods*. Springer Berlin Heidelberg.
- [111] Xiao, T., Takagi, J., Coller, B., Wang, J.-H., and Springer, T. (2004). Structural basis for allostery in integrins and binding to fibrinogen-mimetic therapeutics. *Nature*, 432(7013):59–67.
- [112] Zemel, A., Bischofs, I. B., and Safran, S. A. (2006). Active elasticity of gels with contractile cells. *Phys. Rev. Lett.*, 97:128103.
- [113] Zhao, M., Agius-Fernandez, A., Forrester, J. V., and McCaig, C. D. (1996). Directed migration of corneal epithelial sheets in physiological electric fields. *Investigative Ophthalmology & Visual Science*, 37(13):2548.

A. FEniCS implementation for simulation of a cell on micro-post array

The open source software *FEniCS*, version 2016.2 is used in our implementation. One of the advantages of this framework is that the mathematical models are easily translated into efficient finite element code [53]. For visualising the results, the software *Paraview* and the plotting library *matplotlib* are used with Python.

Model parameters All the parameters involved for the bio-chemo-mechanical model and cell material properties as suggested by McGarry *et al.* [57] are shown in Tab. A.1. In addition to that, we used the values $E_{\text{pillar}} = 2.5 \cdot 10^5 \text{nN}/\mu\text{m}^2$, $\nu_{\text{pillar}} = 0.45$ for Young's

Parameter	σ_{max}	θ	\bar{k}_{v}	\bar{k}_{f}	\bar{k}_{b}	$\dot{\varepsilon}_0$	E_{cell}	ν_{cell}
Unit	[nN/ μm^2]	[s]				[s^{-1}]	[nN/ μm^2]	
Value	25	70	7	10	1	0.003	0.4	0.3

Table A.1: Parameters for the BCM model and cell material properties.

modulus and Poisson's ratio of the pillars and observed that they behaved like rigid bodies, when their straining is too small. The pillars have $1.5\mu\text{m}$ radius and $32\text{nN}/\mu\text{m}$ bending stiffness. The spacing between pillar centres is $10\mu\text{m}$. The cell thickness is $b = 1\mu\text{m}$ and the adhesion stiffness is $k_t = 500\text{nN}/\mu\text{m}^3$. The number of directions for stress fibres is chosen to be 36, as in [15], while $\Delta t = 2\text{s}$ was used for the time step. We carried out a careful analysis to ensure that these parameter choices are appropriate for a meaningful solution. The declaration of all parameters is shown in Listing. A.1.

A. FEniCS implementation for simulation of a cell on micro-post array

Code Listing A.1: Define parameters for the model

```
# model parameters
nPost, dPost, rPost = 2, 10.0, 1.5
theta = 70
epsDot0 = 0.003
kvBar, kbBar, kfBar = 7.0, 1.0, 10.0
sigmaMax = 25.0 # nN/um2
thickness = 1.0 #um
ECell, nuCell = 0.4, 0.3 # nN/um2, 1
EPillar, nuPillar = 2.0E5, 0.4 # nN/um2, 1
ksBar = 1.28
ks = ksBar * sigmaMax * thickness
ks = ks / (math.pi * (rPost**2)) # spring stiffness per area
kFA, xi = 0.15, 3333 # nN/um, 1/um2
kt = kFA * xi

Ct = Constant(1) # level of signal
deltaT = Constant(2.0)
nDirs = 36
```

Mesh We used the `gmsh` generator to create most of our meshes. The `dolfin-convert` command is then used to convert the generated meshes to `xml` file that can be read in FEniCS. In order for OpenMPI parallelism to be utilised, we use a file of hierarchical data format (HDF) to store the mesh together with its sub-domain data. An example for creating a `Mesh` object in FEniCS using data from the `hdf5` file is illustrated in Listing A.2. Plots of the mesh and its sub-domain data for a cell on 2×2 pillars are shown in Figure A.1.

Code Listing A.2: Read the mesh data from a `hdf5` file

```
mesh = Mesh()
hdf = HDF5File(mesh.mpi_comm(), 'mesh.h5', 'r')
hdf.read(mesh, '/mesh', False)
subdomains = CellFunction('size_t', mesh)
hdf.read(subdomains, '/subdomains')
```

Function spaces The variables to be solved include the mixed displacement increment $\Delta\mathbf{u} = (\Delta\mathbf{u}_{\text{cell}}, \Delta\mathbf{u}_{\text{pillar}})$ and the activation level $\boldsymbol{\eta} = (\eta_1, \dots, \eta_{N_d})$. The mixed displace-

A. FEniCS implementation for simulation of a cell on micro-post array

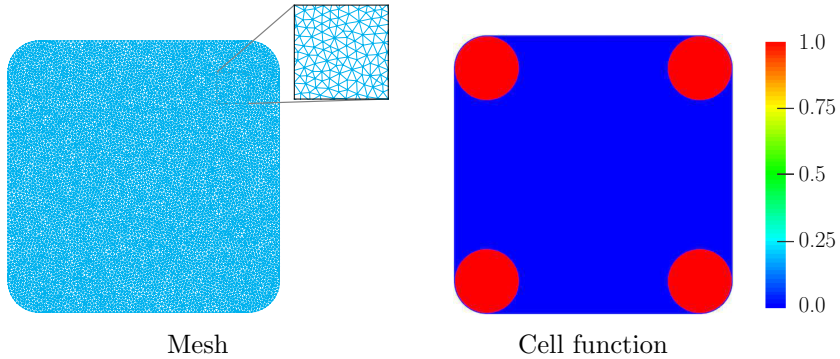


Figure A.1: Mesh and physical regions for cell on 2×2 pillars that are stored in a hdf5 file.

The number of mesh cells is 15 624, while the numbers of degrees of freedom for the deformation and the activation are 31 826 and 562 464, respectively.

ment is then obtained by a time integration $\mathbf{u} = \int_0^t \dot{\mathbf{u}} dt$. First-order Lagrangian elements are used for the displacements of both, cell and pillars. As the activation level in each direction is a real number, zero-order discontinuous Lagrange elements are sufficient. Listing A.3 shows how the function spaces and the primary variables are created.

Code Listing A.3: Define functional spaces

```
CG1 = VectorElement("Lagrange", mesh.ufl_cell(), 1)
V = FunctionSpace(mesh, MixedElement(CG1, CG1))
u, u0, deltaU = Function(V), Function(V), Function(V)

VEta = VectorFunctionSpace(mesh, "DG", 0, nDirs)
etaCoeff, etaCoeff0 = Function(VEta), Function(VEta)
```

Strain and stress tensors The cell and pillar materials are assumed to be isotropic linearly elastic. Geometrically non-linear analysis is considered, so the Green-Lagrange strain tensor \mathbf{E} is used and the Saint Venant–Kirchhoff material model is applied. The stress tensor is related to the strain tensor via the Lamé material constants λ and μ , which can be expressed in terms of the Young’s modulus E and the Poisson’s ratio ν as

$$\lambda = \frac{E\nu}{(1 + \nu)(1 - 2\nu)}, \quad \mu = \frac{E}{2(1 + \nu)}$$

The calculation of these constants for the cell and the pillars in the implementation is shown in Listing A.4.

A. FEniCS implementation for simulation of a cell on micro-post array

Code Listing A.4: Compute the Lamé constants

```
muCell, lmbdaCell = ECell / (2 * (1 + nuCell)), ECell * nuCell / ((1
    + nuCell) * (1 - 2 * nuCell))
muPillar, lmbdaPillar = EPillar / (2 * (1 + nuPillar)), EPillar *
    nuPillar / ((1 + nuPillar) * (1 - 2 * nuPillar))
```

The stress tensor is obtained as $\mathbf{S} = \lambda \text{tr}(\mathbf{E})\mathbf{I} + 2\mu\mathbf{E}$. Listing A.5 shows the computation of the displacement \mathbf{u} at each time step from the displacement increment $\Delta\mathbf{u}$, the strain and stress tensors for cell and pillars.

Code Listing A.5: Define strain and stress tensors

```
(deltaUc, deltaUp) = split(deltaU)
(u0, u0) = split(u0)

uUpdate = u + deltaU
ucUpdate, upUpdate = u0 + deltaUc, u0 + deltaUp

du1, dv1 = TrialFunction(V), TestFunction(V)
a, L = inner(du1, dv1)*dx, inner(uUpdate, dv1)*dx
problemU = LinearVariationalProblem(a, L, u)
solverU = LinearVariationalSolver(problemU)

dim = u.ufl_domain().geometric_dimension()

Id = Identity(dim)
Fc, Fp = Id + grad(ucUpdate), Id + grad(upUpdate)
Ec, Ep = 0.5 * (Fc.T*Fc - Id), 0.5 * (Fp.T*Fp - Id) # strain tensors

SPassiveCell = 2 * muCell * Ec + lmbdaCell * tr(Ec) * Id
SPassivePillar = 2 * muPillar * Ep + lmbdaPillar * tr(Ep) * Id
```

Finally, the strain rate in the cell domain can be obtained from the cell displacement rate as $\dot{\mathbf{E}}_{\text{cell}} = \frac{1}{2}(\dot{\mathbf{F}}_{\text{cell}}^\top \cdot \dot{\mathbf{F}}_{\text{cell}} - \mathbf{1})$, with $\dot{\mathbf{F}}_{\text{cell}} = \mathbf{1} + \nabla \dot{\mathbf{u}}_{\text{cell}}$:

Code Listing A.6: Define the strain rate tensor

```
Fcdot = Id + grad(deltaUc/deltaT)
strainRate = 0.5 * (Fcdot.T*Fcdot - Id) # strain rate for cell
```

Computation of the active stress tensor Listing A.7 shows the computation of the components of the active stress from Eq. (4.24). The active stress tensor is then constructed from these components. In addition, the increment for the activation level at each time step, $\Delta\eta = \dot{\eta} \cdot \Delta t$ is also obtained:

Code Listing A.7: Construct the active stress and increment for the activation

```

strainRatePhi = []
deltaEta = []

activeStress11, activeStress12, activeStress22 = 0, 0, 0

phi = -math.pi / 2.0 # angle
deltaPhi = math.pi / (nDirs - 1.0)

for i in xrange(nDirs):
    cosSquare = math.cos(phi) ** 2
    sinSquare = math.sin(phi) ** 2
    sin2phi = math.sin(2.0 * phi)

    strainRatePhi.append(strainRate[0, 0] * cosSquare +
        strainRate[0, 1] * sin2phi + strainRate[1, 1] * sinSquare)
    activeStressPhi = sigmaMax * (etaCoeff.sub(i) + (kvBar /
        epsDot0) * strainRatePhi[i])
    deltaEta.append(Ct * (1.0 - etaCoeff.sub(i)) * kfBar / theta -
        ((kvBar / epsDot0) * strainRatePhi[i]) * kbBar / theta)

    if (i == 0 or i == nDirs - 1):
        activeStress11 += 0.5 * activeStressPhi * cosSquare
        activeStress12 += 0.5 * activeStressPhi * sin2phi
        activeStress22 += 0.5 * activeStressPhi * sinSquare
    else:
        activeStress11 += activeStressPhi * cosSquare
        activeStress12 += activeStressPhi * sin2phi
        activeStress22 += activeStressPhi * sinSquare

    phi += deltaPhi

activeStress11 = (1.0 / (nDirs - 1.0)) * activeStress11
activeStress12 = (1.0 / (nDirs - 1.0)) * activeStress12 * 0.5
activeStress22 = (1.0 / (nDirs - 1.0)) * activeStress22
activeStress = as_matrix([[activeStress11, activeStress12], [
    activeStress12, activeStress22]])

```

A. FEniCS implementation for simulation of a cell on micro-post array

```

dEta, dvEta = TrialFunction(VEta), TestFunction(VEta)
problemEta = LinearVariationalProblem(inner(dEta, dvEta)*dx,
    inner(etaCoeff0 + deltaT * as_vector(deltaEta), dvEta)*dx,
    etaCoeff)
solverEta = LinearVariationalSolver(problemEta)

```

Defining a non-linear form for the coupled problem The non-linear form is obtained directly from Eq. (4.32).

Code Listing A.8: Arrange the weak form and define non-linear problem

```

# integrals for sub-domains: 1 for cell parts in contact with
# pillars, 0 for the rest
dx = Measure("dx", domain=mesh, subdomain_data=subdomains)
du, w = TrialFunction(V), TestFunction(V)

# nonlinear variational problem
F = inner(SPassiveCell + activeStress, grad(vc)) * (dx(0) + dx(1)) # cell
F += inner(SPassivePillar, grad(vp)) * dx(1) # post elasticity
F += ks * dot(upUpdate, vp) * dx(1) # springs on posts
F += dot(upUpdate, vp) * dx(0) # fix region without posts
F += kt * inner(ucUpdate - upUpdate, vc) * dx(1) # contact force on cell
F += kt * inner(upUpdate - ucUpdate, vp) * dx(1) # contact force on posts

J = derivative(F, deltaU, du)

problem = NonlinearVariationalProblem(F, deltaU, [], J)
solver = NonlinearVariationalSolver(problem)
solver.parameters['newton_solver']['relative_tolerance'] = 1E-6

```

Performing time-stepping The procedure for solving the time-dependent problem is shown in Listing A.9. The solver is advanced in time from t^n to t^{n+1} until the steady state is reached, i.e., when $\Delta\mathbf{u}$ and $\Delta\mathbf{a}$ are close to zero. For convenience, we export the mixed displacement and the activation level to **hdf5** files and use another Python script

A. FEniCS implementation for simulation of a cell on micro-post array

for post-processing of the results.

Code Listing A.9: Perform time stepping

```

fuFile = HDF5File(mesh.mpi_comm(), 'result/disp.h5', "w")
fetaFile = HDF5File(mesh.mpi_comm(), 'result/etaCoeff.h5', "w")
fuFile.write(u, "/initial")
faFile.write(aCoeff, "/initial")

# Time integration
t, timeEnd = 0, 2000
step = 0

while t < timeEnd:
    t += float(deltaT)
    print "Step: " + str(step) + ", time = " + str(t)

    # update concentration C(t)
    Ct.assign(math.exp(-t / theta))

    # solve for deformation
    solver.solve()
    solverU.solve()
    u0.vector()[:] = u.vector() # update deformation

    # solve for activation and update the values
    solverEta.solve()
    etaCoeff0.vector()[:] = etaCoeff.vector()

    step += 1
    fuFile.write(u, "/values_{}".format(step))
    fetaFile.write(etaCoeff, "/values_{}".format(step))

    normDeltaU = norm(deltaU, '12')
    etaDot = project(as_vector(deltaEta), VEta)
    normEta = norm(etaDot, '12')

    if (normDeltaU < 1E-4 and normEta/nDirs < 1E-4):
        print "Steady-state is reached at t = " + str(t)
        break

fuFile.close()
fetaFile.close()

```

B. Stability analysis

We carried out analyses to make sure that the solutions are stable with our choice of the time step size. Figure B.1 shows an exemplary analysis for the simulation of a cell on 2×2 posts. The plot illustrates the average activation at a specific point in the cell, for different time step sizes used. Here, we chose the point $(x_0, y_0) = (2.5\mu\text{m}, 2.5\mu\text{m})$, where the origin is located at the centre of the cell, as we saw the change in actin distribution near this point. A fine mesh is used, with the maximum edge length of $0.248\mu\text{m}$. We

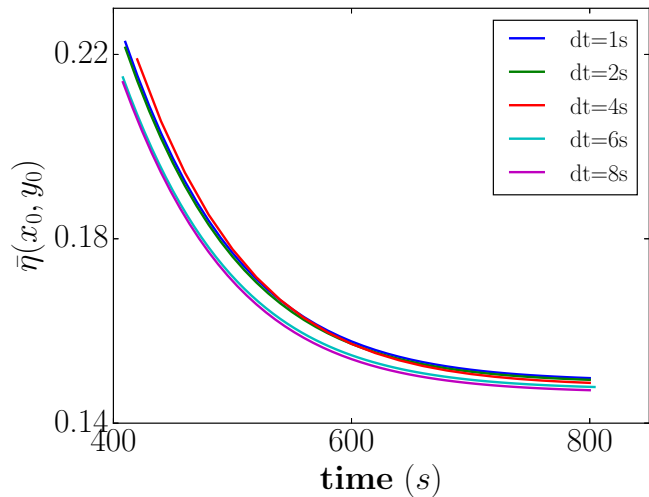


Figure B.1: Plot for the average activation at a point in the cell over time for different time steps used.

can clearly see from the plot that there is almost no change in the results when the time step is less than or equal to 2s . A similar outcome was obtained when we observed the cell deformation.

C. Convergence study

We performed different mesh convergence studies to ensure the accuracy of our solutions. Figure C.1 shows an exemplary convergence study for the simulation of a cell on 2×2 posts. The plot illustrates the magnitudes of cell deformation and the relative errors, for different sizes of the mesh. We used the time step size of 0.1s for all meshes and made an analysis to assure that the solution is stable for the coarsest mesh. We can

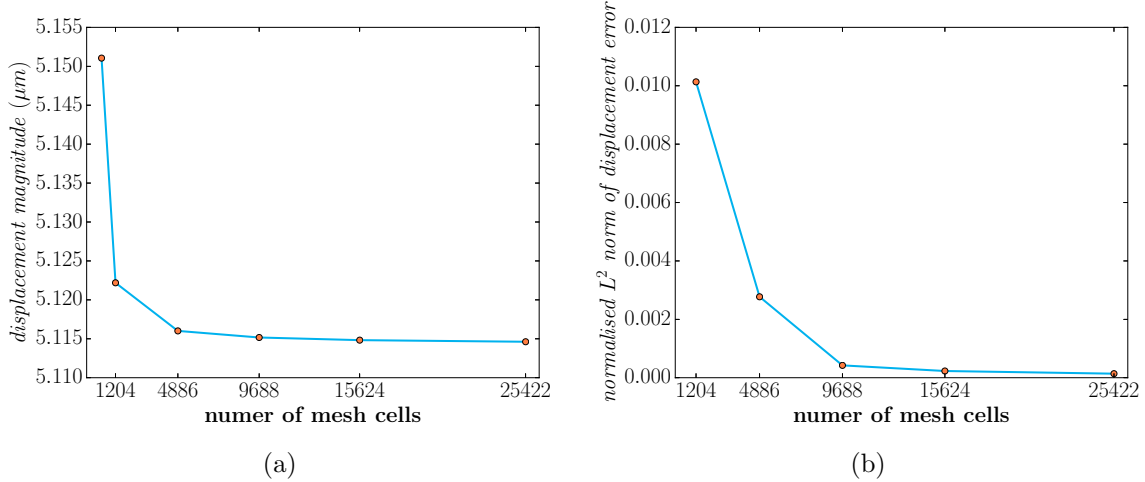


Figure C.1: Plot of the magnitudes of cell displacement and the relative errors $\|u_k - u_{k-1}\|/\|u_k\|$ for meshes of different sizes.

see that as the number of mesh cells increased, the displacement results converged and the error approaches zero. A good accuracy is obtained for the mesh with 15 624 cells, corresponding to the maximum edge length of around $0.25\mu\text{m}$.